APPLIED RADIOCHEMISTRY IN THE NUCLEAR FORENSIC ANALYSIS OF WEAPONS-USABLE PLUTONIUM

A Dissertation

By

KEVIN JAMES GLENNON

Submitted to the Office of Graduate and Professional Studies of
Texas A&M University
In partial fulfillment of the requirements for the degree of

DOCTOR OF PHILOSOPHY

Chair of Committee,	Charles M. Folden III
Committee Members,	Sherry J. Yennello
	Sunil S. Chirayath
	Emile A. Schweikert
Head of Department,	Simon W. North

December 2020

Major Subject: Chemistry

ABSTRACT

Several forensic analyses have been performed on irradiated UO_2 and weapons usable Pu to discriminate their origin and history. The discrimination techniques applied here may be used to aid intelligence officials in the investigation of proliferated special nuclear materials world-wide. Various radiochemical methods have been used to dissolve, separate, and characterize special nuclear materials to measure forensic signatures of interest to the discrimination process. The primary samples investigated were depleted UO_2 containing fuel-grade Pu irradiated at the High Flux Isotope Reactor in Oak Ridge, TN, natural UO_2 containing weapons-grade Pu irradiated at the University of Missouri Research Reactor in Columbia, MO, and four undocumented samples of super-grade Pu identified at Los Alamos National Laboratory in Los Alamos, NM.

Typical radiochemical techniques applied include acid digestions, ion exchange and extraction chromatographies, liquid-liquid extractions, mass spectrometry, and various forms of radiation detection. The principal forensic signatures investigated include isotope ratios of Pu, U, and the fission product elements, inter-elemental nuclide ratios of various chronometer pairs, and trace metal content. These signatures were used to discriminate the reactor origin and irradiation history of all primary materials; the chemical histories of the Pu samples from Los Alamos National Laboratory were also uncovered.

The applied radiochemical and forensic techniques were used to confirm the known origin and production date of the UO_2 materials irradiated at the High Flux Isotope Reactor and the University of Missouri Research Reactor. Their possible origination from other similar nuclear reactors was excluded. The four undocumented Pu samples identified at Los Alamos National Laboratory were suspected to originate from the X-10 reactor during the Manhattan Project of the second World War. The forensic signatures available in these samples indicate they were produced and separated in the early days of weapons science between 1944 – 1954. One of these samples was specifically discovered to be among the first kilogram of Pu ever produced by humankind.

ACKNOWLEDGEMENTS

I would like to thank my laboratory colleagues Merinda F. Volia, Evgeny E. Tereshatov, and Evelyn M. Bond for their guidance and company over many long hours in the radiochemistry laboratory. I would also like to thank Charles M. Folden III, Sunil S. Chirayath, and Brent V. Miller for their guidance in my specialized research, and Jeremy M. Osborn and Patrick J. Oneal for their extensive efforts in reactor modeling and simulations.

CONTRIBUTORS AND FUNDING SOURCES

Contributors

This work was supervised by a dissertation committee consisting of committee chair Associate Professor Charles M. Folden III and committee members Professors Sherry J. Yennello and Emile A. Schweikert of the Department of Chemistry and Associate Professor Sunil S. Chirayath of the Department of Nuclear Engineering.

Maximum likelihood analysis and most reactor simulations in support of these investigations were performed by Dr. Jeremy M. Osborn as published in 2018 and 2019. Modeling and simulation of the X-10 reactor was provided by Patrick J. Oneal. The super-grade Pu and necessary supervisions were provided by Dr. Evelyn M. Bond.

All other work was completed independently by the author.

Funding Sources

First-year graduate studies were supported by a Teaching Assistantship from the Department of Chemistry First Year Chemistry Program. Further graduate studies were supported by the Department of Energy National Nuclear Security Administration under Award Number DE-NA0003180. Some support was received from the Los Alamos National Laboratory Seaborg Fellowship program.

This work was prepared as an account of work sponsored by an agency of the United States Government. Neither the United States Government nor any agency

thereof, nor any of their employees, makes any warranty, express or implied, or assumes any legal liability or responsibility for the accuracy, completeness, or usefulness of any information, apparatus, product, or process disclosed, or represents that its use would not infringe privately owned rights. Reference herein to any specific commercial product, process, or service by trade name, trademark, manufacturer, or otherwise does not necessarily constitute or imply its endorsement, recommendation, or favoring by the United States Government or any agency thereof. The views and opinions of authors expressed herein do not necessarily state or reflect those of the United States Government or any agency thereof.

TABLE OF CONTENTS

Page

Page

Page

LIST OF FIGURES

Page

Page

Page

LIST OF TABLES

Page

CHAPTER I

INTRODUCTION

Nuclear forensics began as a field circa 1993 when a Department of Energy (DoE) official posed the following questions to Lawrence Livermore National Laboratory (LLNL) scientists:

> *"How quickly and with what certainty (if any) could we identify the origin of a nuclear weapon unclaimed by anyone?" (1)*

The LLNL scientists found themselves briefly puzzled about answering these brand-new questions – at the time, radiochemists were trained to identify the capabilities of a nuclear weapon, but not the origins of the device or its components. During these early days, their work established chronometry and reactor discrimination techniques as key components in nuclear forensic efforts (*1*). Around the same time, investigative forces in the Russian Federation and the European Union realized the importance of these same signatures (*2, 3*).

Since then, nuclear forensics has blossomed into a thriving field with internationally recognized importance in nuclear security (*4-8*), primarily using concepts in radiochemistry and nuclear engineering to solve attribution questions such as the ones initially posed circa 1993. Modern applications of nuclear forensics have expanded the scope of these questions to include information about special nuclear material (SNM) outside of nuclear weapons, including separated Pu, irradiated UO_2, and materials related to fuel reprocessing (*8-24*).

The techniques most commonly applied in these modern nuclear forensic "pre-detonation" investigations include chronometry (*25-40*), isotopic and radiopurity evaluations (*41-50*), reactor discrimination (*51-64*), trace metal analysis (*65-72*), and sample morphology and composition studies (*73-85*). The other side of modern nuclear forensics performs "post-detonation" investigations of materials which have been exposed to a nuclear detonation to determine the composition and origin of the detonating device (*86-95*).

The modern nuclear forensic efforts applied herein focus on pre-detonation investigations of SNM containing weapons-usable Pu. The primary samples investigated were depleted UO_2 containing fuel-grade Pu irradiated at the High Flux Isotope Reactor in Oak Ridge, TN, natural UO_2 containing weapons-grade Pu irradiated at the University of Missouri Research Reactor in Columbia, MO, and four samples of undocumented Pu identified at Los Alamos National Laboratory in Los Alamos, NM. Typical radiochemical techniques applied include acid digestions, ion exchange and extraction chromatographies, liquid-liquid extractions, mass spectrometry, and various forms of radiation detection. These radiochemical techniques were used to assay forensic signatures and observables related to the samples' identity (isotopic and radiopurity evaluations), chemical age (chronometry), reactor origin (reactor discrimination), and chemical history (trace metal analysis). The following sections discuss the fundamental basis and modern applications of each technique used in this dissertation in detail.

1.1 Fundamentals of Nuclear and Radiochemistry in Forensics

A radiochemist uses the fundamental properties of radioactive nuclei to identify and quantify radioactive species present in trace or bulk materials. A nucleus is said to be radioactive if there exists a lower energy state it may transition to through one of several modes of radioactive decay. The most prominent modes of radioactive decay across the chart of nuclides (Figure 1.01) include alpha (α), beta minus (β^-), beta plus (β^+), electron capture (EC), spontaneous fission (SF), and gamma (γ) decay (*96*). These decay modes represent the release of energy from a radioactive nucleus via particle or photon emission during its transition to a lower energy state; in $\beta^{-/+}$ and EC decay, protons (p) and neutrons (n) are transmuted amongst each other while leptons are produced.

Radioactive decay is a "truly spontaneous" process; not only is it always thermodynamically spontaneous with a release of free energy ($\Delta G < 0$), it will occur without external stimuli. This distinguishes radioactive decay from nuclear reactions which are induced by external stimuli. Generally, radioactive nuclei decay with a fixed decay constant regardless of their chemical environment. The transition from one nucleus to another may be demonstrated for α, β^-, β^+, EC, SF, and γ decay by Equations 1.01, 1.02, 1.03, 1.04, 1.05, and 1.06 respectively, where W, X, and Y represent specific nuclides with atomic number Z and mass number A, β represents an electron (e^-), ν its neutrino, and overbars indicate anti-particles. An α particle is composed of two neutrons and two protons, while γ represents a photon and a superscript * indicates an excited nuclear state.

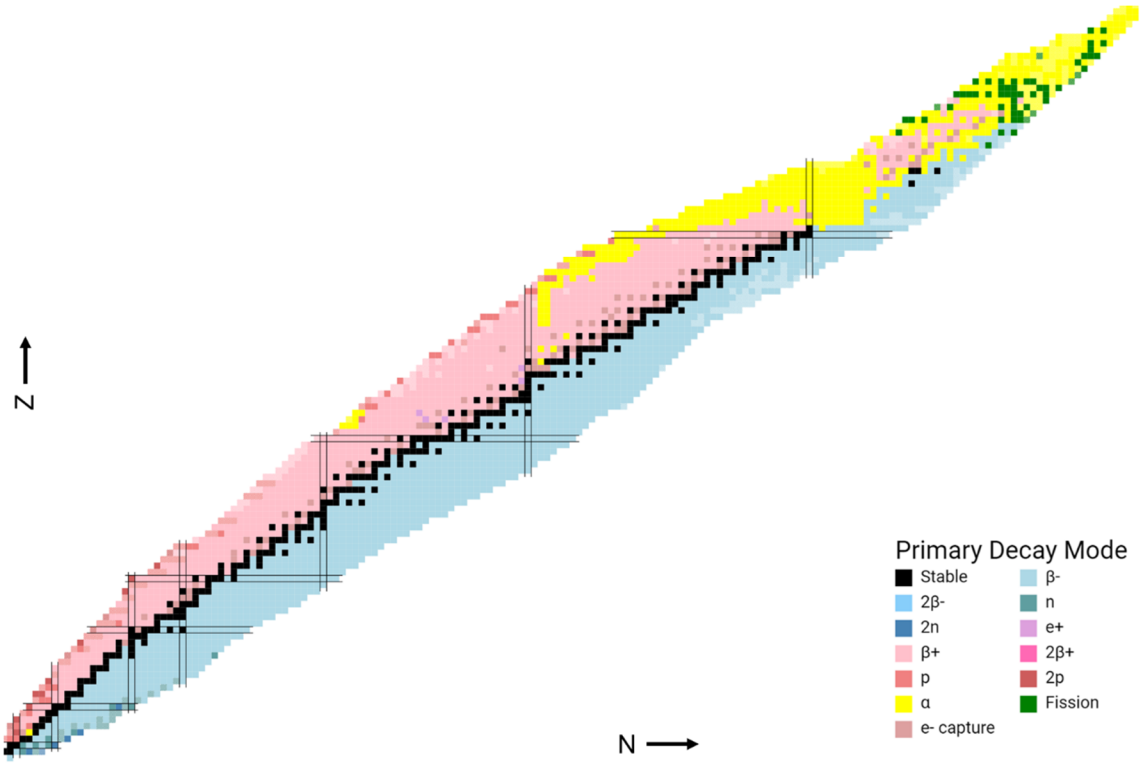

Figure 1.01. Chart of the Nuclides. Dominant decay modes across the chart of nuclides. N refers to the neutron number of a nuclide, Z its atomic number; particles are labeled as defined in the main text. Black squares represent the line of stability. Adapted with permission from (*96*).

$$ {}^{A}_{Z}X \rightarrow {}^{A-4}_{Z-2}Y + {}^{4}_{2}\alpha \tag{1.01} $$

$$ {}^{A}_{Z}X \rightarrow {}_{Z+1}{}^{A}Y^{+} + \beta^{-} + \overline{\nu} \tag{1.02} $$

$$ {}^{A}_{Z}X \rightarrow {}_{Z-1}{}^{A}Y^{-} + \overline{\beta}^{+} + \nu \tag{1.03} $$

$$ {}^{A}_{Z}X^{+} + e^{-} \rightarrow {}_{Z-1}{}^{A}Y + \nu \tag{1.04} $$

$$ {}^{A}_{Z}X \rightarrow {}^{A-i-j}_{Z-k}Y + {}^{i}_{k}W + j\,{}^{1}_{0}n \tag{1.05} $$

$$ {}^{A}_{Z}X^{*} \rightarrow {}^{A}_{Z}X + \gamma \tag{1.06} $$

1.1.1 Thermodynamics of Radioactive Decay

In order for radioactive decay to occur as written, Gibbs free energy must be released through the decay process (under constant pressure and temperature). The thermodynamics of radioactive decay may be understood through Albert Einstein's most famous equation $E = mc^2$, more appropriately written for decay processes in Equation 1.07, where H is the enthalpy of the system, m the mass of a nuclide, and c the speed of light.

$$\Delta H = \Delta mc^2 \tag{1.07}$$

The change in entropy of a radioactive decay process may be assumed negligible in comparison to its change in enthalpy; this is allowable as the reactions involve very few particles while the term Δmc^2 is enormous by comparison (*97*). Thus, ΔG may be approximated by ΔH using Equation 1.07. Therefore, radioactive decay will proceed as written if the combined masses of the daughter nuclide and its emissions are less than the mass of the parent radionuclide. It is important to note that mass is *not* conserved through a reaction, rather mass-energy is conserved. Nuclear scientists more often refer to these thermodynamic processes in terms of a Q-value, which is related to Gibbs free energy in Equation 1.08. A positive Q-value indicates that radioactive decay will occur as written.

$$Q \equiv -\Delta mc^2 = -\Delta H \approx -\Delta G \tag{1.08}$$

The energy released from the spontaneous decay of a nucleus is typically enormous, so it is most common to report Q-values in units of MeV per decay rather than kJ mol^{-1}.

1.1.2 Kinetics of Radioactive Decay

Radioactive decay is experimentally observed to follow first-order kinetics (*98*). Therefore, the rate of decay of N_1 (the "parent" nucleus) is known to be directly proportional to the number of nuclei present. In practice, this proportionality constant is defined ubiquitously as the decay constant, λ. This is shown in the fundamental law of radioactive decay, Equation 1.09, where A is defined as the activity (rate of decay) of a radionuclide.

$$-\frac{d}{dt}N_1 = A_1 = \lambda_1 N_1 \tag{1.09}$$

Equation 1.09 may be differentially solved via Equations 1.10 and 1.11 to determine the number of nuclei at time *t*.

$$\int \frac{1}{N_1} dN_1 = \int -\lambda_1 dt \tag{1.10}$$

$$\ln N_1 + C = -\lambda_1 t \tag{1.11}$$

The constant C is determined in Equation 1.12 by setting $t = 0$.

$$C = -\ln N_1(0) \tag{1.12}$$

Finally, the decay of nucleus N_1 is described as a function of time by Equations 1.13 and 1.14.

$$\ln \frac{N_1(t)}{N_1(0)} = -\lambda_1 t \tag{1.13}$$

$$N_1(t) = N_1(0)e^{-\lambda_1 t} \tag{1.14}$$

Using the fundamental law of radioactive decay (Equation 1.08), these expressions may be solved for their more common form in terms of radionuclide activity in Equation 1.15.

$$A_1(t) = A_1(0)e^{-\lambda_1 t} \tag{1.15}$$

If N_2 (the "daughter" nucleus) is not radioactive, its growth may be understood via Equation 1.16. The terms in this expression come simplified from the decay of N_1 and the initial amount of N_2 which was present at time $t = 0$. The growth of N_2 is understood to originate from the difference between the initial amount of N_1 and the amount of N_1 which remains by time t.

$$N_2(t) = N_1(0)\left(1 - e^{-\lambda_1 t}\right) + N_2(0) \tag{1.16}$$

If N_2 is radioactive, its growth may be described using Equation 1.17. The terms in this expression come from the growth of N_2 by the decay of N_1 and the loss of N_2 by its own decay into N_3 (the "granddaughter" nucleus). The terms are simplified using Equation 1.09.

$$\frac{d}{dt}N_2 = \lambda_1 N_1 - \lambda_2 N_2 \tag{1.17}$$

Assuming $N_2(0) = 0$, this expression is differentially solved to determine the number of nuclei at time t in Equation 1.18.

$$N_2(t) = N_1(0)\frac{\lambda_1}{\lambda_2 - \lambda_1}\left(e^{-\lambda_1 t} - e^{-\lambda_2 t}\right) \tag{1.18}$$

If $N_2(0) > 0$, the expression should be adjusted with an extra term (from Equation 1.14) to account for the decay of the initial nuclei as a function of time as seen in

Equation 1.19. This expression is reported in terms of activity, as it is more readily used in the radiochemistry laboratory.

$$A_2(t) = A_1(0)\frac{\lambda_2}{\lambda_2 - \lambda_1}\left(e^{-\lambda_1 t} - e^{-\lambda_2 t}\right) + A_2(0)e^{-\lambda_2 t} \tag{1.19}$$

Radioactive nuclei far from the line of stability will often have long decay chains involving multiple radioactive decay daughters. The growth of a radioactive daughter N_n may be determined by differentially solving Equation 1.20.

$$dN_n = \lambda_{n-1}N_{n-1}dt - \lambda_n N_n dt \tag{1.20}$$

The differential solutions become increasingly complex as the decay chain progresses; however, a general solution to these problems exists, known as the Bateman Equations. As written, the Bateman Equations solve for the activity of radionuclide N_n in a decay chain at least $n+1$ nuclides long. The activity of radionuclide N_n is solved in Equation 1.21 based on a parameter *c* which is described in Equation 1.22 where *i* and *m* are indices starting at 1.

$$A_n = N_1(0)\sum_{i=1}^{n}(c_i e^{-\lambda_i t}) \tag{1.21}$$

$$c_m = \frac{\prod_{i=1}^{n}\lambda_i}{\prod_{i=1}^{n}(\lambda_{i\neq m} - \lambda_m)} \tag{1.22}$$

1.1.3 Neutron Capture

While radioactive decay occurs without the influence of external stimuli, induced nuclear reactions may *only* occur under the influence of external stimuli. Some of the common nuclear reactions reviewed in modern literature include Coulomb scattering reactions, elastic and inelastic scattering reactions, direct

reactions, photonuclear reactions, fusion-evaporation reactions, spallation, neutron capture, and nuclear fission (*99*). The two reactions which are most important in the scope of nuclear forensics are neutron capture and nuclear fission.

Neutron capture describes a process where a projectile neutron is absorbed into a "target" nucleus. Before a neutron may be captured by a nucleus, the wave functions of the two systems must overlap. As a fermion, neutrons are subject to wave-particle duality through the de Broglie wavelength as described in Equation 1.23 where h is Planck's constant and p the neutron's momentum. In this case only, λ refers to the de Broglie wavelength of a particle.

$$\lambda = \frac{h}{p} \tag{1.23}$$

As a single particle, the "interaction radius" of a neutron is a function of its single wavefunction. If the wavefunction of a neutron is a function of its de Broglie wavelength, then Equation 1.23 suggests that the interaction space between a neutron and a nucleus should decrease as the neutron's kinetic energy increases, resulting in a lower total cross section for neutron capture at high neutron energies. Indeed, this trend is observed in neutron capture reactions as demonstrated by the $^{1}H(n, \gamma)^{2}H$ reaction in Figure 1.02 (*100*). The reaction scheme used here indicates that a neutron is incident on ^{1}H, a photon is ejected, and ^{2}H is produced as the final reaction product.

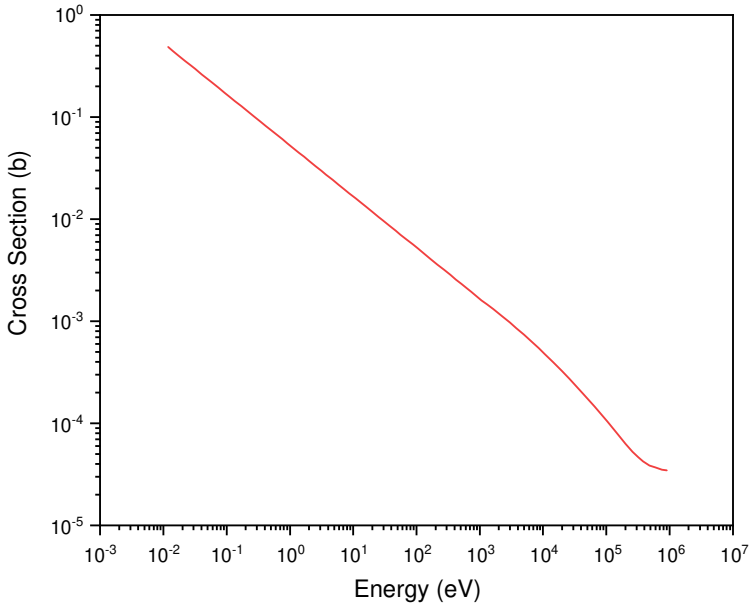

Figure 1.02. Cross Sections of the $^{1}H(n, \gamma)^{2}H$ Reaction. Cross section as a function of energy for neutron capture on a proton. Cross section is observed to decrease exponentially with increasing neutron energy. No resonances are observed for this reaction because the nuclear excited states in ^{2}H are too high in energy. Cross sections originate from EXFOR as extracted through the NGATLAS interface (*100*).

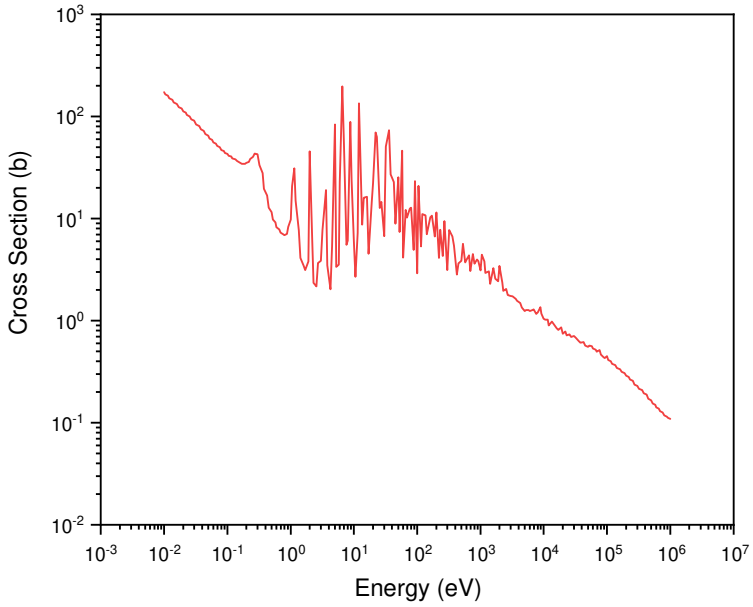

Figure 1.03. Cross Sections of the $^{235}U(n, \gamma)^{236}U$ Reaction. Cross section as a function of energy for neutron capture on ^{235}U. Cross section is still observed to decrease exponentially with increasing neutron energy. However, in this case neutron resonances are observed for this reaction because the nuclear excited states in ^{236}U are readily accessible. Cross sections originate from EXFOR as extracted through the NGATLAS interface (*100*).

Neutron energies around 0.025 eV are considered “thermal” at the Boltzmann constant (kT) at room temperature, while neutrons are considered “fast” at energies above 1 MeV as they are typically released during the fission process. As observed in Figure 1.02, thermal neutrons are far more likely to be captured by a target nucleus. A major consequence of this phenomenon is that moderators are used to reduce neutron energy towards its thermal limit when neutron capture is a desired process. Common moderators used in the nuclear industry include light water ($^{1}H_2O$), heavy water ($^{2}H_2O$), graphite, and carbon-based plastics. These low Z materials are effective at moderating neutron energies towards their thermal limit because their mass is similar to that of a neutron, allowing effective kinetic energy transfer through the conservation of momentum.

Most neutron capture reactions experience resonance regions where the capture cross section increases dramatically over small energies regions, as seen in the $^{235}U(n, \gamma)^{236}U$ reaction in Figure 1.03 (*100*). The kinetic energy of the neutron projectile is transformed into excitation energy within the compound nucleus formed after successful capture; within the resonance regions, this excitation energy aligns with excited states of the newly formed nucleus.

Neutron capture is the favored production pathway to synthesize actinide elements. Nuclear reactors are used as large neutron sources of high flux to facilitate the neutron capture and successive β^- decays of U to produce isotopes of Pu and the minor actinides.

1.1.4 Nuclear Fission

The examples of neutron capture presented so far ultimately result in the emission of a photon as the excited compound nucleus returns to rest. However, several other emissions are possible. These other possibilities include particle emissions of protons, alpha particles, and multiple neutrons; the most important emission to nuclear forensics is nuclear fission.

In general, nuclei are held together through the effects of the strong force via subatomic particle interactions (*101*). In bound nuclei, these effects create an attraction between nucleons (protons or neutrons) which overcomes the repulsive Coulombic force between protons. The strength of these effects depends upon the number of neighboring nucleons. It follows then, that the strength of the strong force will weaken as a nucleus deforms, increasing the energy of the nucleus.

Before a single nucleus may fission into two independent nuclei, it must deform significantly from its ground state conformation, requiring energy to be added into the system as seen in Figure 1.04 (*102*). This energy is called the fission barrier and must be overcome before nuclear fission may occur. The compound nucleus formed immediately after neutron capture carries with it some amount of excitation energy resulting from the Q-value of the capture process. If this excitation energy is greater than the fission barrier of the nucleus, nuclear fission becomes an allowable process in competition with the other modes of photon and particle emission discussed.

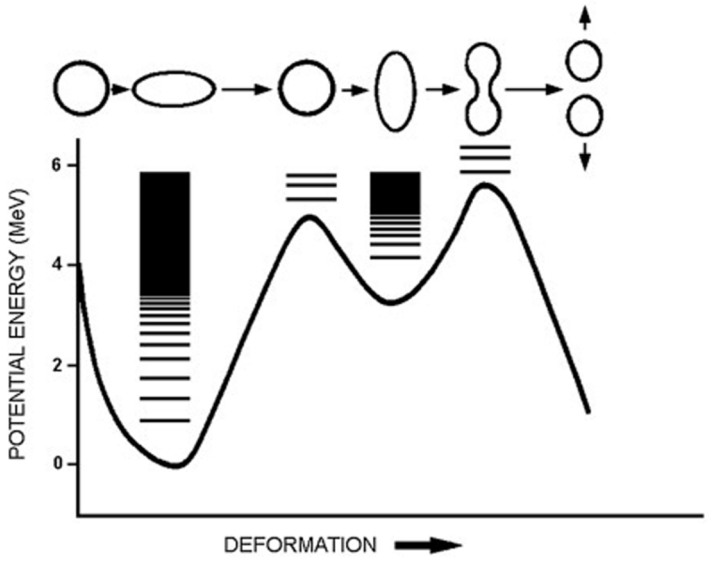

Figure 1.04. Deformation of a Fissioning Nucleus. Reaction coordinate describing the process by which a nucleus may fission. The initial system exists within the "nuclear well" at a low potential energy with minimal deformation; energy is required to deform the nucleus as it deviates from its idealized geometry. The final saddle point marks the first point where the system begins to resemble two independent nuclei and fission becomes a favorable process. This "double well" model correctly predicts asymmetric fission. Adapted with permission from (*102*).

In nuclides of $Z = 92, 94$ (U and Pu), the excitation energy provided from fast neutrons is generally sufficient to overcome the barrier. This makes fast neutron fission possible, but unlikely due do its lower cross section for capture.

The semi-empirical mass formula (Equation 1.24) is an accepted model in nuclear science used to describe the amount of binding energy associated with any given nuclide. The constants a_V, a_S, a_C, and a_A are associated with the strong force, surface energy, Coulombic forces, and nucleon symmetry, respectively.

$$E_B = a_V A - a_S A^{2/3} - a_C \frac{Z(Z-1)}{A^{1/3}} - a_A \frac{(A-2Z)^2}{A} - \delta(N,Z) \qquad (1.24)$$

The final term $\delta(N, Z)$ is often referred to as the pairing energy and describes greater binding energies for nuclei with an even number of either neutrons or protons. This effect is understood through the attractive interaction of paired nucleons.

If the initial nucleus of a fissioning system has an odd number of neutrons, the capture process releases some additional energy associated with the stability of obtaining an even number of neutrons in the newly formed compound nucleus. This additional energy is sufficient to allow for thermal neutron fission in odd neutron *Z = 92, 94* nuclides. These thermal neutron fissions have much higher cross sections than the competing fast neutron fissions, as the thermal neutrons have a much larger de Broglie wavelength.

This effect gives rise to the "fissile" nature of ^{233,235}U and ^{239}Pu which are known to readily undergo nuclear fission upon capture of thermal neutrons. The thermal neutron fission cross section of the fissile odd neutron ^{235}U nucleus is on the order of 10^3 b, while the fast neutron fission of the even neutron ^{238}U nucleus approaches 10^{-1} b. These trends are shown in Figures 1.05 and 1.06 (*103*). Fissile nuclides are extremely attractive for applications in nuclear reactors and nuclear weapons which reply upon the energy released from fission.

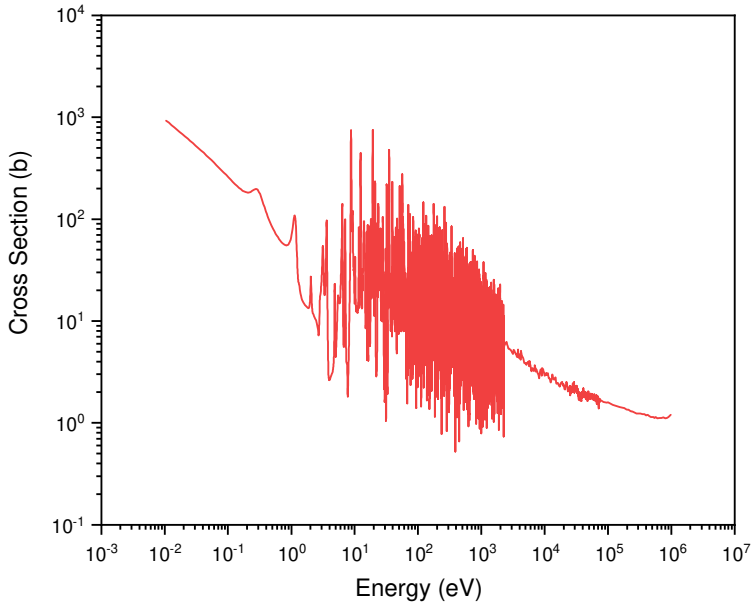

Figure 1.05. Cross Sections for the Neutron-Induced Fission of ^{235}U. Thermal neutron induced fission is a likely process in the fissile ^{235}U nucleus because of the pairing effect. The thermal fission cross section reported here is approximately 10 times higher than the thermal ^{235}U(n, γ)^{236}U reaction from Figure 1.3, making fission the dominate reaction pathway upon thermal neutron capture. Neutron-induced fission cross sections originate from ENDF (*103*).

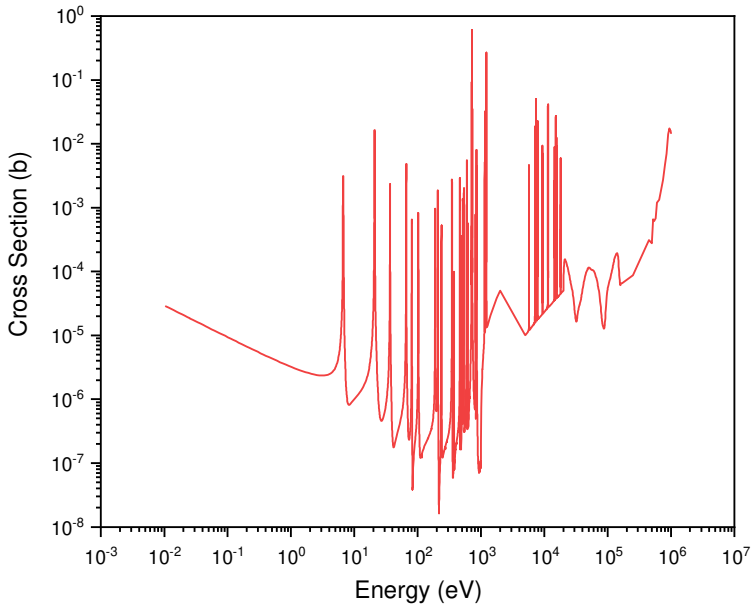

Figure 1.06. Cross Sections for the Neutron-Induced Fission of ^{238}U. Thermal-neutron-induced fission of ^{238}U is extremely unlikely as the compound nucleus does *not* contain enough energy to overcome the fission barrier. The fast neutron fission cross section of ^{238}U is approximately 4 orders of magnitude lower than the thermal fission cross section of ^{235}U due to the small de Broglie wavelength of fast neutrons. Neutron induced fission cross sections originate from ENDF (*103*).

The semi-empirical mass formula can be used to estimate the binding energy per nucleon (E_B/A) of nuclei across the chart of nuclides. The E_B/A is plotted for the most stable nuclides of each mass between 1 – 250 amu in Figure 1.07 (*97*). This trend reveals why nuclear fission of heavy nuclei such as U and Pu releases energy; The initial nucleus fissions into two nuclei with relatively higher E_B/A. The fission of these heavy nuclei releases approximately 200 MeV of energy, most of which is carried away as kinetic energy in the resulting fission fragments. Similar to spontaneous fission from Equation 1.05, the nuclear fission process releases two asymmetric nuclei and between 1 – 3 fast neutrons with approximately 1 MeV of kinetic energy each.

The independent fission yields for the thermal (0.025 eV), epithermal (500 keV), and fast (14 MeV) neutron fissions of ^{235}U are shown in Figure 1.08 (*104*). The fission yields are asymmetric in each case, but the thermal fissions are the most asymmetric. In general, the distribution of FPs in irradiated fissile material serves as an indication as to how the material was irradiated. The cumulative fission yields will deviate from Figure 1.08 as the FPs undergo their own neutron capture and radioactive decay.

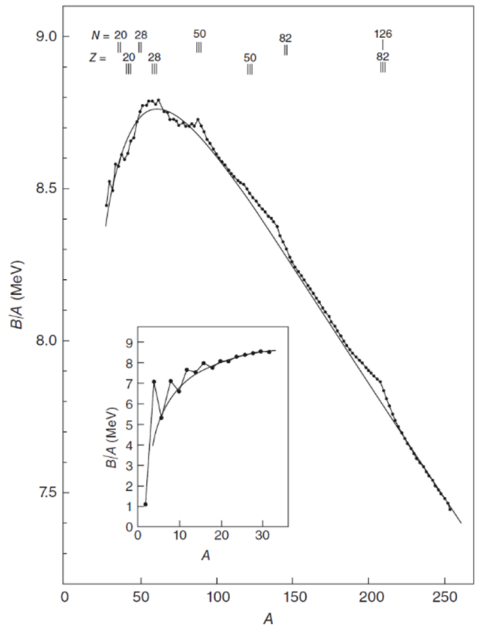

Figure 1.07. Binding Energy Per Nucleon up to Mass 250. The binding energy per nucleon is seen to decrease as mass increases beyond its peak around ^{56}Fe. This is a result of the Coulombic repulsion from the increasing number of protons. This chart describes how the fusion of light nuclei releases energy while the fission of heavy nuclei also releases energy. Presented with permission from (*97*).

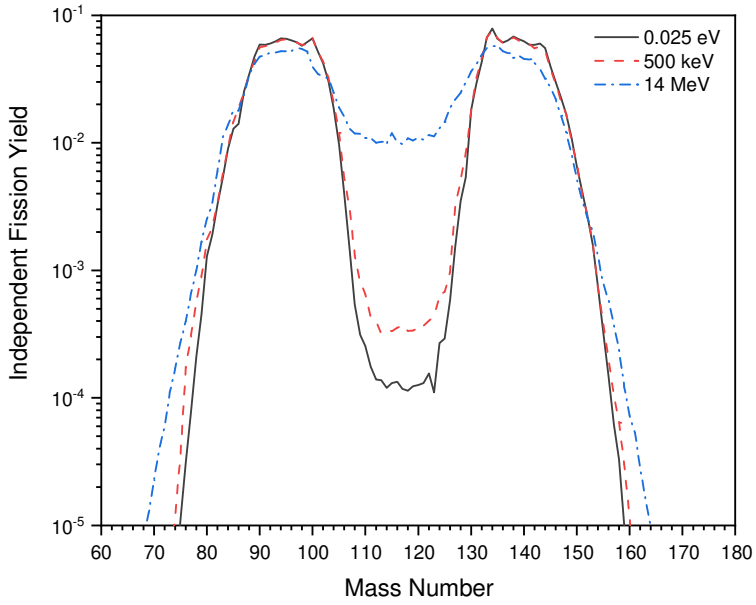

Figure 1.08. Independent Fission Yields of ^{235}U. Fission product distribution is shown to be a function of incident neutron energy. Thermal neutrons produce the most asymmetric fission products while fast neutrons of 14 MeV produce the least asymmetric fission products. The distribution of fission products as measured in a sample may reveal information about the way the sample was irradiated. Independent fission yields originate from JENDL (*104*).

1.1.5 Radiation Detection

Modern radiation detectors are made for a variety of applications. Some of these applications include radioactive source surveys, medical imaging procedures, charged particle reactions, and neutron and photon spectrometry. The radiation detectors employed herein for nuclear forensics are semi-conductors for high resolution α and γ spectrometry.

As charged particles, α particles are able to interact directly with a semi-conducting medium through the electromagnetic force. Uncharged photons, however, cannot be directly detected by a semi-conductor; to be detected, a photon must first interact with the semi-conductor to produce a charged particle. The charged particle is then detected by the semi-conductor through electromagnetic interactions. The four dominant interactions between light and matter here are Rayleigh scattering, the photoelectric effect, Compton scattering, and pair production. The cross section of each interaction is a function of photon energy as depicted in Figure 1.09 (*105*).

Rayleigh scattering describes the elastic scattering of photons by an atom which leaves the energy of the photon unchanged. This interaction has no capability of producing a signal in a semi-conducting detector. The photoelectric effect describes the complete transfer of energy from an incident photon into a semi-conducting medium via the ejection of a photoelectron. This photoelectron carries away all of the energy from the incident photon minus the binding energy of the photoelectron and is able to interact with the semi-conducting medium.

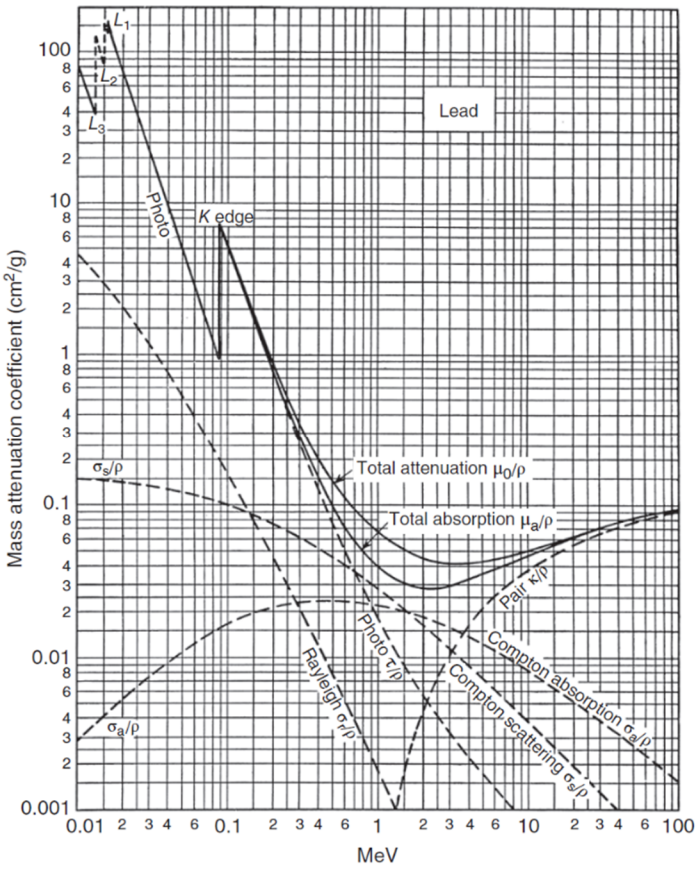

Figure 1.09. Interactions Between Light and Matter. This figure describes the energy dependence of the cross sections for Rayleigh scattering, the photoelectric effect, Compton scattering, and pair production. The desired interaction for radiation detection is the photoelectric effect; its cross section drops off rapidly with increasing photon energy. Presented with permission from (*105*).

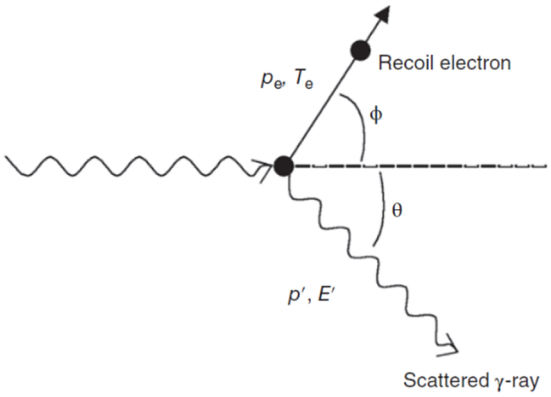

Figure 1.10. The Compton Scattering Interaction. Schematic for the Compton scattering of a photon across an atom. The energy of the scattered photon is a function of its scattering angle θ. The maximum energy imparted into the Compton electron occurs at the greatest scattering angle of 180°. Presented with permission from (*105*).

The photoelectron produces a prominent peak in a γ spectrum called the photopeak which is representative of the incident photon's energy.

Compton scattering describes the incomplete transfer of energy from an incident photon into a semi-conducting medium via the ejection of a Compton electron. The incident photon is scattered at an angle θ depending upon the amount of energy transferred into the Compton electron. These effects are described in Figure 1.10 (*105*) and Equation 1.25 where λ_γ refers to the incident wavelength of the photon, λ_γ' refers to the wavelength of the scattered photon, and m_e is the mass of the electron.

$$\lambda_\gamma' - \lambda_\gamma = \frac{h}{m_e c}(1 - \cos\theta) \tag{1.25}$$

The maximum amount of energy carried by the Compton electron occurs at a scattering angle of 180°, at an energy of $E_\gamma - 0.255$ MeV per Equation 1.25. This feature is prominent on a γ spectrum and results in a peak called the Compton edge.

Pair production describes a process where a photon with energy greater than 1.022 MeV spontaneously creates an electron-positron pair in the vicinity of a nucleus; positrons are the anti-particle of an electron. The minimum energy of pair production is specific as the photon's energy must be greater than the sum of the rest masses of the generated particles, which is 0.511 MeV/c^2 each. Pair production must occur in the vicinity of a nucleus to conserve momentum with the newly created particles. The positron produced may annihilate with a nearby electron producing

two 0.511 MeV photons, which may then produce prominent peaks on a γ spectrum through photoelectric and Compton scattering interactions.

The most desirable of these interactions is the photoelectric effect, as it produces a photopeak which is representative of the incident photon's energy, while Compton scattering and pair production convolute the spectrum. The cross section of the photoelectric effect may be estimated as a function of incident photon energy (E_γ) and atomic number of the absorber (Z) from Equation 1.26 where n represents an exponent between 4 and 5 (*105*).

$$\sigma_{photoelectric} \propto \frac{Z^n}{E_\gamma^{7/2}} \tag{1.26}$$

The photoelectric effect is dependent upon the atomic number of the absorber because the number of electrons in the absorber increases with atomic number (*105*). This effect makes high Z materials attractive as photon detectors and photon radiation shields.

After production of the photoelectron or Compton electron, the detection pathway for photons and α particles becomes identical within a semi-conducting radiation detector. Charged particles propagating through a semi-conductor create a number of electron-hole pairs within the semi-conductor proportional to the energy of the charged particle. The bandgap in a semi-conductor describes the minimum amount of energy needed to create an electron-hole pair, not the average energy. The average energy is significantly larger than the bandgap because not all electrons within the semi-conductor exist within its valence band. For Si semi-conductors, the

bandgap is 1.1 eV while the average electron-hole pairing energy is 3.6 eV. For Ge semi-conductors, these energies are 0.66 and 2.9 eV, respectively (*106*).

The lower electron-hole pairing energy of Ge creates more electron-hole pairs for a given incident particle energy, resulting in better resolution compared to Si detectors. However, the bandgap of Ge is sufficiently small such that room temperature perturbations within the semi-conducting crystal provide enough energy to promote electrons into its conductance band. This produces a significant amount of noise; practically, a Ge semi-conductor must be cooled with liquid N_2 to minimize this noise. Even then, a cooled Ge semi-conductor produces approximately 50% more ambient noise than a Si semi-conductor (*106*). Thus, Si detectors are the most widely used detectors for α spectrometry, capable of producing a full width at half-maximum (FWHM) of approximately 20 keV. However, the atomic number dependence for the photoelectric effect described in Equation 1.26 indicates that Ge would make a better photon detector with higher intrinsic efficiency. Indeed, Ge detectors cooled with liquid N_2 are used preferentially over Si detectors for γ spectrometry and produce photopeaks with a FWHM typically between 1 – 2 keV.

Electron-hole pairs must be created within the depletion region of a doped semi-conductor at its p-n junction; if electron-hole pairs are created outside of the depletion region, they experience rapid recombination. The width of the depletion region (d) is a function of bias, per Equation 1.27 where ρ is the resistivity of the material and V is the applied bias (*106*).

$$d \propto (\rho V)^2 \tag{1.27}$$

An acceptable depletion width is obtained for α spectrometry at a bias between 20 – 200 V; in part because of its low photoelectric cross sections, γ spectrometry requires much higher biases up to 5,000 V to maximize the depletion width and intrinsic detection efficiency.

Upon creation in the depletion region, electron-hole pairs are drawn off to an electrode where they create a current proportional to the number of electron-hole pairs. This creates a voltage signal across a resistor with peak height proportional to the current. This signal is amplified, shaped, and binned into appropriate channels with the use of a pre-amplifier, amplifier, and multi-channel analyzer. This process allows the multi-channel analyzer to report the number of detected events per channel in a spectrum, where each channel may be calibrated to an energy range by the user. Because the photoelectric cross section changes as a function of energy, efficiency calibrations must also be performed to characterize the efficiency of the detector as a function of energy in γ spectrometry. This efficiency curve is flat for α spectrometry as there is no pre-requisite photoelectric interaction.

These radiation detectors have a "dead time" (τ) between detectable events where they cannot accept any other detectable events. As non-paralyzable detectors, the dead time per event depends upon the electronics of the detector and is independent of the event rate. Thus, the detected event rate (R_{obs}) may be readily corrected via Equation 1.28 where R is the true event rate and τ/t represents the fraction of dead time per total real time.

$$R = \frac{R_{obs}}{\left(1 - \frac{\tau}{t}\right)} \tag{1.28}$$

In practice, spectra were only accepted in this work if the fractional dead time remained below 20%.

1.2 Analytical Separations of Fission Products and the Actinide Elements

Radiochemists have been involved in weapons programs since the Manhattan Project (*107*). In the earliest days of weapons science, radiochemists sought to unravel the chemistry of the newly discovered element Pu (*108, 109*); working with trace quantities of 1 μg or less, they learned about its fundamental properties such as favorable oxidation states, solubilities, and extraction behavior (*110, 111*). Their primary role at this stage was to understand how to extract Pu from irradiated U, purify it to the necessary specifications, and reduce it to its metallic form for use in a weapon.

After weapons testing began, radiochemists took upon another role: investigating the distribution of actinides and FPs in detonation debris to evaluate the effectiveness of the tested weapon (*107*). These tasks required the development of sophisticated procedures to separate and isolate individual FPs and actinide elements, an effort which continues today. The most widely employed separation methods are column chromatography and liquid-liquid extractions.

1.2.1 Column Chromatography

Column chromatography is a form of liquid-solid extraction where a stationary phase forms a resin bed supported in a column made of plastic, metal, or glass. The resin is carefully chosen to support the chromatography method; separations of inorganic species supported by modern resins include ion exchange, ion exclusion, size exclusion, and extraction chromatographies (*112*). Glass and plastic columns are used for systems under atmospheric pressure, while metal columns are used for high pressure systems in high-performance liquid chromatography (HPLC). The liquid phase is typically referred to as the mobile phase. In some cases, ligands may be added to the mobile phase to enhance separation.

Solvated species interact with both the stationary phase and mobile phase as shown in Figure 1.11. Species which preferentially interact with the stationary phase take longer to elute, while species which preferentially interact with the mobile phase elute quickly. In some separations, the phases are chosen such that a species remains absorbed to the stationary phase indefinitely until the mobile phase is changed. These interactions provide the basis of separation for all forms of column chromatography. The stationary and mobile phases are always carefully chosen to maximize these interactions for specific species in order to produce the greatest separation.

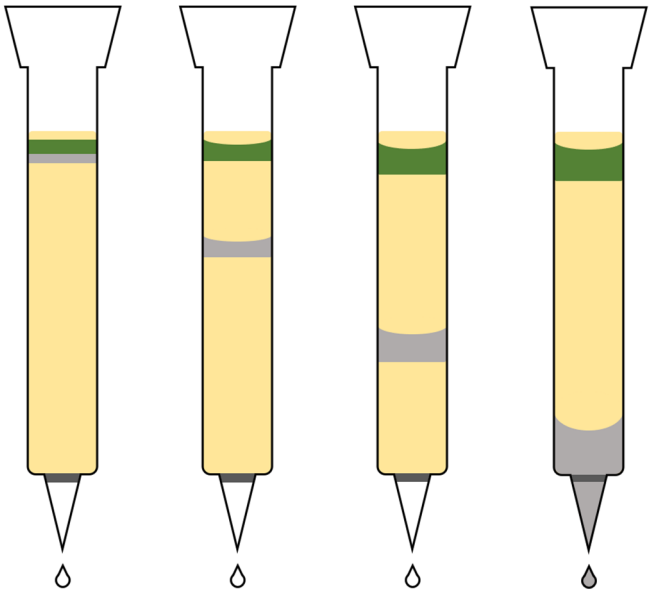

Figure 1.11. Chromatographic Separations. A schematic representation of the separation of two species via column chromatography. Specifically, this example illustrates the separation of Pu^{IV} (green) from fission products (gray) on anion exchange resin (yellow) in 8 M HNO_3. The distribution band of all species will broaden as the total volume of mobile phase eluted increases. Pu^{IV} has an extremely high capacity factor > 10^4 under these conditions; while its band will broaden, it will not move down the column.

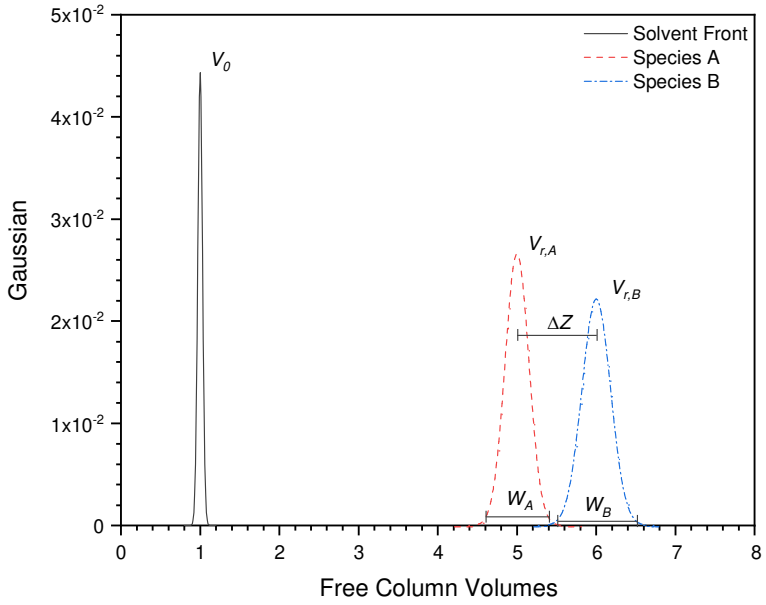

Figure 1.12. Elution Parameters of a Chromatogram. Chromatogram showing the separation of arbitrary species A and B. The mobile phase is seen to first break through with the solvent front at 1 free column volume; this is the smallest volume where anything may elute from the column. Species A and B are shown to elute at retention volumes of $V_{r,A}$ and $V_{r,B}$ with base widths of W_A and W_B, respectively. Along with the difference in retention volumes (ΔZ), these parameters may be used to measure the separation resolution.

The resin is formed of small spherical particles packed closely together. The space between the packed resin particles is referred to as the dead volume, void volume, or free column volume (FCV). In a system of perfectly arranged spheres of equal size, the minimum FCV mathematically possible is approximately 26%. In practice, randomly packed spheres produce a FCV on the order of 35 – 40% (*113*). The FCV of a column marks the minimum volume of mobile phase that must pass through the column before any analyte may be eluted.

The number of FCVs required to elute a given species is defined as the capacity factor (k') and is calculated in Equation 1.29 where V_r is the retention volume of the species and V_0 is the FCV, as depicted in Figure 1.12.

$$k' = \frac{V_r - V_0}{V_0} \tag{1.29}$$

These capacity factors are an extremely useful tool used to understand the separation performance of a column while planning its design. Ideal capacity factors for favored solute-stationary phase interactions are on the order of 10^2 – 10^4, while capacity factors for favored solute-mobile phase interactions are on the order of 10^{-2} – 10^0.

Separation resolution (R_s) provides a quantitative measure of the separating power of a column. Resolution is a function of the inter-centroid distance between the two species (ΔZ) and the width of their bases (W_A, W_B) at 5 or 10% of their peak height (Figure 1.12), as described in Equation 1.30 (*114*).

$$R_s = \frac{2\Delta Z}{W_A + W_B} \tag{1.30}$$

These parameters are shown in Figure 1.12 with complete separation at $R_s > 1.5$.

1.2.2 α-Hydroxyisobutyric Acid as a Mobile Phase for Lanthanide Separations

Lanthanide (Ln) elements are produced as FPs during the irradiation of U and Pu in reactors and weapons (Figure 1.08). Several of these Ln elements have isobars which cannot be resolved by a standard mass spectrometer and require separation prior to assay (*44*). The extraction behavior of all Ln elements is remarkably similar; this is due in part to their ions' dominantly trivalent nature and unfilled 6s and 5d orbitals (*115, 116*). Most extractants are not able to separate these elements through liquid-liquid extractions or column chromatography. One successful ligand which has been widely used to facilitate the separation of the Ln elements through column chromatography is α-hydroxyisobutyric acid (α-HIB) (*44, 117-128*).

A significant difference between each of the Ln elements is the trend of decreasing ionic radius with increasing atomic number (*129-132*). This trend is presented in Figure 1.13 where the Ln – O bond length in $Ln{\cdot}H_2O$ is reported as a function of f electrons (*129*). This causes the charge density of the trivalent Ln ions to increase with atomic number and is often referred to as the Ln contraction; in general, the higher atomic number Ln elements will be more strongly coordinated to a given ligand. A similar contraction is seen through any given period across the periodic table. These contractions result from adding electrons to valence shells which are relatively shielded from the increasing nuclear charge. The Ln contraction is particularly pronounced as electrons are added to the diffuse inner 4f orbitals.

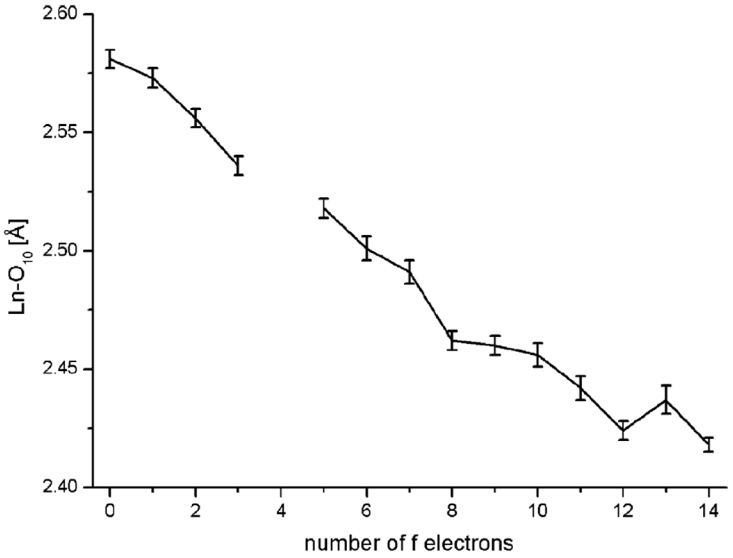

Figure 1.13. The Lanthanide Contraction. Bond length of the Ln – O bond in Ln·H_2O. Bond length is shown to decrease as the number of f electrons in the Ln atom increases. This establishes the trend often called the Ln contraction. A similar contraction exists within any given period across the entire periodic table, but this contraction is exaggerated as electrons are added to the diffuse 4f orbitals. Presented with permission from (129).

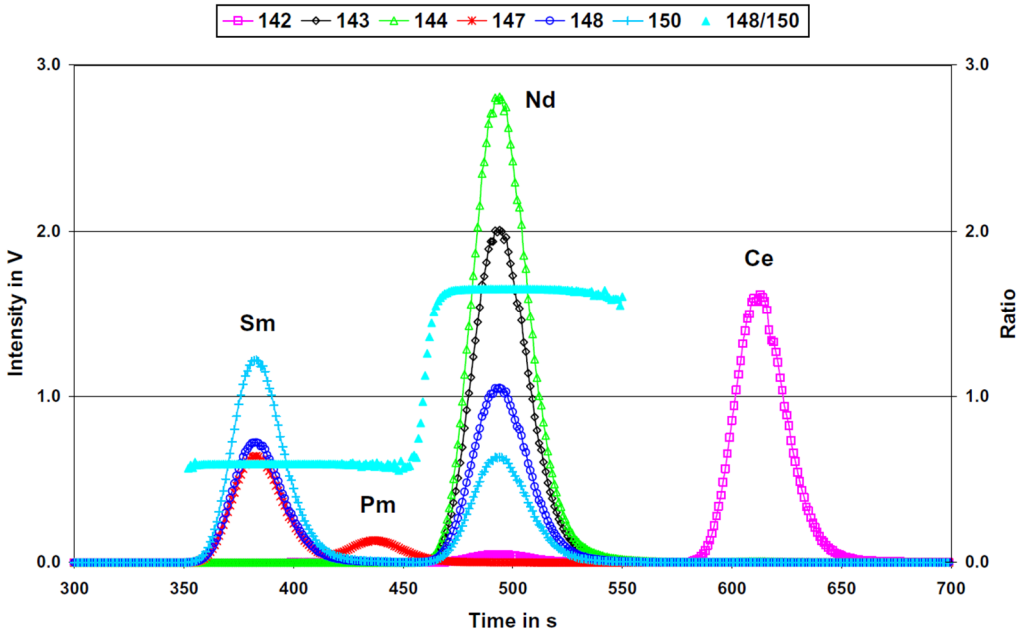

Figure 1.14. Separation of the Lanthanide Elements. The α-HIB ligand is shown to separate some Ln elements in order of decreasing atomic number. Mass bin intensities are read from the left axis, mass bin ratios from the right axis. The higher atomic number Ln elements have a greater charge density and coordinate to the α-HIB ligand more strongly, which facilitates their elution. Completely resolved separations such as presented here are typically only accomplished using an HPLC. Presented with permission from (127).

The α-HIB ligand exploits this difference in charge density to separate the Ln elements on cation exchange resins. The conjugate base of the α-HIB ligand will coordinate with the Ln elements to form species in a dynamic equilibrium between $Ln(\alpha\text{–}HIB^{-})_2^{+}$ and $Ln(\alpha\text{–}HIB^{-})_4^{-}$ (*133*). The Ln elements with lower charge density will exist in the cationic form more often, allowing them to interact with the anionic stationary phase. The Ln elements with higher charge densities will exist in the neutral and anionic forms more often and will elute with the mobile phase. Thus, α-HIB facilitates the separation of Ln elements on cation exchange resin in elution order of decreasing atomic number, as seen in Figure 1.14 (*127*).

In these separations, Ln elution is dependent upon its coordinated speciation with the α-HIB conjugate base. As a result, the concentration of α-HIB and the pH of the mobile phase have a strong impact on the effectiveness of the separation. The separation resolution between Er and Tm is shown as a function of conjugate base concentration in Figure 1.15 (*124*). If the concentration of the conjugate base becomes too high, no separation will be observed. The concentration of the conjugate base may be calculated through the Henderson-Hasselbalch equation, reported as Equation 1.31. The pK_a of α-HIB is approximately 3.7 (*134*); A^- corresponds to its conjugate base, *HA* to its acidic form.

$$pH = pK_a + \log\frac{[A^-]}{[HA]} \tag{1.31}$$

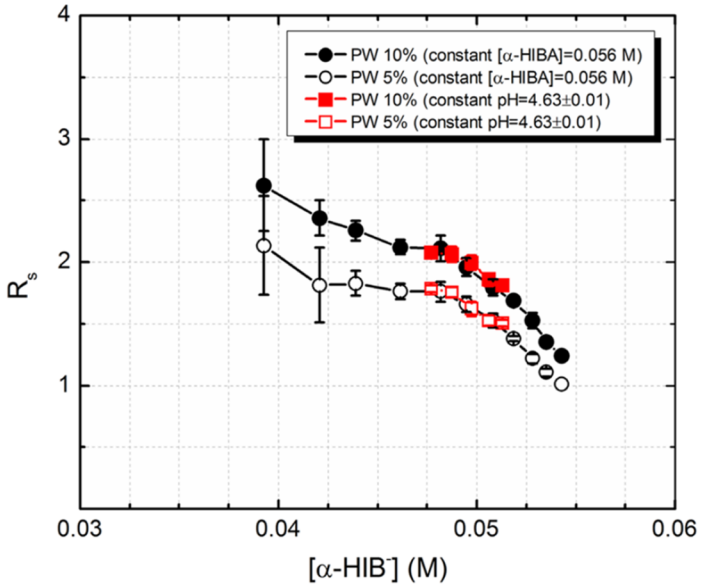

Figure 1.15. Concentration and pH Dependence of α-Hydroxyisobutyric Acid. The separation resolution of the Er, Tm separation by α-HIB is reported as a function of conjugate base concentration. In general, the greater the concentration of the conjugate base, the worse the separation becomes. If the concentrate of the conjugate base is too high, no separation will be apparent. Presented with permission from (124).

1.2.3 Ion Exchange and Extraction Resins as Stationary Phases for Actinide Separations

Actinides (An) are produced as transmutation products through successive neutron captures and β^- decays during the irradiation of U and Pu in reactors and weapons. Unlike the Ln elements, the An elements experience significant relativistic effects due to their large nuclear charge. These effects contract their s and p orbitals while destabilizing their d and f orbitals, and result in pronounced spin-orbit coupling of their valence orbitals (*135-141*). Combined, these effects allow for the early An elements (up through Pu) to access more than just the trivalent oxidation state available to their analogous Ln elements. Therefore, separation of the An elements up through Pu is relatively easy; separations of the trivalent An elements

from Am and beyond is challenging, just like the Ln elements. While some success has been obtained using α-HIB for the trivalent An elements (*142-144*), most An separations are focused on separating Th, U, Np, Pu, and Am from each other and FP elements.

The resins most commonly used for the chromatographic separation of the An elements include ion exchange and extraction resins (*145-149*). The extraction resins typically favored include UTEVA (*150-155*), TEVA (*156-160*), TRU (*161-165*), AN (*166-169*), LN (*170, 171*), and SR (*172-175*) resins by Eichrom. Figure 1.16 (*147*) shows how an anion exchange resin may be used to separate Pu from FPs and the other An elements in nitric acid; many of these figures exist for multiple ion exchange and extraction resins and may be used to design a desired separation.

While the older references in this area are still valid, they tend to report extraction behavior in terms of the partition coefficient (K) instead of the capacity factor (k'). This was typically done out of convenience since the extractions were performed in batch studies using resin in a beaker, instead of on columns. The partition coefficient is described in Equation 1.32 and may be converted to the capacity factor using Equation 1.33. In these equations, m is mass, and V is volume; subscript s refers to the stationary phase, while subscript m refers to the mobile phase.

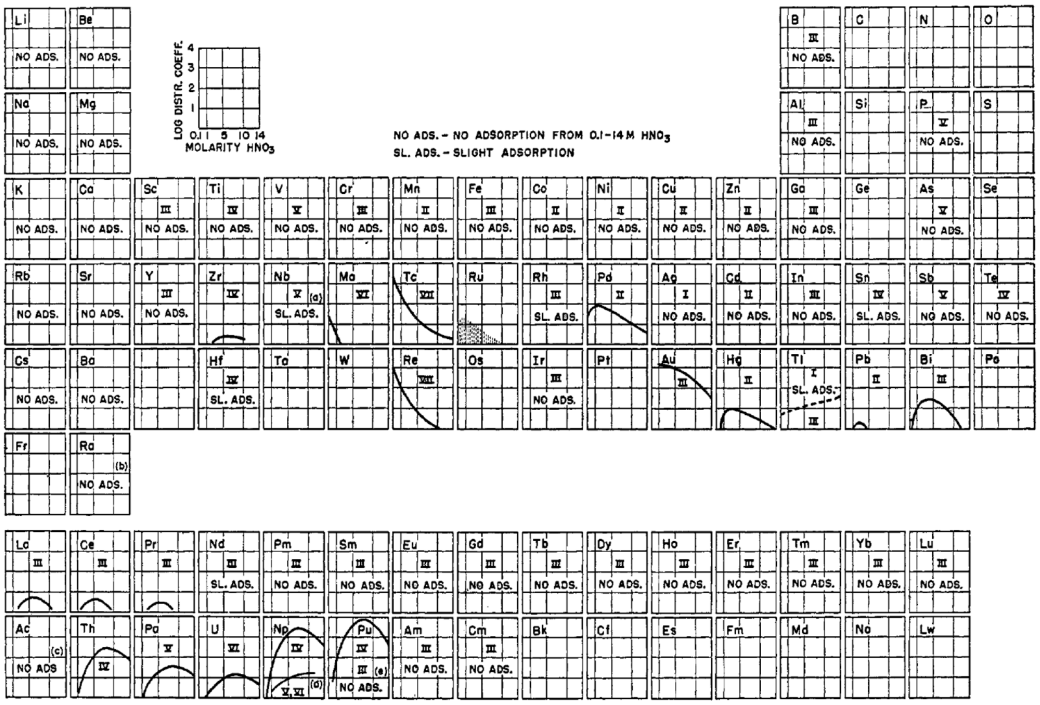

Figure 1.16. Separation of the Elements with Nitric Acid on Anion Exchange Resin. Partition coefficients of most elements in nitric acid on anion exchange resin. Many figures of this manner exist for multiple resins and mobile phases; they may be used to design separations of many different elements. This figure is particularly useful for separating Pu from other elements. Presented with permission from (147).

$$K = \frac{m_s/V_s}{m_m/V_m} \tag{1.32}$$

$$k' = K\frac{V_s}{V_m} \tag{1.33}$$

1.3 Forensic Signatures and Observables

The most common pre-detonation forensic observables investigated in the nuclear industry today include chronometry (*25-40*), isotopic and radiopurity evaluations (*41-50*), reactor discrimination (*51-64*), trace metal analysis (*65-72*), and sample morphology and composition studies (*73-85*). Additionally, post-detonation forensics investigates materials which have been exposed to a nuclear detonation to determine the composition and origin of a detonating device (*86-95*).

These observables are determined by measuring the signatures they impart into a sample; these signatures typically include inter- and intra-elemental nuclide ratios, trace metal abundance, particle size distributions, and molecular excitations, vibrations, and stretches. These signatures are measured using a combination of instrumental techniques including radiation detection, mass spectrometry, atomic emission, x-ray fluorescence (XRF), UV-vis spectrometry, FTIR and Raman spectroscopy, scanning and transmission electron microscopies (SEM and TEM), and atomic force microscopy (AFM).

1.3.1 Mass Spectrometry in Nuclear Forensics

Mass spectrometry is widely applied in nuclear forensics to measure sample isotopics and assay trace metal content (*18, 19*). The most common modes of mass spectrometry used in forensics are inductively coupled plasma mass spectrometry (ICP-MS) and thermal ionization mass spectrometry (TIMS). These techniques are highly valued in forensics because they can be used to measure sample isotopics with

high sensitivity and precision. A mass spectrometer is generally made up of four sections: sample introduction, sample ionization, mass analysis, and detection.

In ICP-MS, samples are generally prepared solvated in 1 – 2% HNO_3 (v/v); these samples are introduced to a "spray chamber" as an aerosol using a nebulizer and a peristaltic pump. A small portion of the aerosol is transferred to the ionization chamber through a small pressure differential in the instrument. It is also possible to assay solid samples with ICP-MS using laser ablation (LA-ICP-MS). In laser ablation instruments, a high intensity laser is used to irradiate the surface of a solid substrate, evaporating some portion of the surface. These evaporated atoms are carried into the ionization chamber using a carrier gas such as Ar or He.

In all forms of ICP-MS, after the sample has been introduced to the ionization chamber a hot Ar^+ plasma (approximately 6,000 K) is used to ionize the sample. Because Ar has the fourth highest ionization potential on the periodic table, an Ar^+ plasma has enough energy to ionize every other element to the +1 charge state (*176*). The three elements which are not ionized to the +1 state are F, Ne, and He; these elements cannot be assayed by ICP-MS. In TIMS, sample introduction and ionization occur in the same step. The liquid sample is deposited onto a thin filament (typically Re or W) and placed into the instrument. The filament is heated up to 2,500 K until the sample beings to evaporate ions from the sample material (*176*).

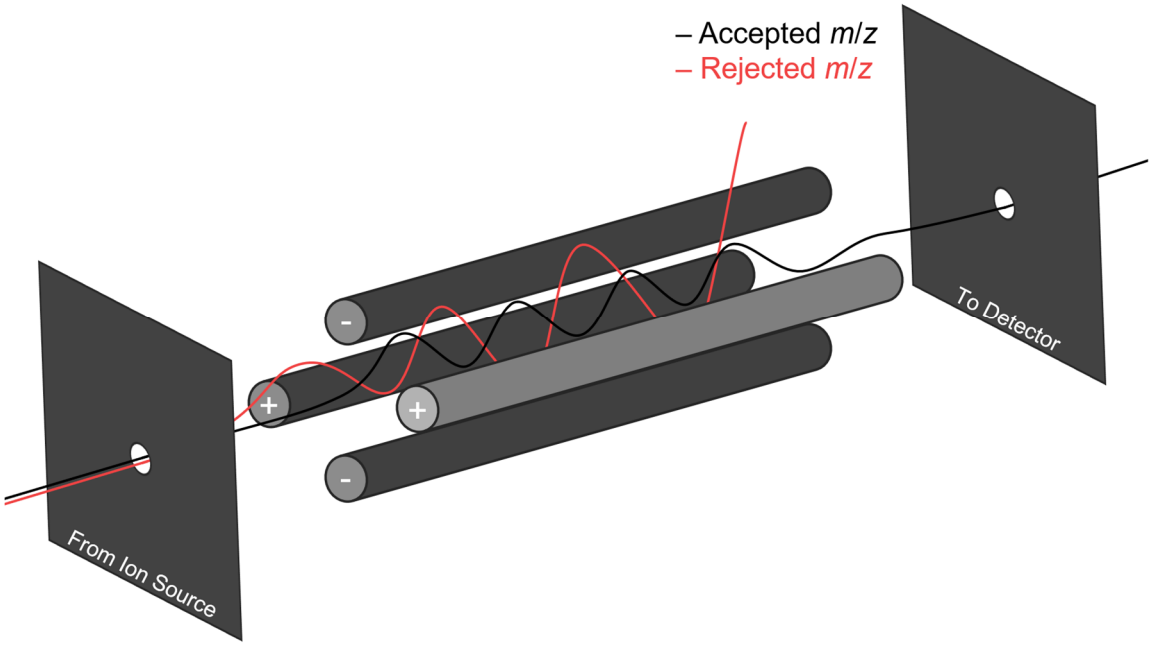

Figure 1.17. Quadrupole Mass Analyzer. These four electrodes are used to select for a single m/z in some ICP-MS and TIMS instruments. All four electrodes are biased with both direct and alternating currents that affect the trajectory of the ions within them. Only one m/z is allowed through the analyzer at a time; selected mass bins are scanned one at a time.

ICP-MS and TIMS use either quadrupole electrodes or dipole magnets as the mass analyzer. In some disciplines, a dipole magnet is more often referred to as a "magnetic sector." The mass analyzer is used to allow ions of a specific mass-to-charge ratio (m/z) to pass through while blocking all other ions. Because the instruments are designed to produce primarily 1+ ions, the mass-to-charge ratio of an ion is often discussed in terms of its mass or "mass bin." A quadrupole mass analyzer uses four electrodes to accept ions by their m/z, shown in Figure 1.17. Ion trajectories pass through the center of the quadrupole mass analyzer where parallel electrodes are biased to either a positive or negative direct current (DC) terminal. In

addition, each pair of parallel electrodes is biased with an alternating current (AC) that is 180° out of phase from the other pair. Heavy ions are most strongly affected by the constant direct current, while lighter ions are more strongly affected by the rapid alternating current (*176*). Combined, the electric fields produced from these currents are able to select for a single m/z. These quadrupole systems are cheap, widely deployed, low resolution mass analyzers.

Higher-resolution magnetic sector mass analyzers are available at higher costs. Their two poles exert a magnetic field perpendicular to the trajectory of the ion bean, applying a Lorentz Force. This force causes the ion beam to move with centripetal motion. These interactions are explained through Equations 1.34 and 1.35 where F_L is the Lorentz Force, F_C the force of centripetal motion, B the strength of the magnetic field, z the charge of the ion, v its velocity, m its mass, e the charge of an electron, and r the radius of its centripetal motion. The velocity of the ion beam is described by its kinetic energy (KE) in Equation 1.36 where V is the applied bias of an accelerating electrode. Because its centripetal motion originates solely from the Lorentz Force, Equations 1.34 and 1.35 can be set equal and re-solved (with Equation 1.36) to express the motion of a single m/z, shown in Equation 1.37. This equation reveals that a magnetic sector may select for a single m/z by varying B, V, or r. Practically, most magnetic sector mass spectrometers use B to select for ion mass (*177*). A diagram of these interactions is shown in Figure 1.18.

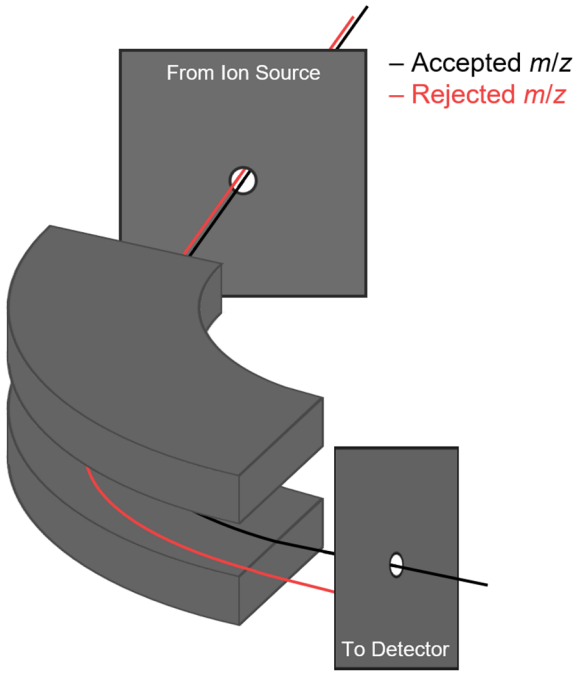

Figure 1.18. Dipole Mass Analyzer. These two electrodes select for a single m/z using a magnetic field and the resulting centripetal Lorentz Force. Ion beams passing between the two electrodes bend at a radius depending upon their m/z. In multi-collecting instruments, multiple m/z ion beams are accepted and directed towards multiple detectors.

$$F_L = Bzev \tag{1.34}$$

$$F_C = \frac{mv^2}{r} \tag{1.35}$$

$$KE = zeV = \frac{1}{2}mv^2 \tag{1.36}$$

$$\frac{m}{z} = \frac{B^2r^2e}{2V} \tag{1.37}$$

ICP-MS and TIMS use either Faraday cup or secondary electron multiplier (SEM) detectors. A Faraday cup is simply a conductive medium which produces a current as the ion beam implants into it, where the magnitude of the current is

proportional to the intensity of the ion beam. These detectors are effective for high beam intensities, which corresponds to samples with relatively high concentrations of analyte.

An SEM is a device which multiplies the signal from a single ion implantation event into millions of events. In an SEM, the ion beam strikes an electron-emissive material which ejects 1 – 3 electrons per incident ion. These electrons are accelerated towards a biased electron-emissive dynode, which also ejects electrons. This continues until the signal is multiplied by a factor of 10^6 – 10^8. These detectors are most effective for low intensity ion beams, or samples with a low concentration of analyte. Advanced detection is available through multi-collecting instruments (MC) such as MC-ICP-MS and MC-TIMS; these MC instruments use a magnetic sector mass analyzer to accept multiple m/z to multiple different detectors at the same time. These instruments are able to measure isotope ratios with incredibly high precision, producing relative errors as low as 0.1% (*178-180*).

Both ICP-MS and TIMS are highly sensitive analyses capable of detecting trace metals down to 1 part per trillion (ppt), where 1 ppt is 1 pg/mL of solution. Thus, these techniques are widely used to document trace metal content and sample isotopics in forensics (*15, 18, 19*). However, typical mass spectrometers do not have the resolving power to distinguish two isobars. Such "isobaric interference" should always be carefully considered when planning analysis by mass spectrometry. In some cases, chemical separation is required prior to mass spectrometry to prevent isobaric interference (*44*).

Some corrections should always be performed when using ICP-MS or TIMS. The most important corrections are mass bias and molecular interferences. Mass bias describes the fractionation that occurs in the ionization step due to the slightly different ionization potential of each isotope of an element. These effects are usually quite small, with less than a 1% change in ionization efficiency per amu. Mass bias corrections are performed by assaying a NIST traceable isotopic standard and comparing the measured isotopic ratios to its reported ratios. Molecular interference refers to isobaric interference which results from the formation of some "hot-atom" molecules within the energetic Ar^+ plasma. The most common molecular species formed in the plasma are argides, oxides, and hydrides. The formation of these interferences may be readily estimated by measuring a calibration standard which contains nuclides of $A-40$, $A-16$, and $A-1$, where A is the mass number of the analyte of interest.

The detection limit of a mass spectrometer is typically estimated by measuring blanks which contain acid without any sample analyte. The lower limit of detection (LOD or LLD) is most often quantified by measuring a blank several times and adding three standard deviations to the blank mean. The LLD refers to the lowest concentration of an analyte that may be positively identified as above background. Typically, the measurement errors on samples at the LLD are quite high, thus the lower limit of quantification (LLQ) is set at ten standard deviations above the blank mean and refers to the lowest concentration of an analyte that may be quantified with acceptably low error (*44*).

1.3.2 Chronometry

Chronometry is a form of temporal analysis which uses the Bateman Equations (Equations 1.21 and 1.22) to solve for the decay time a sample must have experienced based on a measured nuclide ratio from species within a decay chain. More often, chronometry is applied between two neighboring radionuclides in a decay chain (N_1 and N_2) , which enables the use of the simpler decay kinetics from Equations 1.15 and 1.19. While it initially looks like Equation 1.19 may be solved for time (t) on its own if both $A_2(t)$ and $A_1(0)$ are known, there actually does not exist an analytical solution to the equation. Instead, an analytical solution becomes apparent if Equation 1.19 is divided by Equation 1.15 (shown in Equation 1.38), which is solved for t in Equation 1.39. This result is why chronometry is usually discussed in terms of nuclide ratios. All variables here are defined per Section 1.1.2.

$$\frac{A_2(t)}{A_1(t)} = \frac{\lambda_2}{\lambda_2 - \lambda_1}\left(1 - e^{t(\lambda_1 - \lambda_2)}\right) \tag{1.38}$$

$$t = \frac{1}{\lambda_1 - \lambda_2} \ln\left[1 - \frac{A_2(t)}{A_1(t)}\frac{\lambda_2 - \lambda_1}{\lambda_2}\right] \tag{1.39}$$

The solution presented here assumes that $N_2(0) = 0$, and therefore chronometry is used to solve for the "time of last chemical separation." Typical applications of chronometry in nuclear forensics assume that the sample was completely purified of N_2 at $t = 0$; if that assumption is not true, then multiple chronometers from different decay chains will predict different sample ages.

Chronometry is not applicable to nuclides which are in secular equilibrium within a decay chain. Secular equilibrium describes a situation in which $\lambda_1 \ll \lambda_2$. In

these cases, $A_2(t)$ will always approach $A_1(t)$ after approximately seven half-lives of the daughter. This can be understood by the nature of N_2 decaying much faster than N_1; $A_2(t)$ is therefore limited by $A_1(t)$ and will eventually approach it (*98*). These effects are shown in Figures 1.19 and 1.20 using the ^{238}U – ^{234}Th decay pair as an example. If $\lambda_2 \ll \lambda_3$, the next nuclide in the decay chain may also exist in secular equilibrium with N_1, and so on for λ_n. In cases where N_1 and N_2 are in secular equilibrium, $A_2(t)/A_1(t)$ stops changing over time, rendering it useless for chronometry; however, if the time required to establish secular equilibrium is short compared to the time since last separation, $A_{n+1}(t)/A_1(t)$ may be used as a chronometer instead, where N_n is the final nuclide in secular equilibrium with N_1. This is performed routinely for some chronometers (*181*).

There are multiple decay chains of interest to chronometry depending upon the sample's nature. Most samples of U and Pu will contain measurable amounts of ^{234,235,238}U and ^{238,239,240,241}Pu, respectively. Some of these radionuclides have an immediate decay daughter which may be readily measured; others have decay daughters in secular equilibrium that cannot be used for chronometry, or a decay daughter which cannot be measured easily. Figure 1.21 shows the chronometers most often used for each radionuclide in U and Pu forensics (*27, 30-36, 38, 40, 181, 182*).

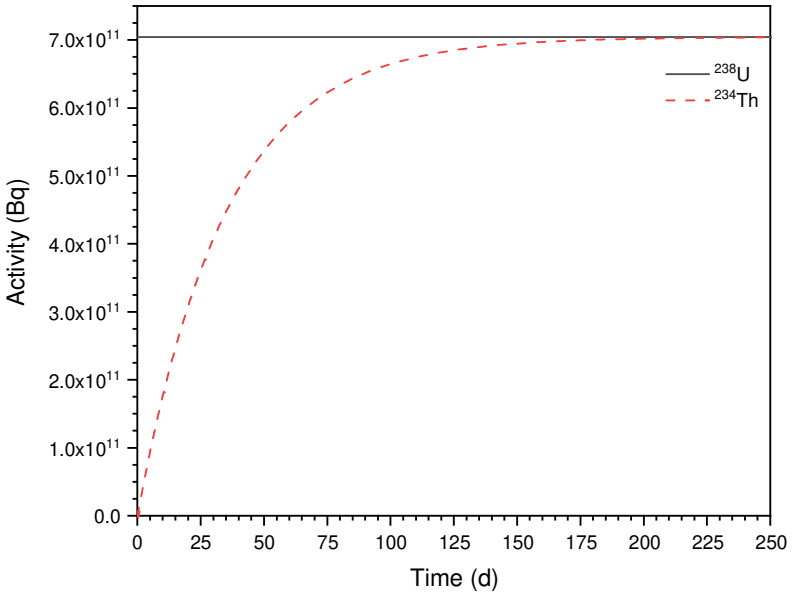

Figure 1.19. ^{238}U and ^{234}Th in Secular Equilibrium. This case is an example where $\lambda_1 \ll \lambda_2$; the activity of the long-lived ^{238}U nucleus ($t_{1/2}$ = 4.5x10^9 y) does not change appreciably over the short time domain, while the activity of the ^{234}Th daughter ($t_{1/2}$ = 24 d) quickly approaches $A_1(t)$. This occurs because the ^{234}Th nuclei decay rapidly relative to the decay of ^{238}U. One kilogram of ^{238}U was used for this example.

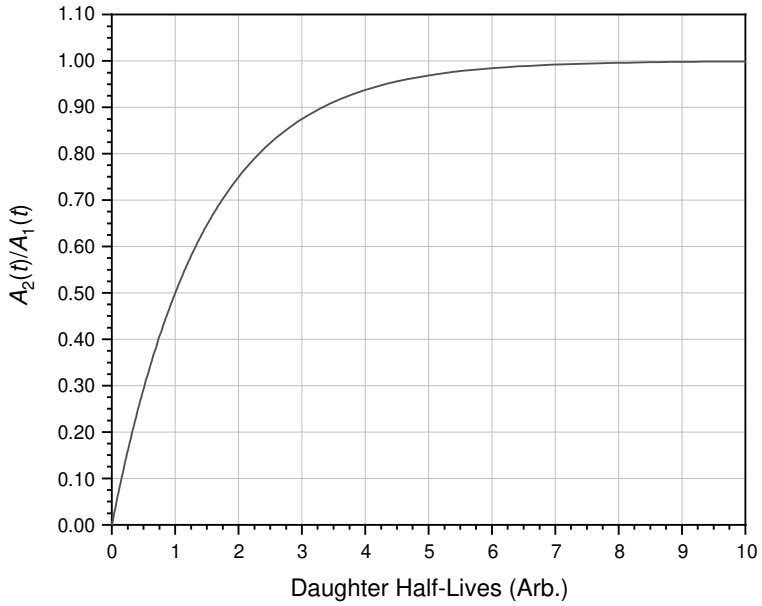

Figure 1.20. Approaching Secular Equilibrium. The rate at which two radionuclides approach secular equilibrium when $\lambda_1 \ll \lambda_2$. The activity ratio approaches one (and remains constant) after approximately seven half-lives of the daughter nuclide. Produced using the data from Figure 1.19.

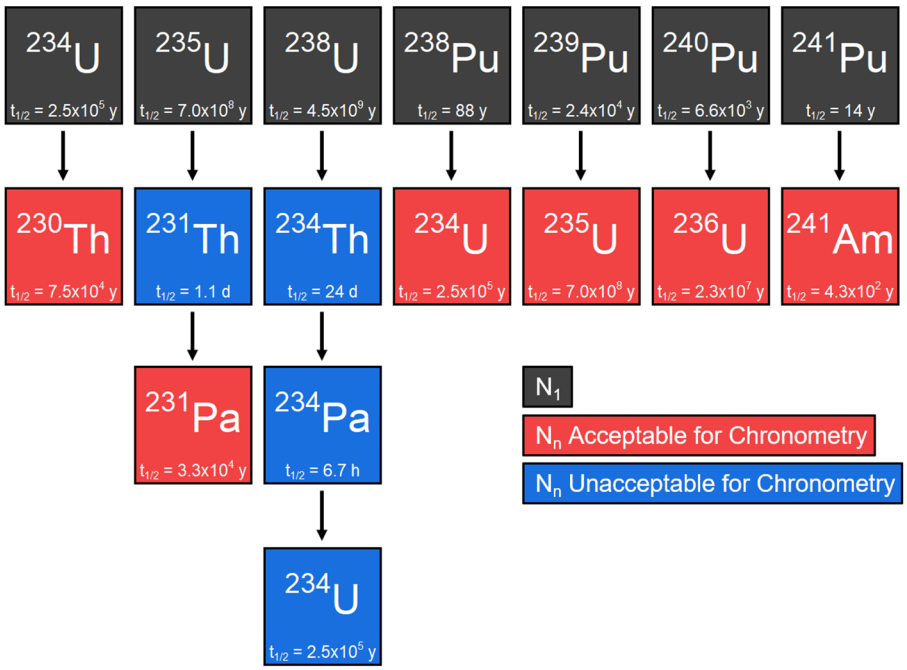

Figure 1.21. Chronometers for U and Pu Forensics. The chronometer pairs most frequently used for U and Pu forensics. Some of the radionuclides in this list cannot be used as a chronometer because they establish secular equilibrium with N_1 over a short period of time. ^{238}U has no usable chronometer because the first radionuclide which is not in secular equilibrium (^{234}U) should already be present in the bulk material even after chemical separation.

Chronometers may be measured using mass spectrometry, radiation detection, or a combination of the two. Typically, the smallest relative errors are produced using isotope dilution mass spectrometry (IDMS) with an MC-ICP-MS. IDMS describes an analytical procedure where well-characterized radiotracers (N_R) are added to the sample, which is then assayed by mass spectrometry. The radiotracers should be isotopes of N_1 and N_n (added and measured separately) such that the MC-ICP-MS may measure an isotope ratio of N_1/N_{R_1} and N_n/N_{R_n}, which is then multiplied by the known quantity of N_R which was added. When using well-

characterized radiotracers, IDMS is capable of measuring chronometers to less than 1% relative uncertainty (*26*).

The uncertainty in chronometric age (often referred to as a "model age") is most often reported in terms of the 95% confidence interval (*CI*). The confidence interval is determined using Equation 1.40 where t is Student's t, α is the significance level ($1 - CI$), N is the number of measurements, and σ is the standard deviation of the measured data (*183*).

$$CI = t_{\alpha,N-1}\frac{\sigma}{\sqrt{N}} \tag{1.40}$$

Student's t is available from a table based on the desired significance level and the number of measurements taken; it represents the coverage factor of the *CI* based on these parameters. When $N \geq 30$, Student's t begins to approach the same coverage factor which is used to describe a Gaussian distribution. For example, when $N \geq 30$, $t \approx 1$ for a *CI* of 68%, $t \approx 2$ for a *CI* of 95%, and $t \approx 3$ for a *CI* of 99.9%. The confidence interval is inversely proportional to $\sqrt{N}$; in general, taking multiple measurements will reduce the range of the *CI* even if the centroid of the measured value is wrong. When $N \geq 4$, the range of the 95% *CI* is typically smaller than the range of 2σ.

1.3.3 Isotopic and Radiopurity Evaluations

Isotopic and radiopurity evaluations are among the first steps of most forensic investigations (*9, 10, 19, 20, 55, 60, 61*). The radiopurity evaluation of an unknown sample begins with a non-destructive assay (NDA), using gamma and/or neutron spectrometry. The sample may be placed at an appropriate distance from a

high-purity Ge spectrometer (HPGe) and assayed for gamma-active radionuclides. This is effective as an NDA since it requires no sample preparation or dissolution. It can even be performed if the sample is encased in a thin layer of low Z material, as γ-rays are penetrating forms of radiation. The NDA may not be quantitative if the geometry of the sample is abnormal. However, it serves as a qualitative tool to understand what radionuclides the sample contains.

Figure 1.22 shows the gamma spectrum for the NDA of a sample of irradiated UO_2. The material was placed 3 m away from the detector face with a fractional dead time (τ/t) of 64%. These conditions are highly unfavorable for a quantitative NDA but were necessary due to the high activity of the sample. Even in these conditions, it was readily determined that the sample was relatively young irradiated U which likely contained weapons-grade Pu. These conclusions were possible because the dominant photopeaks were attributed to short-lived FPs, and a ^{137}Cs burnup measurement (661.7 keV on the γ spectrum) predicted a burnup of less than 1 GWd/MTU (gigawatt day per metric ton of U). Once the sample was dissolved and counted under more appropriate conditions, the burnup was confirmed as approximately 1 GWd/MTU.

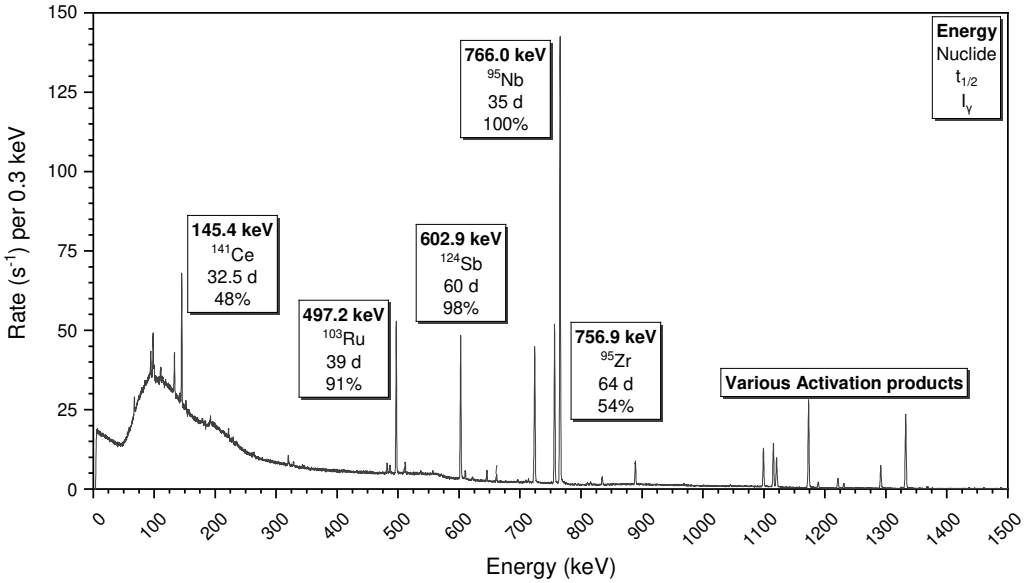

Figure 1.22. Non-Destructive Assay of Irradiated UO_2. Gamma spectrum taken as part of an NDA of irradiated UO_2 under non-ideal conditions. The sample was placed 3 m away from the detector face with a fractional dead time of 64%. Qualitatively, the presence of short-lived FPs indicates the sample was young, and a burnup measurement under these unideal conditions indicated the sample may contain weapons-grade Pu. ^{137}Cs (662 keV) is used to measure burnup.

Burnup is a property of irradiated material that describes how much energy was extracted per mass of fissile material in the fuel. In general, irradiated U will contain weapons-grade Pu if it was burned to less than 3 GWd/MTU (*17*). Weapons-grade Pu refers to Pu which is isotopically greater than 93% ^{239}Pu. This quality of Pu is particularly important because it is the lowest quality of Pu that may be readily deployed in a high-yield nuclear weapon (*15, 18, 19*).

A burnup measurement is performed by assaying the FP content of an irradiated sample. For example, the cumulative fission yield of ^{137}Cs is well known, at approximately 6% (*104*), and the energy released per fission is well documented

as approximately 200 MeV (*16*). The β-decay parents of ^{137}Cs are short lived, making it an ideal nuclide for burnup assay as it quickly approaches its cumulative yield. With those two pieces of information, the measured number of ^{137}Cs atoms may be used to determine the total number of fissions, and therefore the total amount of energy released from fission, which is then divided by the mass of U present to determine burnup.

An NDA may reveal other information about an unknown sample as well. ^{235}U is identified on a γ spectrum by its 185 keV photopeak, and ^{238}U by the 1001 keV photopeak of its secular equilibrium ^{234m}Pa daughter. These two photopeaks may be used in an NDA to determine the enrichment of U material. In addition, the identification of ^{241}Am (59 keV) may indicate the presence of ^{241}Pu, which produces ^{241}Am through β- decay. Following the NDA, destructive analyses are usually taken which involve dissolving the unknown sample. After dissolution, α spectrometry and ICP-MS may be performed to identify other radioactive actinides of interest to forensics. These results may be used in the chronometry, reactor discrimination, and trace metal analysis of the sample.

1.3.4 Reactor Discrimination

Per Section 1.1.4, the distribution of FPs produced during the fission of SNM in a nuclear reactor depends upon the conditions under which the material was irradiated. Fission by thermal neutrons produces the most asymmetric FPs, while fission by fast neutrons produces less asymmetric FPs (*104*). Fast neutrons are also captured by the various FPs and actinides less frequently than thermal neutrons due

to their smaller de Broglie wavelength; this results in drastically different isotope ratios such as $^{149}Sm/^{150}Sm$ in fuels discharged from fast and thermal neutron nuclear reactors (*16, 51, 53, 54*). The fissioning nucleus also impacts the distribution of FPs – the fission of ^{235}U will produce different FPs than the fission of ^{239}Pu (*104*). In addition, the initial content of $^{235,238}U$ and $^{239,240}Pu$ in the fuel will impact the production of the actinides produced through neutron capture. All of these factors come together to produce unique "fingerprints" which may be used to identify the irradiation conditions of an unknown sample. Some of the irradiation conditions which may be identified by measuring the FP and actinide distributions of unknown material include its U enrichment, fuel composition, reactor type, neutron spectrum, fuel burnup at discharge, and "cooling time" (time since the material was removed from the reactor) (*12, 16, 17, 44, 51-56, 58, 60-62*).

Some of these properties may be identified by comparing the measured Pu isotope ratios in an unknown sample to several sets of Pu isotope ratios produced from the simulation of multiple reactor conditions (*55, 56, 58*). Figure 1.23 plots three different Pu isotope ratios on three axes as a function of fuel burnup to produce clear separation between fuels discharged from pressurized water reactors (PWR) and boiling water reactors (BWR) (*58*). As these two types of nuclear reactors are similar in fuel composition and neutron spectrum, distinguishing between them is a significant result; however, it should be noted that 10% error in some of the measured quantities may result in overlapping of the two curves.

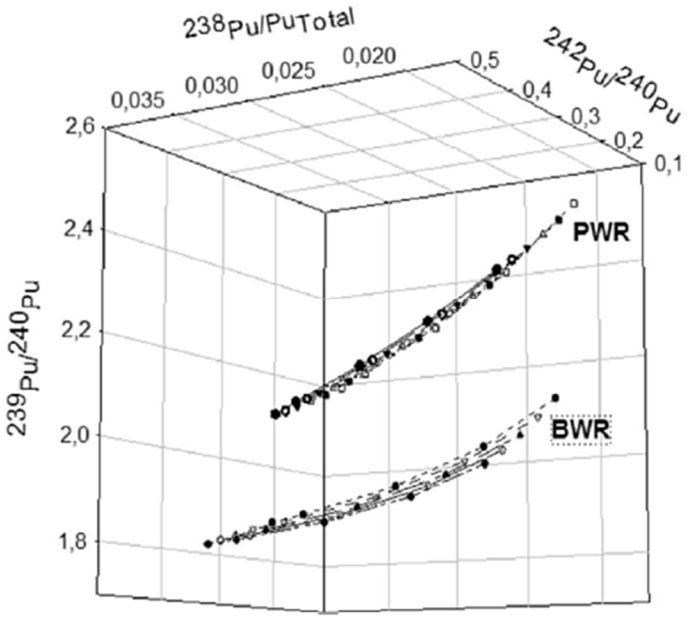

Figure 1.23. Pu Isotope Fingerprinting. Three different Pu isotope ratios are plotted as a function of fuel burnup to produce separation between two different similar nuclear reactors. Ideally, one could measure the Pu isotope ratios of an unknown sample and determine if it was discharged from a pressurized water reactor (PWR) or boiling water reactor (BWR) based on where it falls on this figure. Presented with permission from (58).

Figure 1.24 shows some spatial resolution between multiple reactor types as a function of fuel burnup for two Pu isotope ratios, but most of these curves tend to overlap at low fuel burnups (*55*). Using Pu isotope ratios exclusively tends to be an effective tool for reactor discrimination when there exists some prior knowledge about the sample's history. For example, if it is known that the sample did not originate from a graphite moderated reactor, some of the curves from Figure 1.24 could be excluded. However, if the sample history is entirely unknown, Pu isotope ratios alone are often not sufficient for reactor discrimination.

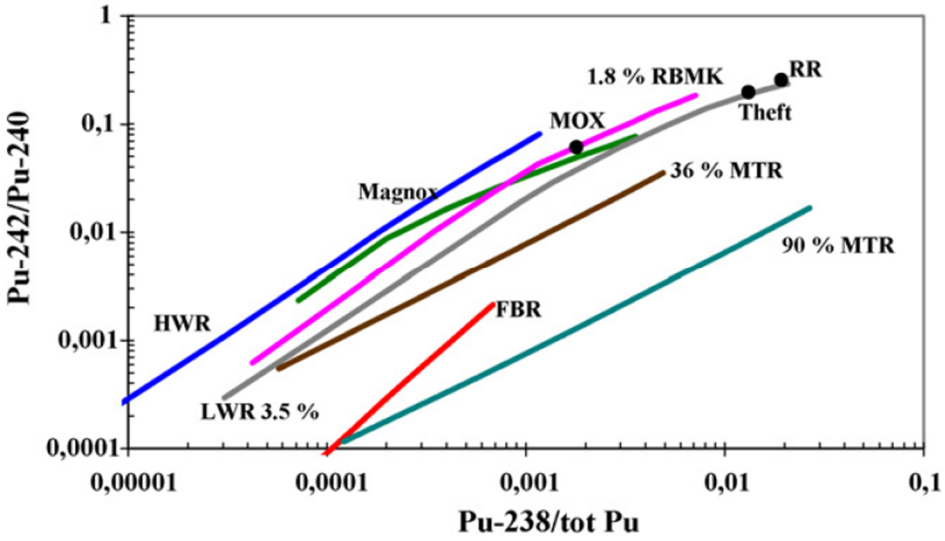

Figure 1.24. Reactor-Type Discrimination of Separated Pu. Multiple nuclear reactors were modeled and their Pu isotopics reported as a function of fuel burnup. Three samples of separated Pu were compared to the models to determine their reactor origin (black circles). Many of these curves are indistinguishable from one another at low fuel burnups (towards the origin of the plot). Presented with permission from (55).

A maximum likelihood forensic methodology has recently been developed at Texas A&M University which utilizes both Pu and FP isotope ratios to discriminate the irradiation history of unknown irradiated SNM (*44, 52-54*). The methodology compares a set of measured isotope ratios to a suite of simulated isotope ratios produced under varying irradiation conditions and reactor types by the Monte Carlo radiation transport code, MCNP6 (*184*). The ideal isotope ratios chosen for this methodology are $^{137}Cs/^{133}Cs$, $^{134}Cs/^{137}Cs$, $^{135}Cs/^{137}Cs$, $^{136}Ba/^{138}Ba$, $^{154}Eu/^{153}Eu$, $^{150}Sm/^{149}Sm$, $^{152}Sm/^{149}Sm$, $^{240}Pu/^{239}Pu$, $^{241}Pu/^{239}Pu$, and $^{242}Pu/^{239}Pu$. The isotope ratios were chosen such that each of them change as a function of fuel burnup, reactor type, or cooling time (*54*). In addition, an isotope ratio was only accepted if it

could be readily measured by γ spectrometry or mass spectrometry in materials greater than 10 years old.

The measured (*meas*) and simulated (*sim*) isotope ratios are compared to each other based on their Gaussian similarity using Equation 1.41, where $L(M|r)$ is the likelihood that the reactor model M matches the measured isotope ratios r, σ is the uncertainty of a measurement, and j refers to one specific isotope ratio.

$$L(M \mid r) \propto \prod_{j=1}^{n} \frac{1}{\sigma_j \sqrt{2\pi}} e^{-\frac{\left(r_{j,meas} - r_{j,sim}\right)^2}{2\sigma_j^2}} \tag{1.41}$$

To determine the irradiation conditions of unknown materials, the methodology computes the likelihood of each reactor model under different burnups and cooling times, then the "maximum likelihood" which was calculated for the model is presented with its corresponding parameters.

This forensic methodology was first applied in a publication which compared the isotope ratios of two simulated fuels to the models of some reactor types produced by the authors (*54*). The first fuel was simulated as natural UO_2 ($^{nat}UO_2$) originating form the core of the University of Missouri Research Reactor (MURR) discharged at a burnup of 4.39 GWd/MTU with a cooling time of 10 years. The second fuel was simulated as depleted UO_2 ($^{dep}UO_2$) originating from the core of the Fast Flux Test Facility (FFTF) discharged at a burnup of 1.97 GWd/MTU with no cooling time. The simulated isotopics of these materials were compared against the simulated isotopics of fuels discharged from generic pressurized water reactors (PWR), pressurized heavy water reactors (PHWR), and fast-breeder reactors (FBR) using

the likelihood calculation in Equation 1.41, shown in Tables 1.01 and 1.02 (*54*). In these tables, the likelihood values are reported as the natural logarithm of the likelihood with the corresponding burnup and cooling time of their maximum likelihood.

The reactor model which was most similar to the simulated $^{nat}UO_2$ fuel was the PHWR by a considerably large margin. This is a fair result as the PHWR was the only type of reactor in the model library that used natural UO_2 fuel. The model predicted a burnup and cooling time which were similar to the known burnup of the simulated fuel. The differences likely result from the differences between the actual MURR facility and a typical PHWR.

The reactor model which was most similar to the simulated $^{dep}UO_2$ fuel was the FBR. This is a fair result as the FBR is the only type of reactor in the model library which has a predominately fast neutron spectrum. The fuel burnup and cooling time of the model did not correctly predict the known burnup and cooling time of the simulated fuel, likely resulting from differences between the actual FFTF facility and a typical FBR.

Table 1.01. Maximum Likelihood Analysis of the Simulated $^{nat}UO_2$ Fuel. Presented with permission from (54).

Reactor Model	Maximum ln Likelihood	Fuel Burnup (GWd/MTU)	Cooling Time (y)
PWR	-1.0×10^3	≥ 4.74	8.9
PHWR	+28	3.83	10.6
FBR	-2.6×10^6	≥ 4.73	0

Table 1.02. Maximum Likelihood Analysis of the Simulated $^{dep}UO_2$ Fuel. Presented with permission from (54).

Reactor Model	Maximum ln Likelihood	Fuel Burnup (GWd/MTU)	Cooling Time (y)
PWR	-4.7×10^2	≥ 4.74	6.2
PHWR	-1.1×10^3	4.35	8.5
FBR	+42	0.43	1.1

While these initial results were encouraging, it must be noted that simulated fuels were compared against simulated reactor models. To fully verify the strength of the maximum likelihood forensic approach, it would be necessary to apply it to real irradiated U, and then to Pu which has been separated by the PUREX process. Applying the methodology to such materials forms the basis of Chapters II and III of this dissertation.

1.3.5 Trace Metal Analysis

It is common in a forensic investigation of SNM to assay the trace metal content of the unknown material (*8-10, 12, 14, 15, 19, 20*). While the trace metal content does not hold a wealth of information, it is typically used to check for consistency between identified metal impurities and documented metal impurities of declared materials. For example, a sample of Pu which is suspected to have been separated in late 1940 or early 1950 should contain some amount of trace Bi, La, and Ce resulting from contamination through the Bismuth Phosphate purification process (*12*); otherwise, it may contain some amount of Fe resulting from the Fe^{II} reduction step of the PUREX process (*185, 186*). Some facilities which produce SNM may have documented trace metal impurities in their product, which should also be seen in the assay of any SNM which is suspected to originate from that facility.

The techniques which are most often used for trace metal assay are ICP-MS, XRF, and electron dispersive x-ray spectrometry (EDS). While the mass of the trace metal content is sometimes quantified during analysis, no publication to date has used the quantified masses for any additional forensic discrimination. In practice, qualitative identification of the trace metals present has been the only applied use.

The following chapters utilize all of the preceding fundamental science, instrumental analysis, reactor physics, and statistical evaluations discussed here to study several samples of SNM in detail. It is noted that a strong understanding of these fundamental principles is required to perform the detailed analyses reported herein.

CHAPTER II

[1]FORENSIC CHARACTERIZATIONS OF IRRADIATED UO_2 CONTAINING FUEL-GRADE AND WEAPONS-GRADE PLUTONIUM

A nuclear forensic collaboration between the Department of Nuclear Engineering, Center for Nuclear Security Science & Policy Initiatives, Cyclotron Institute, and Chemistry Department at Texas A&M University has made significant progress in the development of a novel forensic methodology in recent years (*44, 52-54*). This methodology was discussed in detail in Section 1.3.4. In brief, it is designed to compare a set of measured isotope ratios in irradiated U or separated Pu to a suite of simulated isotope ratios from a large range of reactor types and irradiation conditions; the similarities between the measured and simulated ratios are computed using Equation 1.41. Each considered reactor type is modeled at a range of burnups and cooling times, and the "maximum likelihood" of each reactor is reported as the closest match between the simulated and measured isotope ratios for each reactor type. Prior to this work, the methodology had been successfully applied to simulated irradiated fuels, but needed to be validated with real irradiated SNM (*54*). The following work provides a validation of the methodology.

[1] Parts of this chapter have been previously published by Glennon *et al*. [*44*]. Appropriate permission to reproduce the work here has been obtained from the publishing journal.

2.1 Description of the Irradiated UO_2

To validate the methodology, two samples of UO_2 were prepared and irradiated at two different facilities under different conditions to produce material containing weapons-grade Pu. The details in this section represent a summary of work performed by the whole of the forensics collaboration. It was chosen to irradiate $^{dep}UO_2$ in a fast spectrum of neutrons in order to represent fuel discharged from the blanket of an FBR, and $^{nat}UO_2$ irradiated in a thermal spectrum of neutrons in order to represent fuel discharged from the core of a PHWR. Both of these reactor types have been known to operate in India, which is not under direct IAEA safeguards through the NPT (*53*). Both fuels were intended to be burned to a total fuel burnup of 1 GWd/MTU in order to produce weapons-grade Pu.

2.1.1 Irradiation of $^{dep}UO_2$ at the High Flux Isotope Reactor

The first fuel sample was prepared as six pellets of $^{dep}UO_2$ (approximately 16 mg each) encapsulated in a ^{nat}Gd "sheath" for irradiation in the High Flux Isotope Reactor (HFIR) at Oak Ridge National Laboratory. From this point on, this material is referred to as the "HFIR" material. For clarification, this term will refer to the six pellets which were prepared and irradiated at HFIR, it will not refer to any material discharged from the HFIR core. A schematic and radiograph of the HFIR material as prepared for irradiation is shown in Figure 2.01 (*17*). The position of the pellets as they were irradiated in the HFIR core's flux trap is shown in Figure 2.02 (*17*).

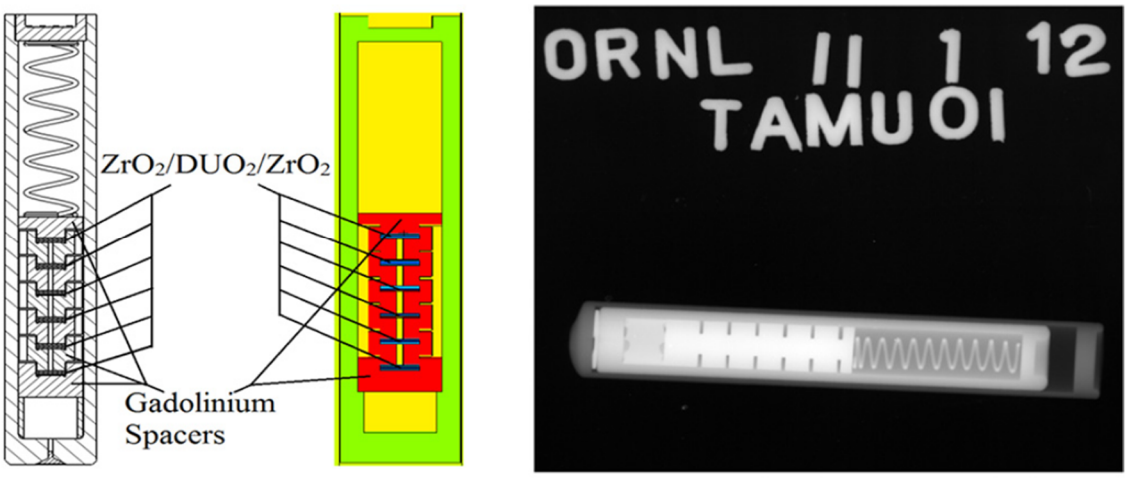

Figure 2.01. Schematic and Radiograph of the Irradiated $^{dep}UO_2$ Pellets. Schematic representation of the UO_2 pellet assembly designed for the irradiation of the $^{dep}UO_2$ at HFIR (left). The six original pellets were completely surrounded by ^{nat}Gd to block the thermal neutrons emanating from the HFIR core. Radiograph of the constructed assembly prior to irradiation (right). Presented with permission from (17).

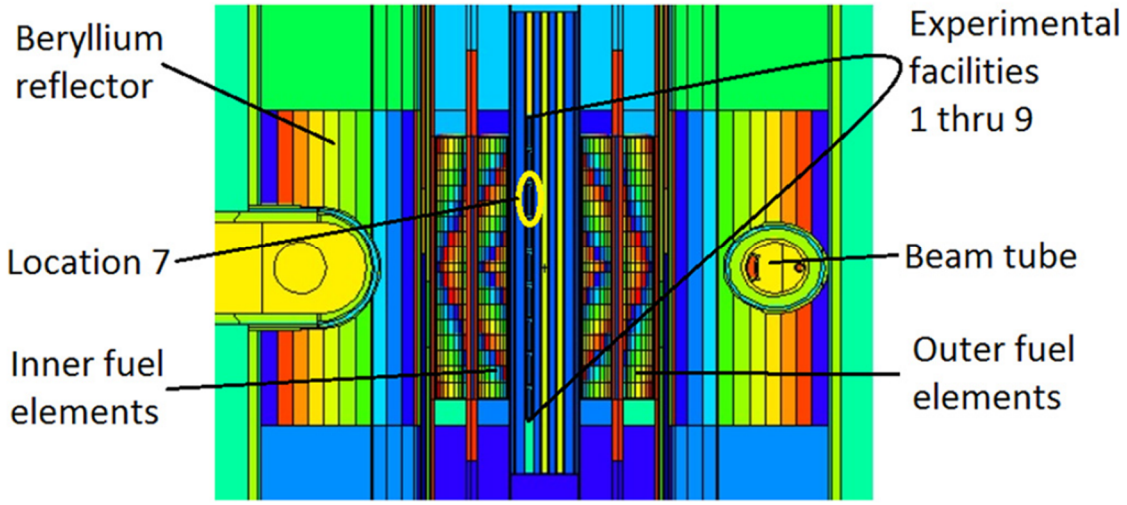

Figure 2.02. Model of the High Flux Isotope Reactor. Reactor model of HFIR as used to design the irradiation parameters. The $^{dep}UO_2$ pellets were located in the flux trap in the center of the reactor in location 7. Presented with permission from (17).

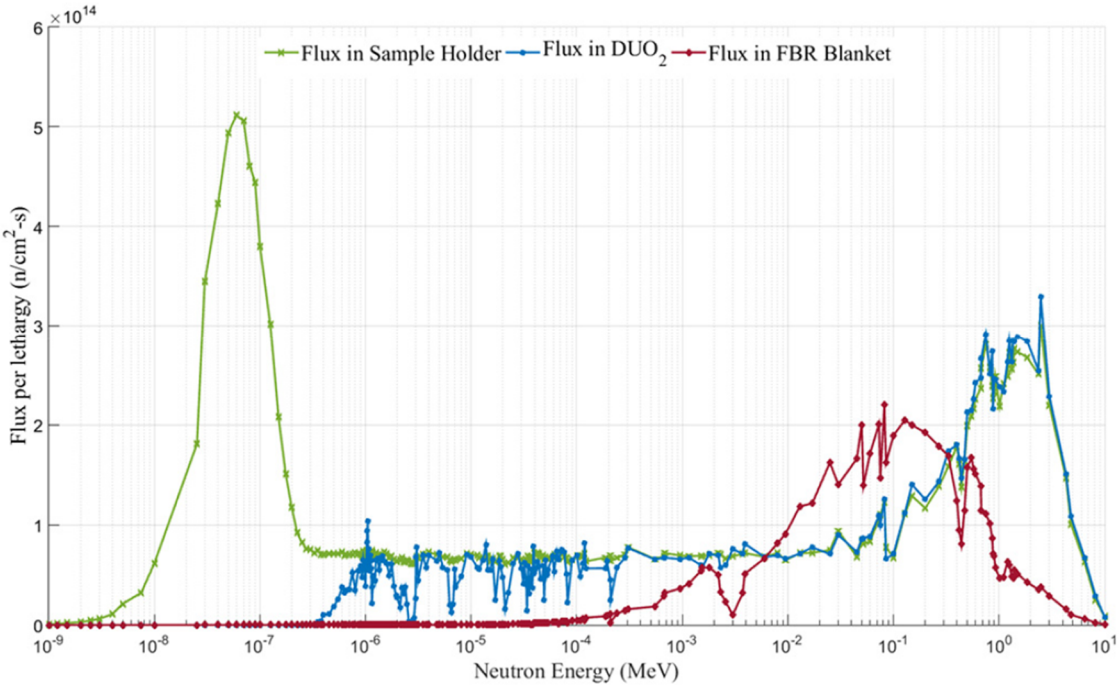

Figure 2.03. Flux Spectrum Exposed to the $^{dep}UO_2$ Pellets. Flux spectra comparisons between three irradiation conditions. The blue line indicates the net flux seen by the shielded $^{dep}UO_2$ pellets as depicted in Figure 2.01. The ^{nat}Gd sheath blocks the strong peak of thermal neutrons from the HFIR core. Presented with Permission from (17).

While HFIR is known as the highest flux of thermal neutrons in the US, it is not known for producing fast neutrons. In order to shield the HFIR pellets from the core's high flux of thermal neutrons, they were encapsulated in a ^{nat}Gd sheath as seen in Figure 2.01. Several isotopes of ^{nat}Gd have high thermal neutron capture cross sections, making it an ideal material to block thermal neutrons from reaching the $^{dep}UO_2$ pellets (*100*). The resulting flux spectrum is shown in Figure 2.03 as seen by the shielded $^{dep}UO_2$ pellets (*17*). Although the flux spectrum seen by the HFIR pellets is not identical to the flux spectrum seen in the blanket of an FBR, it does provide a close approximation of the desired system. These irradiation conditions were

necessary as there are currently no fast neutron reactors operating in the US (*187*). The HFIR material was irradiated from January 8th, 2013 until February 2nd, 2013 in axial position 7 of radial position C-5 in the reactor's flux trap. Irradiation resumed on May 7th, 2013 until final discharge on June 1st, 2013 (*17*). Evaluation of the irradiation is discussed in Section 2.3.1

2.1.2 Irradiation of $^{nat}UO_2$ at the University of Missouri Research Reactor

The second fuel sample was prepared as three pellets of $^{nat}UO_2$ (approximately 14 mg each) prepared separately in a single Al (alloy 1100) canister for irradiation in the University of Missouri Research Reactor (MURR). From this point on, this material will be referred to as the "MURR" material. The term MURR will not refer to any material discharged from the MURR core. A model of the reactor with the relative position of the $^{nat}UO_2$ pellets is shown in Figure 2.04 (*16*). These pellets were intended for irradiation in a thermal neutron environment, which is provided naturally by the chosen reactor; therefore, no materials were added to the pellets to change the neutron spectrum emanating from the core. The neutron spectrum of MURR is compared to three other similar nuclear reactors in Figure 2.05 (*16*).

The final discharge of the MURR material occurred on April 25, 2017 after a total irradiation period of 111.9 full-power days at a radial and axial distance of 27.9 cm and 36.2 cm away from the core center, respectively. The reactor was shut down at least once per week during the irradiation period, such that the 111.9 full-power days were distributed over 126.3 days and 33 total irradiation periods (*16*).

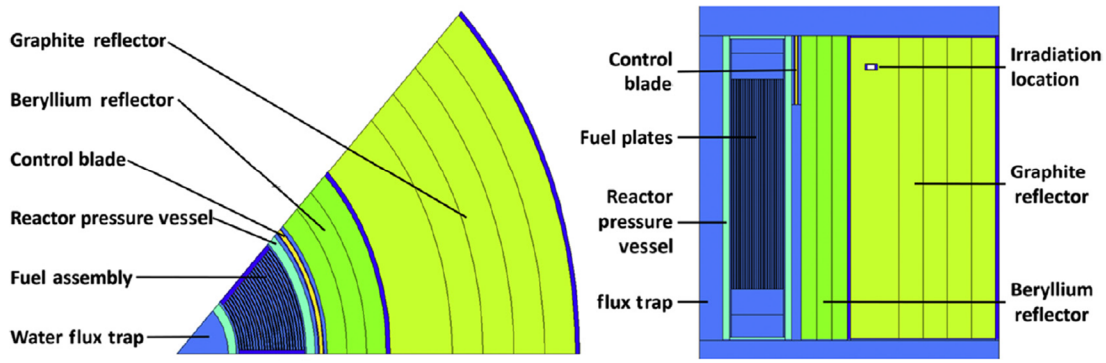

Figure 2.04. Model of the University of Missouri Research Reactor. Reactor model of MURR used to design the irradiation parameters. The core was modeled with symmetry based on the one-eighth section modeled here. The $^{nat}UO_2$ pellets are located in the graphite reflector outside of the reactor core. Presented from an open access publication (16).

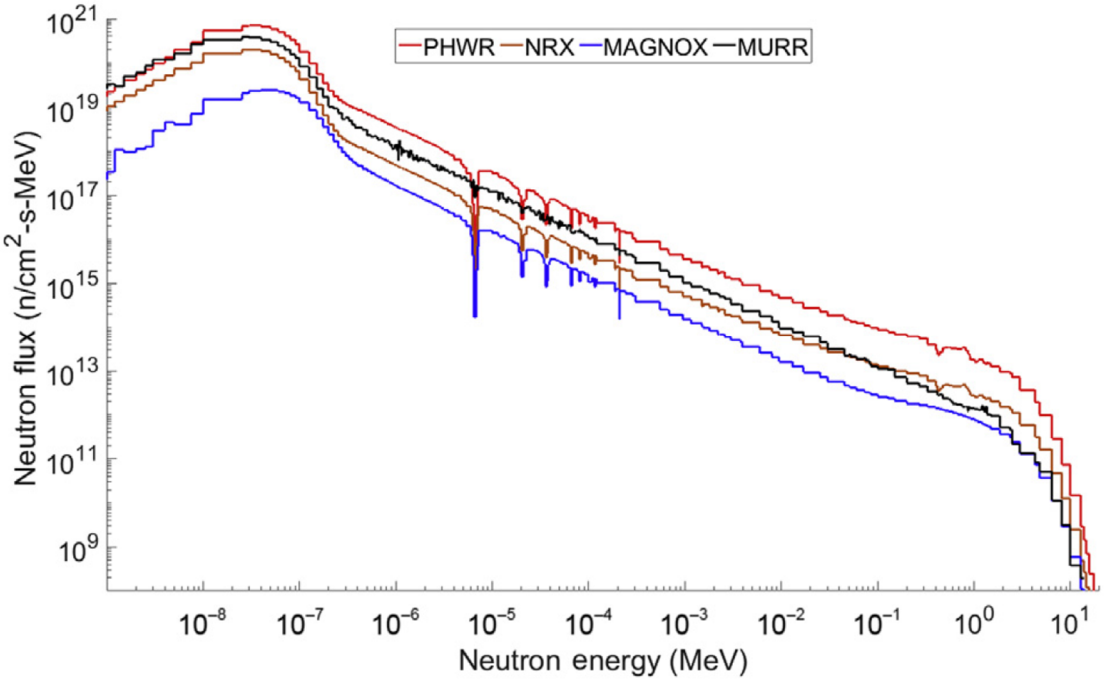

Figure 2.05. Flux Spectrum Exposed to the Irradiated $^{nat}UO_2$ Pellets. Simulated flux spectra comparisons between four reactor types. The black line represents the neutron spectrum seen by the $^{nat}UO_2$ pellets. The flux is generally similar to the known neutron spectra from operating thermal reactors around the world. Presented from an open access publication (16).

2.2 Experimental Methods

Both the HFIR and MURR pellets were characterized as reported here with and without a chemical separation to assay the isotope ratios of interest to the maximum likelihood forensic methodology (Section 1.3.4). While most isotope ratios of interest could be measured directly through a combination of mass spectrometry and γ spectrometry, the $^{150}Sm/^{149}Sm$ isotope ratio required a chemical separation prior to assay by ICP-MS. ^{150}Sm experiences isobaric interference in these irradiated materials from the presence of ^{150}Nd which is also produced as a FP. The chosen method to separate these elements prior to assay by ICP-MS was cation exchange column chromatography with α-HIB (Section 1.2.2).

2.2.1 Reagents

All nitric acid used was purchased as Omni-Trace Ultra Nitric Acid from MilliporeSigma with trace metal contaminates certified as ≤ 0.01 ppt for Nd, Sm, and Eu, and ≤ 0.05 ppt for Gd. The α-HIB used was purchased as 99% pure from Alfa Aesar and prepared as ammonium α-hydroxyisobutyrate using ≥ 99.5% pure NH_4Cl purchased from BDH Chemicals. The cation exchange resin was purchased as DOWEX 50W X4 200-400 mesh in the H^+ form from Alfa Aesar. UTEVA resin 2 mL cartridges were purchased with 50-100 μm resin beads from Eichrom.

Cs, Ce, Nd, Sm, Eu, Gd, and U calibration standards were used for ICP-MS calibration and surrogate column separations purchased individually as 1,000 ppm ICP-MS standards from BDH chemicals. A separate mixed rare earth element (REE) ICP-MS standard containing Sc, Y, La, Ce, Pr, Nd, Pm, Sm, Eu, Gd, Tb, Dy, Ho, Er, Tm,

Yb, Lu, Th, and U at 100 ppm each was purchased from Inorganic Ventures to check for potential systematic error in the ICP-MS calibration.

2.2.2 UO_2 Pellet Dissolutions

Two of the six HFIR pellets were received at Texas A&M University on August 31st, 2013 and allowed to cool for 8 months prior to dissolution in 5 mL of 4 M HNO_3. The dissolution of one pellet was carried out by previous staff (*17*) at approximately 50 °C in an enclosed system with a carbon filtered vacuum-trap cooled with liquid N_2. The vacuum pump was used to draw radioiodine, radioxenon, and radiocarbon out of the solution's headspace, along with the N_2O_4 and NO_2 produced during dissolution from the reduction of HNO_3.

All three MURR pellets were received at Texas A&M University on July 12, 2017 and allowed to cool for 3 months prior to dissolution in 5 mL of 8 M HNO_3. Dissolution of one pellet was carried out using an apparatus of the same design as the HFIR material. The dissolution apparatus is pictured in Figure 2.06.

2.2.3 Mass Spectrometry

Mass spectrometry was performed using a newly installed Thermo Fisher Scientific iCAP RQ mass spectrometer made available for use with radioactive materials in the College of Geosciences with aide from Professor Brent V. Miller. This mass spectrometer uses an Ar^+ plasma ion source, quadrupole mass analyzer, and SEM detector as discussed in Section 1.3.1. All isotope ratios and isotopic vectors measured by ICP-MS are reported as atom percent or as atom ratios.

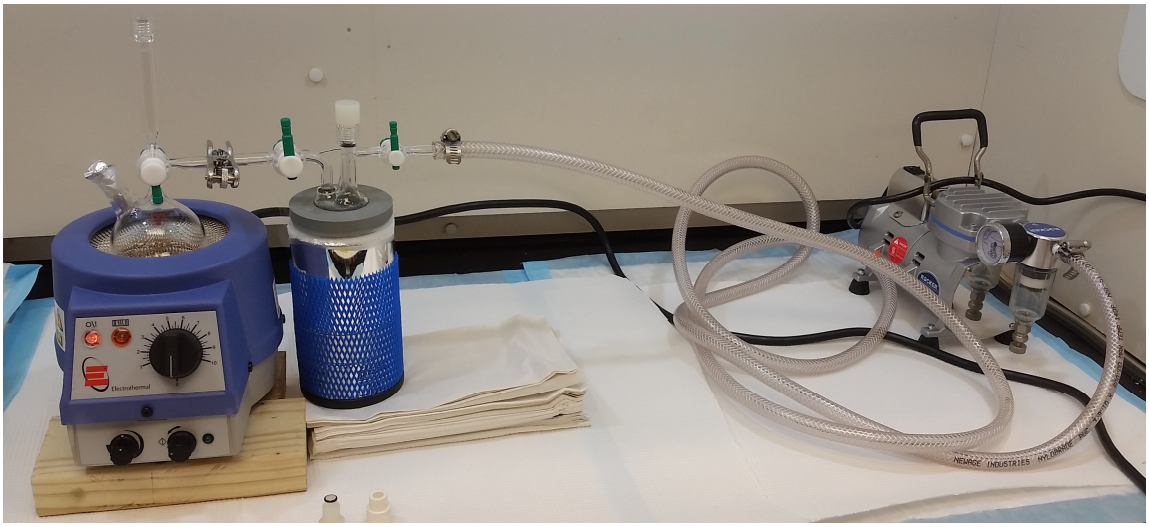

Figure 2.06. Dissolution Apparatus. Apparatus used to dissolve both the HFIR and MURR pellets. All glassware was replaced between the dissolution of each sample. An addition funnel was used to add acid without opening the system to air. This was done to avoid releasing radioiodine and radioxenon into the atmosphere.

Typical operating procedures for the instrument included replacing the standard sample cone, skimmer cone, torch, inlet, spray chamber, nebulizer, and sample tubing with ones specifically designated for use with radioactive material prior to operation. Tubing was disposed of and replaced between each use with radioactive materials, while the other components were swapped in and reused each time for the assay of any radioactive material. A vacuum trap was installed to prevent radioactive material from migrating to the vacuum pump's oil. Regularly scheduled maintenance and review by radiation safety personnel indicated no radioactive contamination was found on any component of the instrument aside from those previously mentioned. The majority of radioactive contamination was found on the inner skimmer cone after typical use.

All samples were diluted into 2% HNO_3 (v/v) prior to assay by ICP-MS. Typical calibration standards were prepared between 0.01 – 100 ppb containing each element of interest. The LLD was determined in every mass bin by adding three standard deviations to the blank mean. Likewise, the LLQ was determined using ten standard deviations. Assays employed both acid blanks and sample blanks as appropriate, where a sample blank is defined as any acid blank which was exposed to the same process as an actual sample (for example, elution through a column).

Mass bias and molecular interferences were corrected as appropriate using the guidelines discussed in Section 1.3.1. Mass bias corrections were performed using naturally abundant species for most elements on the periodic table while the U500 isotopic standard was used for U mass bias determination (*188*). $^{238}U^{1}H$ formation was the most significant molecular interference in most assays, adding isobaric interference to the ^{239}Pu mass region in unseparated samples. The rate of $^{238}U^{1}H$ formation was measured between 0.009 – 0.01% under most conditions as measured using calibration standards.

2.2.4 Gamma Spectrometry

Gamma spectra were taken at sample distances between 1.15 and 9.0 cm from the detector face of a Canberra Standard Electrode Coaxial high-purity germanium (HPGe) detector cooled with liquid nitrogen and shielded with lead. Energy and efficiency calibrations were performed using a ^{152}Eu NIST-traceable calibration standard purchased from Eckert and Ziegler. Energy and efficiency calibrations representative of typical operation are shown in Figures 2.07 and 2.08.

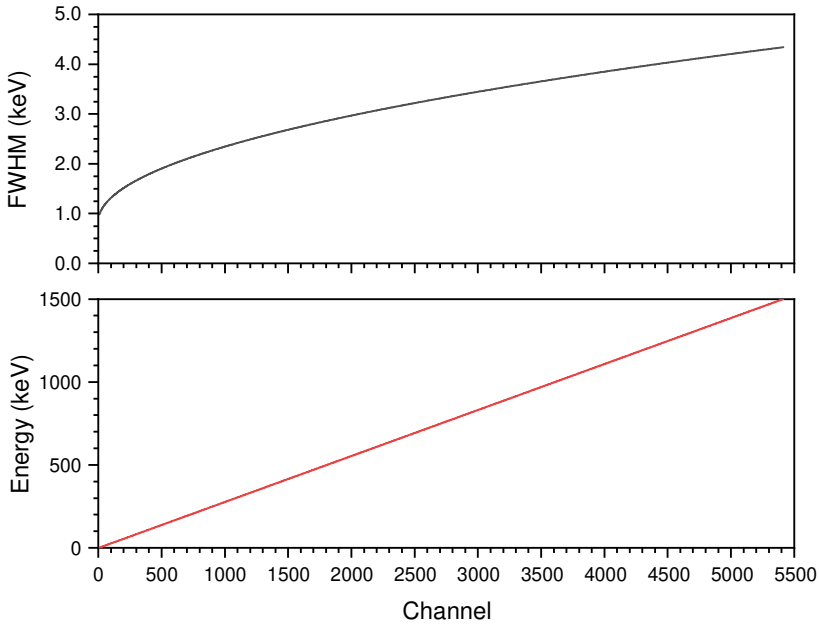

Figure 2.07. Energy Calibration of the Gamma Spectrometer. The HPGe detector was calibrated for energy (bottom) with a NIST-traceable ^{152}Eu source placed between 1.15 and 9.0 cm from the detector face. The FWHM is also reported as a function of channel (top).

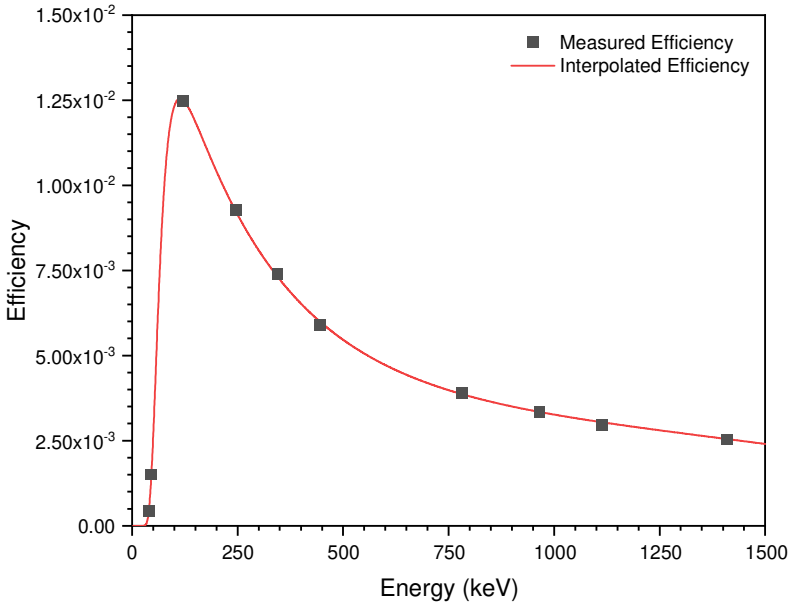

Figure 2.08. Efficiency Calibration of the Gamma Spectrometer. The HPGe detector was calibrated for efficiency with a NIST-traceable ^{152}Eu source placed 9.0 cm from the detector face. Generally, photopeaks with intensities below 1% were not accepted for calibration. The two left most points are x-rays from the ^{152}Sm decay daughter.

2.2.5 Column Chromatography

Chromatography was performed using benchtop columns with flow rate controlled by an eight-roller Ismatec REGLO Digital peristaltic pump. All columns were 300 mm by 3.12 mm height by inner diameter made of glass. The columns were slurry packed with DOWEX 50W X4 strong cation exchange stationary phase in the NH_4^+ form to a bed height of 210 mm at pH 3.00. The free column volume (FCV) of a typical column was measured as 33% (549 µL) by detecting the first drop at which the HFIR material eluted through the column. The HFIR material was considered to be diverse enough to contain anionic species for this determination.

The mobile phase for all chromatography separations was prepared as 0.40 M α-HIB at pH 3.00 and eluted at 0.50 mL/min. Fractions were collected at each FCV for chromatography of the HFIR and MURR pellets. Columns were stripped of any remaining lanthanide elements using several bed volumes of 0.5 M α-HIB at pH 4.2 then rinsed with 1 M NH_4Cl at pH 3.00 between each use.

2.2.6 Column Chromatography of Surrogate Material

Surrogate material was prepared to determine the performance of the separations before applying them to the HFIR and MURR pellets. The surrogate material contained 1.75 µg of Ce, Nd, Sm, Eu, Gd, and U, as prepared using ICP-MS standards of those elements. Columns were performed both at room temperature and at 60 °C to determine the effect of temperature on separation resolution (R_s). Temperature was maintained by pumping warm water through the jacketed region

of the glass column; the resin bed was heated at 60 °C for one hour to establish thermal equilibrium prior to separation. Fractions were collected every 0.5 FCVs.

2.2.6 Column Chromatography of the Irradiated UO_2 Materials

A 500 μL aliquot containing 2% of the dissolved HFIR pellet was diluted from 4 M HNO_3 to 0.4 M HNO_3 and loaded onto the cation exchange column inside a contained glovebox. The material was separated as previously discussed with fractions collected every FCV. Both the HFIR and MURR pellets were separated at room temperature.

A 500 μL aliquot containing 6% of the dissolved MURR pellet was diluted and loaded onto the cation exchange column in the same way. A separate 500 μL aliquot containing 20% of the dissolved MURR pellet was diluted to 4 M HNO_3 and eluted through a 2 mL UTEVA resin cartridge using a 4 M HNO_3 mobile phase to sequester the U.

The UTEVA cartridge was rinsed with several bed volumes of 4 M HNO_3 prior to use. The lanthanide fraction was collected in 1.72 mL. The mobile phase was changed to 0.02 M HNO_3 and the U fraction was collected in the next 3.00 mL. The resulting lanthanide fraction was diluted to 0.4 M HNO_3 and loaded onto the cation exchange column to be separated at room temperature. Fractions were collected at each FCV. The same procedure was performed with surrogate material prepared with the same mass and ratio of U/^{149}Sm to determine the effectiveness of the UTEVA pre-separation.

2.3 Initial Characterizations of the Irradiated UO_2 Materials

The first characterization of the HFIR material was performed by the previous staff of the laboratory (*17*). These samples had to be sent out of the laboratory for analysis by ICP-MS as Texas A&M University did not have an ICP-MS available for use with radioactive material at the time. The first characterization reported a ^{239}Pu abundance of 89.4% with a burnup of 4.4 ± 0.3 GWd/MTU.

2.3.1 Initial Characterizations of the Irradiated $^{dep}UO_2$ Material

The characterizations of the HFIR material were reevaluated as reported here on October 19th, 2017 with the newly installed Thermo Fisher Scientific iCAP RQ mass spectrometer made available for use with radioactive materials at Texas A&M University. Four 0.04% aliquots of the dissolved HFIR material were diluted into 10 mL of 2% HNO_3 (v/v) for assay by ICP-MS. The measured Pu isotopics are reported in Table 2.01. $^{238}U^{1}H$ molecular interference corrections were performed using the U calibration standard in these unseparated samples.

In addition, most of the isotope ratios of interest to the maximum likelihood forensic methodology were measured directly in these samples, as reported in Table 2.02. ^{154}Eu and $^{134,137}Cs$ were assayed by γ spectrometry; all other ratios were measured using ICP-MS. A ^{137}Cs assay via γ spectrometry was used to perform a burnup calculation using a cumulative fission yield of 6.5% and an enthalpy of 198.5 MeV per fission (*16*). A summary of the HFIR pellet's features as measured here are reported in Table 2.03.

Table 2.01. Measured Pu Isotopics of the Irradiated $^{dep}UO_2$ Material. Isotopics were decay corrected to the date of discharge from 11.4 mg of $^{dep}UO_2$.

Quantity	^{239}Pu	^{240}Pu	^{241}Pu	^{242}Pu
Measured Vector (%)	88.9 ± 0.04	7.36 ± 0.04	3.61 ± 0.04	0.167 ± 0.002
Measured Mass (μg)	194 ± 9	16.1 ± 0.7	7.9 ± 0.4	0.37 ± 0.02

Table 2.02. Measured Isotope Ratios in the Irradiated $^{dep}UO_2$ Material. Reported as of October 19th, 2017. Results Published in (53).

Isotope Ratio	Value	MCNP	$\frac{Simulation}{Experiment} - 1$
$^{154}Eu/^{153}Eu$	$(4.7 \pm 0.2)x10^{-2}$	$4.9x10^{-2}$	5%
$^{134}Cs/^{137}Cs$	$(3.7 \pm 0.2)x10^{-3}$	$4.4x10^{-3}$	17%
$^{135}Cs/^{137}Cs$	$(4.3 \pm 0.4)x10^{-1}$	$4.6x10^{-1}$	8%
$^{137}Cs/^{133}Cs$	$(1.31 \pm 0.09)x10^{0}$	$1.1x10^{0}$	-18%
$^{240}Pu/^{239}Pu$	$(8.28 \pm 0.05)x10^{-2}$	$9.5x10^{-2}$	15%
$^{241}Pu/^{239}Pu$	$(3.30 \pm 0.03)x10^{-2}$	$4.4x10^{-2}$	35%
$^{242}Pu/^{239}Pu$	$(1.88 \pm 0.02)x10^{-3}$	$2.9x10^{-3}$	54%

These initial characterizations indicated that the HFIR material contained fuel-grade Pu (between 82% and 93% ^{239}Pu) rather than the intended weapons-grade Pu. The ^{137}Cs measurement indicated a burnup of 4.4 ± 0.3 GWd/MTU, significantly higher than the intended burnup of 1 GWd/MTU.

Table 2.03. Summary of the Irradiated $^{dep}UO_2$ Material.

Parameter	HFIR Characterization
Burnup (GWd/MTU)	4.4 ± 0.3
$^{total}Pu/U$ (%)	1.9 ± 0.1
^{239}Pu Abundance (%)	88.9 ± 0.04
Neutron Spectrum	Fast-then-Thermal†

†The total neutron spectrum shifted from fast to thermal, as discussed in the main text

Ultimately, this discrepancy was determined to result from the exhaustion of the ^{nat}Gd sheath prior to the end of irradiation. It seems most likely that the sample was placed closer to the HFIR core than initially anticipated, and the amount of ^{nat}Gd available for capture of the thermal neutrons was no longer sufficient by the end of the irradiation. This resulted in a complex irradiation history of the HFIR material, with a total neutron spectrum that started fast then turned thermal. This is described as "Fast-then-Thermal" in Table 2.03. Thus, the irradiation history of the HFIR pellet no longer represented material discharged from the blanket of an FBR, and instead represents highly unique irradiated UO_2.

This complex irradiation history was modeled by my colleague Dr. Jeremy M. Osborn in MCNP6 as closely as possible with the known conditions (*17, 53*). The isotope ratios from the HFIR irradiation reactor model are reported in Table 2.02 along with the experimentally measured isotope ratios reported here. There is generally good agreement between the simulation and experiment except for the

heavier Pu isotope ratios. Disagreement is assumed to result from an imperfect reactor model of the HFIR material's complex irradiation history and neutron energy exposure.

Seven of the ten isotope ratios of interest to the maximum likelihood methodology were measured directly in Table 2.02. The $^{136}Ba/^{138}Ba$ isotope ratio was not able to be measured as the FP source of Ba was lower than the ^{nat}Ba background in the sample. The $^{150}Sm/^{149}Sm$ isotope ratio could not be measured directly due to isobaric interference from ^{150}Nd which was also present as a FP in the sample, at a near 1:1 ratio as ^{150}Sm. The measurement of the $^{150}Sm/^{149}Sm$ isotope ratio required a chemical separation prior to assay; the $^{152}Sm/^{149}Sm$ ratio did not experience isobaric interference, but it is reported along with the other Sm isotope ratio after separation.

2.3.2 Initial Characterizations of the Irradiated $^{nat}UO_2$ Material

The MURR material was initially characterized in a similar way as the HFIR material after dissolution. Three aliquots of 0.16% of the dissolved MURR pellet were diluted into 10 mL of 2% HNO_3 for assay by ICP-MS. A 1% aliquot of the dissolved MURR pellet was placed 28 cm away from the detector face of the HPGe for assay by gamma spectrometry. The Pu isotopics as assayed via ICP-MS are reported in Table 2.04. Six of the isotope ratios of interest to the forensic methodology were measured directly through some combination of γ spectrometry and mass spectrometry, reported in Table 2.05. A summary of the MURR material is reported in Table 2.06.

Table 2.04. Measured Pu Isotopics of the Irradiated $^{nat}UO_2$. Isotopics were decay corrected to the date of discharge from 14.4 mg of $^{nat}UO_2$. Results published in (16).

Quantity	^{239}Pu	^{240}Pu	^{241}Pu	^{242}Pu
Measured Vector (%)	95.20 ± 0.04	4.53 ± 0.02	0.26 ± 0.01	0.0079± 0.0008
Measured Mass (μg)	20.1 ± 0.8	0.96 ± 0.04	0.054 ± 0.005	0.0017 ± 0.0002

Table 2.05. Measured Isotope Ratios in the Irradiated $^{nat}UO_2$ Material. Reported as of October 19th, 2017. Results published in (53).

Isotope Ratio	Value	MCNP	$\frac{Simulation}{Experiment} - 1$
$^{134}Cs/^{137}Cs$	$(3.8 \pm 0.3)x10^{-3}$	$4.2x10^{-3}$	8%
$^{135}Cs/^{137}Cs$	$(3.0 \pm 0.2)x10^{-1}$	$2.7x10^{-1}$	-7%
$^{137}Cs/^{133}Cs$	$(9.8 \pm 0.6)x10^{-1}$	$9.5x10^{-1}$	-3%
$^{240}Pu/^{239}Pu$	$(4.76 \pm 0.03)x10^{-2}$	$4.2x10^{-2}$	-11%
$^{241}Pu/^{239}Pu$	$(2.6 \pm 0.1)x10^{-3}$	$2.3x10^{-3}$	-14%
$^{242}Pu/^{239}Pu$	$(6.0 \pm 0.8)x10^{-5}$	$3.3x10^{-5}$	-45%

The $^{154}Eu/^{153}Eu$ isotope ratio could not be measured for the MURR material because the activity of ^{154}Eu was below the LLQ of both the HPGe and ICP-MS used. This was a result of the lower burnup of the MURR material, reported as 0.97 ± 0.03 GWd/MTU by the ^{137}Cs measurement. The MURR irradiation was relatively successful, discharged with weapons-grade Pu at the intended burnup.

Table 2.06. Summary of the Irradiated $^{nat}UO_2$ Material.

Parameter	MURR Characterization
Burnup (GWd/MTU)	0.97 ± 0.03
$^{total}Pu/U$ (%)	0.15 ± 0.01
^{239}Pu Abundance (%)	95.20 ± 0.04
Neutron Spectrum	Thermal

The MURR material generally contained fewer FPs and Pu than the HFIR material due to its lower burnup. The MURR reactor model was burned using MCNP6 by the forensics collaboration to predict the FP distribution contained within the MURR material (*16*). The comparison between simulation and experiment agreed quite well for all isotope ratios of interest except for $^{242}Pu/^{239}Pu$, per Table 2.05. The simulation's poor agreement with the $^{242}Pu/^{239}Pu$ isotope ratio likely originated from the small mass of ^{242}Pu produced at 1 GWd/MTU, measured as 1.7 ± 0.2 ng (Table 2.04).

2.4 Lanthanide Separations of the Irradiated UO_2 Materials

The $^{150}Sm/^{149}Sm$ isotope ratio could not be measured directly in either the HFIR or MURR material due to isobaric interference from ^{150}Nd which is also produced as a FP. A chemical separation was performed on both irradiated UO_2 pellets to separate these lanthanide elements and measure the final isotope ratio for

the forensics methodology. As lower burnup material, the MURR pellet expressed a higher U/^{149}Sm ratio than the HFIR pellet.

In the initial round of mass spectrometry, the U/^{149}Sm ratio was measured as (1.1 ± 0.1)x10^5 and (1.7 ± 0.1)x10^6 in the HFIR and MURR pellets, respectively. Experimentally, it was observed that the MURR pellet required a pre-separation to sequester this U prior to the lanthanide separation, while the HFIR pellet did not. Due to the lower FP concentration in the low burnup MURR material, a larger fraction of the pellet had to be loaded onto the cation exchange column. This partially saturated the column in the initial separation performed without the U pre-separation, resulting in poor performance. UTEVA resin with a 4 M HNO_3 mobile phase was chosen to pre-separate the U from the lanthanide elements in the MURR pellet.

2.4.1 Developing Separation Procedures with Surrogate Material

Lanthanide separations were performed with surrogate material to standardize the separation conditions prior to application with the HFIR and MURR pellets. Surrogate material was made using ICP-MS standards of the lanthanide elements. The chromatogram of the 60 °C surrogate separation containing 1.75 μg of Ce, Nd, Sm, Eu, Gd, and U each is shown in Figure 2.09 (*44*). The separation resolutions (R_s, Section 1.2.1) between Sm-Gd, Sm-Eu, and Sm-Nd are reported in Table 2.07 where they are compared to the room temperature (24 °C) separation performed with the same surrogate material. R_s (Equation 1.30) was determined only for these elution pairs because they are the only ones relevant to measuring the Sm isotope ratios in the irradiated pellets.

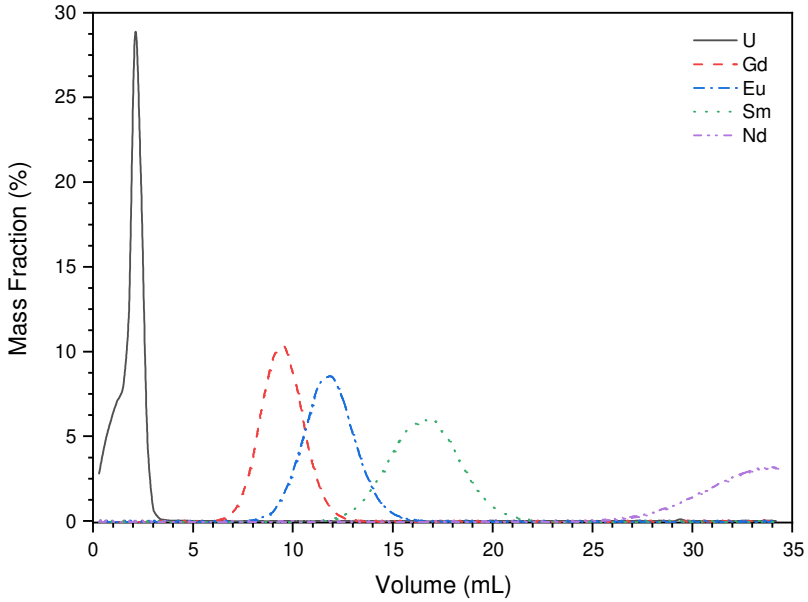

Figure 2.09. Lanthanide Separation of the Surrogate Material. Lanthanide separation performed with a strong cation exchange stationary phase and a 0.4 M α-HIB mobile phase at pH 3.00 eluted at 60 °C and 0.5 mL min^{-1}. Complete separation is obtained between Sm and Nd; the entire Nd curve was not collected during chromatography. Presented with permission as published from (44).

Table 2.07. Separation Resolutions in the Surrogate Separations.
Results published in (44).

Elution Pair	R_s at 60 °C	R_s at 24 °C
Sm-Gd	1.3	1.0
Sm-Eu	0.81	0.64
Sm-Nd	≥ 1.3	≥ 1.0

The entire Nd elution peak was not captured in any of the separations, so R_s could not be measured for the Sm-Nd elution pair. It can be seen in Figure 2.09,

however, that the Sm-Nd elution pair is at least as well resolved as the Sm-Gd pair. Thus, R_s for Sm-Nd is indicated as greater than R_s for Sm-Gd in Table 2.07. The weakest separation is seen between the neighboring elements Sm and Eu; however, none of the Sm or Eu nuclides of interest to the methodology experience isobaric interference with each other. The separation resolution between most peaks at 60°C was approximately 30% higher than at 24°C, but this provided little practical benefit while presenting technical challenges for the HFIR and MURR separations which must be performed within a contained glovebox.

In general, there was complete separation between Sm-Nd and only partial separation between Sm-Eu at either temperature. As a result, it was chosen to perform the pellet separations at room temperature, which still had adequate separation to measure the Sm isotope ratios. At equal masses, U is seen to elute prior to any of the relevant lanthanides; however, the peak was expected to broaden over the entire chromatogram in the actual pellet separations, which contained up to 2000 times more U than the surrogate separations.

The UTEVA pre-separation was evaluated with the surrogate material before it was applied to the MURR pellet. The lanthanide fraction of the surrogate UTEVA pre-separation contained (93 ± 1)% of the total lanthanide mass loaded into the cartridge; the U fraction contained (100 ± 1)% of the loaded U. The U/^{149}Sm ratio was reduced from (1.7 ± 0.1)x10^6 down to 0.14 ± 0.02 in the lanthanide fraction after the pre-separation of the surrogate material. This demonstrated the effectiveness of

the UTEVA pre-separation to reduce the U/^{149}Sm ratio in the MURR pellet by 7 orders of magnitude prior to loading the solution onto the cation exchange column.

2.4.2 Separating the Irradiated $^{dep}UO_2$ Material

The chromatogram of the separation performed on a 2% aliquot of the dissolved HFIR pellet at 24°C without a UTEVA pre-separation is shown in Figure 2.10 (*44*). Separation resolutions are reported in Table 2.08 and are compared to the surrogate separation performed at 24°C. The Sm-Pm pair is not reported for the surrogate separation because Pm is not naturally abundant and was not added to the surrogate material. The results show that a UTEVA pre-separation was not required for the higher burnup HFIR pellet with a U/^{149}Sm ratio of (1.1 ± 0.1)x10^5, as R_s for each of the lanthanide pairs was within 10% of the surrogate separation performed at the same temperature with a U/^{149}Sm ratio of 1.

Figure 2.10 shows the elution profile of the 158, 153, 147, and 150 mass bins after separation of the HFIR pellet. The 147-mass bin shows the elution of both ^{147}Sm and ^{147}Pm, and the 150-mass bin shows the elution of both ^{150}Sm and ^{150}Nd. The chromatogram shows complete separation between Sm and Nd, allowing the ^{150}Sm/^{149}Sm isotope ratio to be accurately measured as necessary for application with the maximum likelihood methodology. The elution profiles of ^{154,155}Eu were measured via γ spectrometry in Figure 2.11 (*44*) and shown to agree with the elution profile of ^{153}Eu as assayed by ICP-MS. This agreement verifies the mass spectrometer's capability to measure the ^{153}Eu concentration accurately down to 12 ppt.

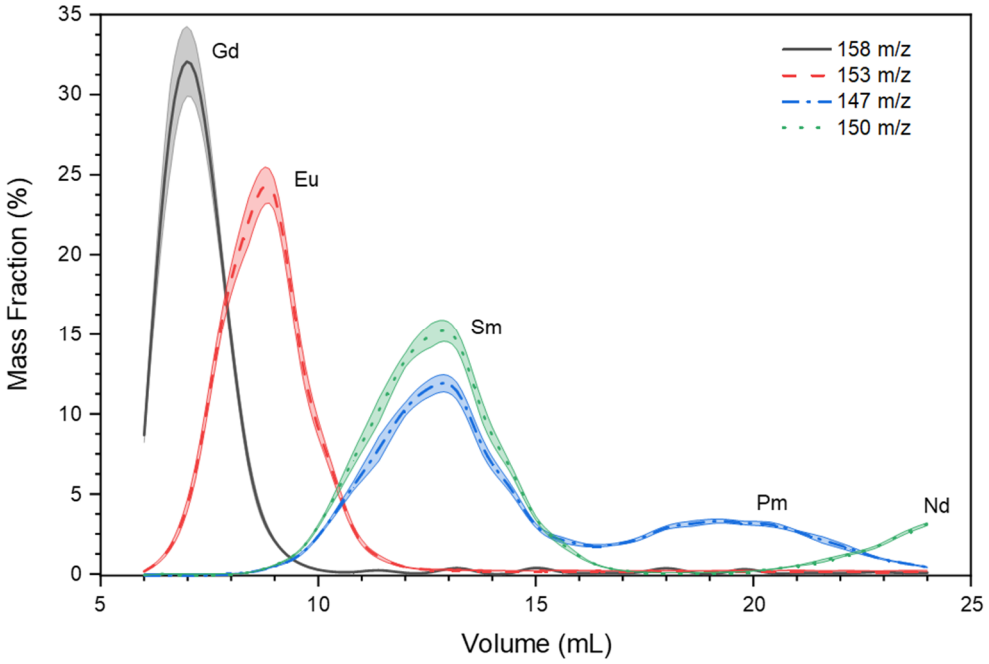

Figure 2.10. Lanthanide Separation of the Irradiated $^{dep}UO_2$ Material. Lanthanide separation performed with a strong cation exchange stationary phase and a 0.4 M α-HIB mobile phase at pH 3.00 eluted at 24 °C and 0.5 mL min^{-1}. Complete separation was obtained between Sm and Nd; centroids are plotted with their 1σ error bands. Presented with permission as published from (44).

Table 2.08. Separation Resolutions in the Separation of the Surrogate and Irradiated $^{dep}UO_2$ Material. Results published in (44).

Elution Pair	R_s of the Surrogate Material at 24 °C	R_s of the $^{dep}UO_2$ Material at 24 °C
Sm-Gd	1.0	1.1
Sm-Eu	0.64	0.67
Sm-Nd	≥ 1.0	≥ 1.1
Sm-Pm	Pm not present	1.1

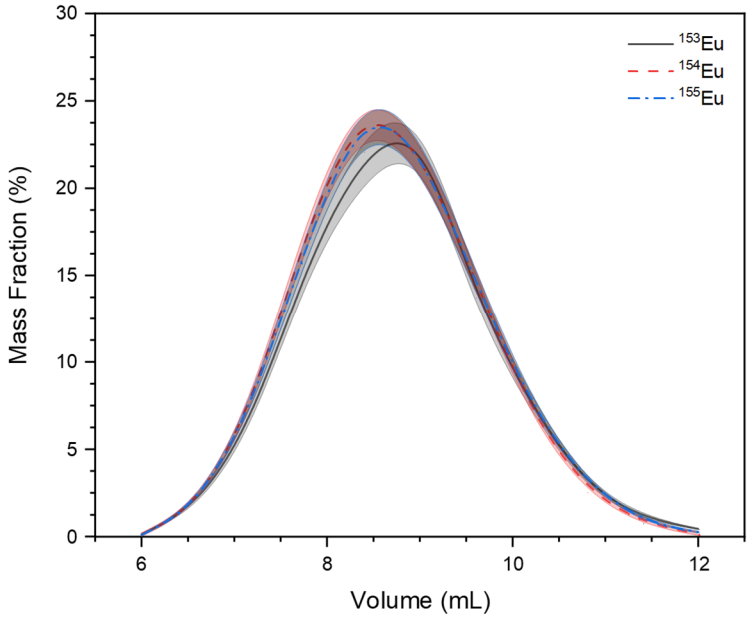

Figure 2.11. Elution of Eu Isotopes in the Separation of the Irradiated $^{dep}UO_2$ Material. The elution of three Eu isotopes in the separation of the $^{dep}UO_2$ material. Centroids are plotted with their 1σ error bands. ^{153}Eu was measured using mass spectrometry while ^{154,155}Eu were measured using γ spectrometry. The consistency with γ spectrometry verifies the ability of the mass spectrometer to measure these trace FPs. Presented with permission as published from (44).

The application of this separation to measure the various Sm isotope ratios is displayed in Figure 2.12, which shows the elution profile of ^{150}Sm with the 150/149 and 152/149 mass bin ratios (*44*). In this figure, a constant value of a mass bin ratio indicates a region which contains no isobars of the corresponding masses. In such a case, the value of the mass bin ratio must be equal to the value of the isotope ratio for the element eluting in the given region. Both the 150/149 and 152/149 mass bin ratios are shown to be constant within the Sm elution peak in Figure 2.12, indicating those masses contain no isobars of ^{149,150,152}Sm in that region.

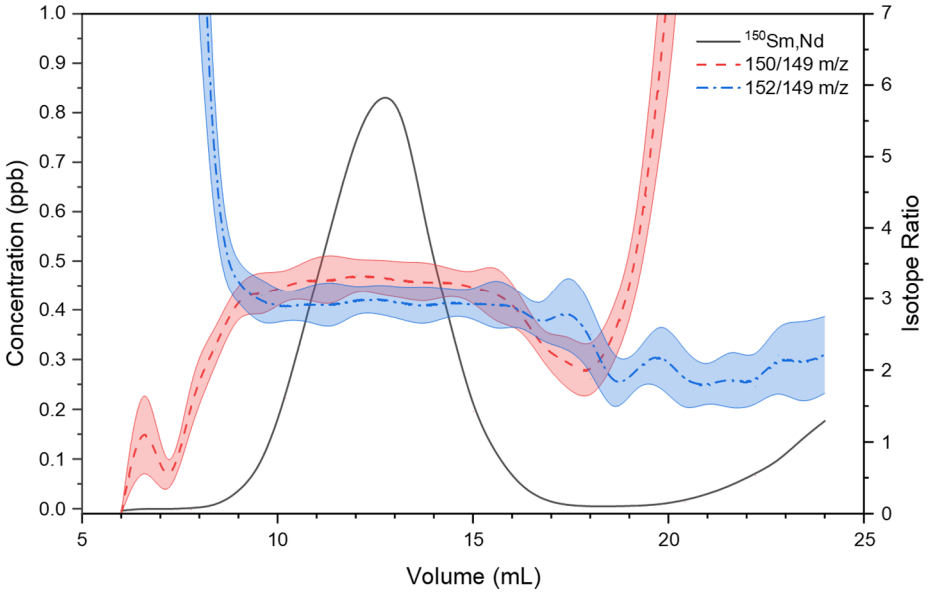

Figure 2.12. Measuring Sm Isotope Ratios in the Irradiated $^{dep}UO_2$ Material. The 150/149 and 152/149 mass bin ratios (right axis) are plotted along with the ^{150}Sm,Nd elution profile (left axis). The mass bin ratios are shown to be constant within the Sm elution peak, indicating they are clear of any isobaric interference. Presented with permission as published from (44).

The $^{150}Sm/^{149}Sm$ and $^{152}Sm/^{149}Sm$ isotope ratios were determined by taking the average of the mass bin ratios within the Sm elution peak. Table 2.09 shows all 21 of the Sm isotope ratios measured this way for the HFIR pellet; every isotope ratio measured was compared to the simulated isotope ratios from MCNP6. Simulations were performed by the forensics collaboration (*17, 53*).

The $^{152}Sm/^{149}Sm$ isotope ratio reported here does not experience any significant isobaric interference in low burnup nuclear fuel. Although ^{152}Eu and ^{152}Gd may be produced during irradiation, their direct fission yields are too low to be measured in these low burnup samples.

Table 2.09. The 21 Measured Sm Isotope Ratios in the Irradiated $^{dep}UO_2$ Material Compared to the Simulated Ratios from MCNP6. Results published in (44).

Isotope Ratio	Measured Value	$\frac{Simulation}{Experiment} - 1$ (%)
$^{150}Sm/^{149}Sm$	3.23 ± 0.09	4.4
$^{152}Sm/^{149}Sm$	2.93 ± 0.04	-10
$^{147}Sm/^{148}Sm$	12.2 ± 0.8	-16
$^{147}Sm/^{149}Sm$	4.2 ± 0.1	0.69
$^{147}Sm/^{150}Sm$	1.31 ± 0.03	5.1
$^{147}Sm/^{151}Sm$	3.97 ± 0.09	18
$^{147}Sm/^{152}Sm$	1.44 ± 0.01	-9.3
$^{147}Sm/^{154}Sm$	4.43 ± 0.08	4.6
$^{148}Sm/^{149}Sm$	0.34 ± 0.05	12
$^{148}Sm/^{150}Sm$	0.104 ± 0.004	16
$^{148}Sm/^{151}Sm$	0.32 ± 0.02	28
$^{148}Sm/^{152}Sm$	0.117 ± 0.003	5.1
$^{148}Sm/^{154}Sm$	0.35 ± 0.03	15.0
$^{149}Sm/^{151}Sm$	0.93 ± 0.02	17
$^{149}Sm/^{154}Sm$	1.03 ± 0.03	1.7
$^{150}Sm/^{151}Sm$	3.02 ± 0.06	13
$^{150}Sm/^{152}Sm$	1.112 ± 0.009	-14
$^{150}Sm/^{154}Sm$	3.3 ± 0.2	-2.7
$^{151}Sm/^{152}Sm$	0.365 ± 0.003	-33
$^{151}Sm/^{154}Sm$	1.12 ± 0.02	-16
$^{152}Sm/^{154}Sm$	3.06 ± 0.04	-16

As such, their total masses in the HFIR pellet are negligible, and they were not detected in any quantity by either mass spectrometry or γ spectrometry. Therefore, ICP-MS was also used to measure the $^{152}Sm/^{149}Sm$ isotope ratio in the unseparated HFIR pellet. The unseparated $^{152}Sm/^{149}Sm$ isotope ratio was measured as 3.0 ± 0.2, which agrees with the $^{152}Sm/^{149}Sm$ isotope ratio of 2.93 ± 0.04 measured using these separation techniques. This result verifies the ability of this separation technique to measure isotope ratios that may otherwise suffer from isobaric interference in unseparated fuels.

In general, the 21 Sm isotope ratios reported in Table 2.09 show good agreement with the MCNP6 simulation, where all but two of the ratios have less than a 20% difference with simulation. The only two ratios that are currently utilized by the maximum likelihood technique are $^{150}Sm/^{149}Sm$ and $^{152}Sm/^{149}Sm$, but these results show there are many more Sm ratios which may be readily measured.

2.4.3 Separating the Irradiated $^{nat}UO_2$ Material

The separation of the 6% MURR pellet aliquot at 24°C with no UTEVA pre-separation resulted in a chromatogram showing no separation between the lanthanides present. As this separation was performed otherwise identically to the HFIR separation, this result implies that the $U/^{149}Sm$ ratio of $(1.7 \pm 0.1)x10^6$ was too high to perform a lanthanide separation without prior sequestration of the U due to saturation of the resin. A UTEVA resin cartridge was chosen to pre-separate the U from the MURR sample because U is well known to adhere to the resin at higher HNO_3 concentrations, while the lanthanide elements continue to elute (*154, 189*).

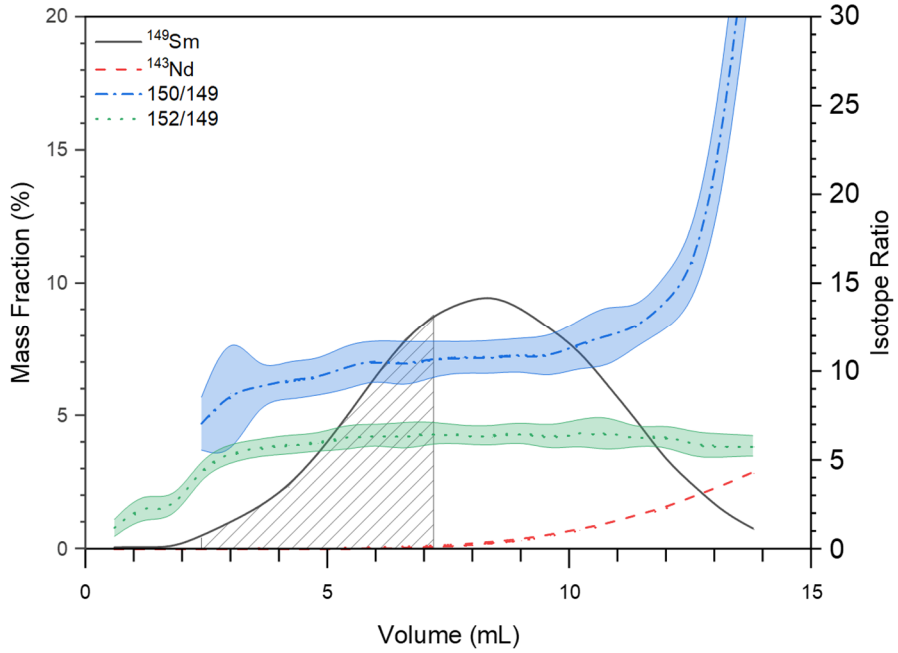

Figure 2.13. Measuring Sm Isotope Ratios in the Irradiated $^{nat}UO_2$ Material. The 150/149 and 152/149 mass bin ratios (right axis) are plotted along with the ^{149}Sm and ^{143}Nd elution profiles (left axis).The shaded region of the ^{149}Sm elution curve represents a portion containing < 0.33% of the total Nd. The Sm isotope ratios were measured only in this shaded region. Presented with permission as published from (44).

The chromatogram from the 20% MURR aliquot separated at 24°C after the UTEVA pre-separation is shown in Figure 2.13 (*44*). The results show significantly poorer separation compared to the HFIR pellet, which was not pre-separated for U. However, it is a significantly improved separation compared to the 6% MURR aliquot which was not pre-separated using the UTEVA cartridge. The results from the surrogate UTEVA pre-separation indicate that nearly 100% of the U is removed from the lanthanides, reducing the U/^{149}Sm ratio by a factor of 10^7 prior to loading in the cation exchange column. At this concentration, the abundance of U cannot be the cause for the poor separation. Although the resin was washed with several bed

volumes of 4 M HNO_3 prior to use, it is possible that some of the diamyl amylphosphonate coated on the UTEVA resin was captured in the lanthanide fraction, which was then loaded into the α-HIB column. It is hypothesized that this potential contamination drastically reduced the effectiveness of the system.

Nevertheless, the separation was still effective enough to measure the $^{150}Sm/^{149}Sm$ isotope ratio as necessary for the maximum likelihood method. This was accomplished by taking the $^{150}Sm/^{149}Sm$ isotope ratio in a region of the Sm elution peak (from 2.4 to 7.2 mL) that was measured to contain less than (0.3 ± 0.1)% of the total Nd. This region was determined using the elution of ^{143}Nd, which has no isobars in the pellet; the same region was measured to contain (37 ± 1)% of the total Sm, measured using ^{149}Sm. Using the simulated total masses of ^{150}Sm and ^{150}Nd in the MURR pellet from MCNP6, the 150 mass bin in the region between 2.4 to 7.2 mL is estimated to be >99% ^{150}Sm. The measured $^{150}Sm/^{149}Sm$ and $^{152}Sm/^{149}Sm$ isotope ratios are presented in Table 2.10.

As with the HFIR pellet, the contribution of ^{152}Eu and ^{152}Gd to the 152-mass bin in the MURR pellet is negligible due to their low cumulative fission yield. Thus, the $^{152}Sm/^{149}Sm$ isotope ratio was measured in the unseparated material as 6.7 ± 0.4, in excellent agreement of the value measured using the separation technique reported in Table 2.10.

Table 2.10. Sm Isotope Ratios Measured in the $^{nat}UO_2$ Material. Results published in (44).

Isotope Ratio	Measured Value	$\frac{Simulation}{Experiment} - 1$ (%)
$^{150}Sm/^{149}Sm$	9.6 ± 0.6	1.6
$^{152}Sm/^{149}Sm$	6.3 ± 0.2	-6.4

2.5 Validation of the Maximum Likelihood Forensics Methodology

The isotopics of the HFIR and MURR pellets measured and reported here were used to validate the maximum likelihood forensics methodology (Section 1.3.4). This validation serves as the first application of the methodology to any irradiated material. This section briefly summarizes the validation of the methodology as performed by the whole of the forensics collaboration (*53*). Other members of the collaboration modeled multiple reactor types including a PHWR, FBR, PWRs operating at various enrichments, and the NRX and Magnox reactors. The Magnox reactor was modeled as the North Korean Yongbyon reactor, and the NRX reactor was modeled as Iran's IR-40 (*53*).

These reactor models were simulated to various burnups and decay corrected to various cooling times; the isotope ratios at each burn-step and decay-step were compared to the measured isotope ratios reported in the previous sections. The similarities between the measured isotope ratios and all the simulated ratios were computed using Equation 1.41 (Section 1.3.4). The closest match was identified at a given burnup and cooling time for each reactor model and reported as the maximum

likelihood for that model. The maximum likelihoods for each modeled reactor type are presented in Tables 2.11 and 2.12 for the HFIR and MURR pellets, respectively (*53*). These tables report maximum likelihood as the natural log of the computed likelihood value. The computed likelihood is not a probability, but a measurement of similarity by Equation 1.41.

Table 2.11. Maximum Likelihood Validation with the HFIR Material. The PWRs are distinguished by fuel enrichment. The maximum ln-likelihood possible is +28.7. Results published in (53).

Reactor Model	Maximum ln Likelihood	Fuel Burnup (GWd/MTU)	Cooling Time (y)
HFIR	+18 ± 5	4.29	1833
MURR	-40 ± 10	3.76	1647
NRX	-40 ± 10	3.71	1524
Magnox	-50 ± 10	2.79	491
PWR (2.35%)	-70 ± 20	≥ 5.31	1861
PHWR	-130 ± 40	3.31	2022
PWR (3.4%)	-280 ± 30	≥ 5.01	792
PWR (4.45%)	$-(5.5 \pm 0.1)\times10^{3}$	≥ 3.90	0
FBR	$-(6.2 \pm 0.1)\times10^{5}$	≥ 4.73	0
Measured Parameters	-	4.4 ± 0.3	1601

Table 2.12. Maximum Likelihood Validation with the MURR Material. The PWRs are distinguished by fuel enrichment. The maximum ln-likelihood possible is +29.8. Results published in (53).

Reactor Model	Maximum Log Likelihood	Fuel Burnup (GWd/MTU)	Cooling Time (y)
MURR	+30 ± 1	1.01	303
NRX	+26 ± 3	1.02	203
Magnox	+13 ± 6	0.73	0
PWR (3.4%)	-6 ± 9	3.89	1371
PWR (4.45%)	-10 ± 10	≥ 3.90	1195
PWR (2.35%)	-10 ± 10	3.04	1162
PHWR	-20 ± 20	0.94	260
HFIR	-170 ± 30	4.40	1788
FBR	$-(1.5 \pm 0.2)\times10^{5}$	≥ 4.73	0
Measured Parameters	-	0.97 ± 0.03	318

The maximum possible ln-likelihood value that could be achieved for the HFIR validation was +28.7. This number was obtained by setting $r_{j,mes} = r_{j,sim}$ in the likelihood computation. Likewise, the maximum possible ln-likelihood value for the MURR validation was +29.8 (*53*). The reported most likely reactor of origin for the HFIR material was the HFIR specific irradiation which was modeled to represent the conditions discussed in Section 2.1.1. This result is unsurprising since the HFIR irradiation was unique with a fast-then-thermal neutron spectrum during

irradiation. The FBR origin is not likely for the HFIR pellet because approximately 75% of the total HFIR burnup was produced after the ^{nat}Gd sheath was exhausted, when the pellet was exposed to a large flux of thermal neutrons (*17, 53*). The methodology correctly predicted the fuel burnup and cooling time of the HFIR pellet in Table 2.11.

The reported most likely reactor of origin for the MURR material was the MURR-specific irradiation which was modeled to represent the conditions discussed in Section 2.1.2. The computed likelihood of this origin was within error of the maximum possible likelihood of + 29.8, indicating a strong match with the reactor model. This result is significant as the MURR material was designed to be similar in nature to fuel discharged from the core of a thermal ^{nat}U fuel reactor at 1 GWd/MTU.

The second most likely reactor origin was predicted as Iran's NRX reactor. This is a reasonable prediction as the NRX reactor is also a thermal neutron reactor with ^{nat}U fuel. The enriched U fueled PWRs and the fast neutron FBR were computed as a much less likely reactor origin of the MURR material. The methodology correctly predicted the burnup and cooling time of the MURR pellet in Table 2.12. "Heatmaps" of the final maximum likelihood results for the HFIR and MURR pellets are shown in Figures 2.14 and 2.15, respectively (*53*).

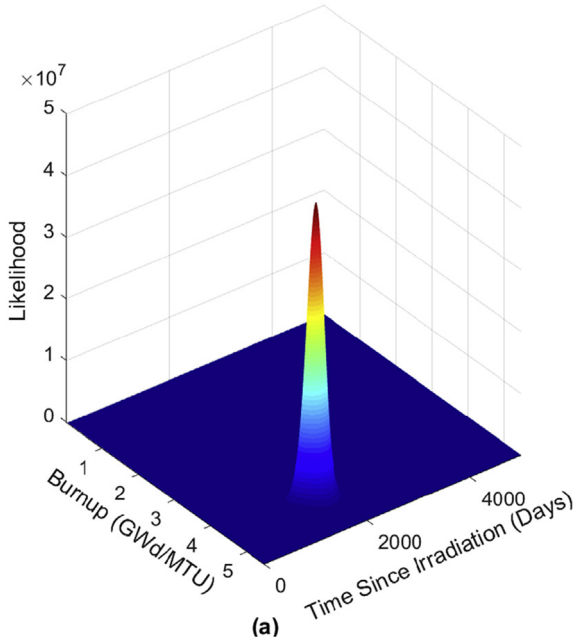

Figure 2.14. Maximum Likelihood Heatmap of the Irradiated $^{dep}UO_2$ Material. A heatmap showing the computed likelihoods of the possible burnups and cooling times of the HFIR material. Only a narrow range of burnups and likelihoods are computed with likelihoods close to the maximum likelihood. The maximum possible likelihood is 2.91×10^{12}. Presented from an open access publication (53)

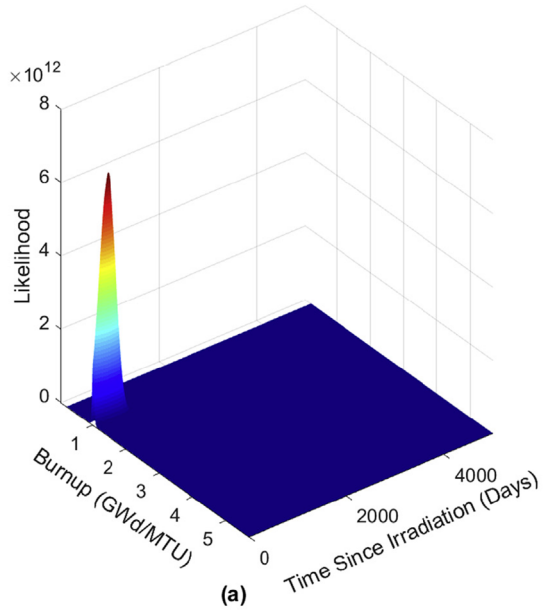

Figure 2.15. Maximum Likelihood Heatmap of the Irradiated $^{nat}UO_2$ Material. A heatmap showing the computed likelihoods of the possible burnups and cooling times of the MURR material. Only a narrow range of burnups and likelihoods are computed with likelihoods close to the maximum likelihood. The maximum possible likelihood is 8.75×10^{12}. Presented from an open access publication (53)

CHAPTER III

ISOLATING TRACE FISSION PRODUCT ELEMENTS FROM SEPARATED SUPER-GRADE PLUTONIUM

In Chapter II, the maximum likelihood forensics methodology (*52-54*) was validated against two different irradiated UO_2 pellets; however, it was intended to ultimately apply this methodology to samples of separated Pu containing only trace amounts of the FP elements. The forensics collaboration has modeled and simulated thermal neutron reactors utilizing ^{nat}U fuels to produce weapons-grade Pu at burnups as low as 1 GWd/MTU (*16*). The mass of each FP nuclide of interest to the methodology produced under these conditions is reported in Table 3.01, before and after a PUREX process DF of 10^7 – 10^8 (*185*).

A sample of 5 g PUREX separated Pu is expected to contain at least 10^{-10} g of all the FPs of interest to the methodology except for ^{134}Cs, ^{136}Ba, and ^{154}Eu (*16*). ^{134}Cs and ^{154}Eu are gamma-active radionuclides which are readily assayed by γ spectrometry to activities as low as 2 Bq, corresponding to 40 and 200 fg of ^{134}Cs and ^{154}Eu, respectively. From the previous investigations (*53*), the applicability of Ba with the methodology is questionable due to the relatively high levels of ^{nat}Ba contamination found in standard laboratory materials. Therefore, in order to apply the maximum likelihood forensic methodology to samples of separated Pu, a procedure which is capable of isolating 10^{-10} g of the FP nuclides out of 5 g of separated Pu must be developed.

Table 3.01. Fission Product Production Rates in Low Burnup ^{nat}U Containing Weapons-Grade Pu. Simulated Using MCNP6 with the MURR Model (16). PUREX DFs originate from (185).

Nuclide	Mass ratio (g FP/g Pu)	Mass Ratio after PUREX (g FP/g Pu)	Mass in 5 g of PUREX Separated Pu (g)
^{133}Cs	2.60×10^{-2}	1.98×10^{-10}	9.91×10^{-10}
^{134}Cs	8.86×10^{-5}	6.76×10^{-13}	3.38×10^{-12}
^{135}Cs	6.79×10^{-3}	5.18×10^{-11}	2.59×10^{-10}
^{137}Cs	2.47×10^{-2}	1.88×10^{-10}	9.41×10^{-10}
^{136}Ba	8.01×10^{-5}	1.05×10^{-12}	5.27×10^{-12}
^{138}Ba	2.71×10^{-2}	3.56×10^{-10}	1.78×10^{-9}
^{149}Sm	4.55×10^{-4}	2.17×10^{-11}	1.08×10^{-10}
^{150}Sm	4.42×10^{-3}	2.11×10^{-10}	1.05×10^{-9}
^{152}Sm	2.67×10^{-3}	1.27×10^{-10}	6.36×10^{-10}
^{153}Eu	8.97×10^{-4}	4.27×10^{-11}	2.14×10^{-10}
^{154}Eu	2.99×10^{-5}	1.42×10^{-12}	7.11×10^{-12}

3.1 Experimental Methods

The mass of 5 g separated Pu was chosen as the approximate minimum mass of Pu which contains at least 10^{-10} g of each FP nuclide of interest to the forensics methodology for assay via ICP-MS. This limit was chosen because a fraction containing 10^{-10} g of a single FP element would have a total concentration of 10 ppt in a 10 mL sample prepared for assay by ICP-MS, nearing the detection limit of the

instrument. The chemical methodology described here uses benchtop chromatography techniques to isolate and concentrate these trace FPs of interest out of much larger samples of separated Pu.

Benchtop chromatography was chosen because it may be readily scaled up to samples as large as 5 g of Pu, while modern applications of HPLC in actinide chemistry do not exceed sample sizes over 10^{-2} g (*190-193*). Two samples of Pu were used to characterize this chemical methodology: a 4.0 mg sample of separated super-grade Pu and a 61.1 mg sample of separated super-grade Pu, hereafter referred to as Plutonium 1 and Plutonium 4, respectively. Super-grade Pu is defined as any Pu with a ^{239}Pu isotopic abundance greater than 97%. These were the largest samples of Pu available to the author for analysis; scale up procedures for samples as large as 5 g of Pu are discussed in Section 3.3.2.

3.1.1 Reagents

The separated Pu was obtained from LANL as super-grade Pu with an isotopic vector of 99.95% ^{239}Pu. The ^{137}Cs, ^{152}Eu, ^{133}Ba, and ^{233}U radiotracers were also obtained from LANL solvated in HNO_3 with an undocumented history. All acids used were purchased in the concentrated form as Optima grade from Fisher Scientific. All anion exchange resin used was macroporous, purchased as AG MP-1 from Bio-Rad. All cation exchange resin used was Dowex 50W X4 purchased from Sigma Aldrich. Strontium resin (SR resin) was purchased as 100 – 150 μm particle size from Eichrom. The $NaNO_2$ was purchased as 99.999% trace metal grade from Sigma Aldrich. All 3 mL and 20 mL columns used were purchased from Evergreen.

3.1.2 Safety and Security

All work involving > 167 kBq (4.5 μCi, 73 μg) of ^{239}Pu was performed in the Actinide Research Facility (ARF) at LANL. This facility is specifically designed and regulated for work with significant activities of the transuranic elements.

The primary safety concerns in this method include laboratory and personnel contamination. To minimize the risk of contamination, proper safety equipment should include double gloves, disposable sleeves, and disposable booties in addition to standard laboratory attire. Under the conditions used in this method, the critical mass of ^{239}Pu is between 0.5 – 2.2 kg, well above the mass of material present (*194*).

3.1.3 Dissolution of the Pu Materials

Plutonium 1 originated as a white crystalline solid of an unidentified speciation. This material dissolved readily upon the addition of 8 M HNO_3, producing a dark green solution characteristic of Pu^{IV} in HNO_3. Plutonium 4 originated as a dry green powder identified as the most common oxide, PuO_2. This material dissolved over several hours in concentrated HCl, producing a dark red solution characteristic of Pu^{IV} in HCl. The other two Pu materials (Plutonium 2 and Plutonium 3) are discussed in Chapter IV but were not used in the methodology reported here.

3.1.4 Mass Spectrometry

Mass spectrometry was performed with the same Thermo Fisher Scientific iCAP RQ mass spectrometer available for use with radioactive materials as in Chapter II. In general, the same protocols for handling the contaminated components were followed here. All solutions used for ICP-MS were diluted to a total volume of 10 mL

with 2% HNO_3 (v/v). All 2% HNO_3 used here was prepared as 2% by volume. Elemental calibration standards were used to calibrate the mass spectrometer for each of the FP nuclides of interest.

The LLQ was set at 10 standard deviations above the background mean. The LLQ is reported for each nuclide of interest in Table 3.02. The final column reports the LLQ of the mass spectrometer in terms of total FP mass in the separated Pu; however, these samples were diluted by an extra factor of 10 than necessary for precautionary reasons. Mass bias and molecular interference corrections were performed as appropriate according to Section 1.3.1. Background corrections were performed with sample blanks produced by eluting acid through the same chromatography resins as the Pu samples.

3.1.5 Gamma Spectrometry

Gamma spectra were taken at sample distances between 1.15 cm and 9.0 cm from the detector face of a Canberra Standard Electrode Coaxial high-purity germanium (HPGe) detector cooled with liquid nitrogen and shielded with lead. Energy and efficiency calibrations were performed using a ^{152}Eu NIST-traceable calibration standard purchased from Eckert and Ziegler. Energy and efficiency calibrations representative of typical operation are shown in Figures 2.07 and 2.08 (Section 2.2.4). The ^{137}Cs, ^{152}Eu, ^{133}Ba, and ^{233}U radiotracers were added in ultra-trace concentrations, so detection limits in γ spectrometry are carefully considered in Section 3.2.1. In general, the LLQ of most radionuclides in most samples was between 1 – 2 Bq.

Table 3.02. The Lower Limit of Quantification for Each Nuclide of Interest by Mass Spectrometry. The LLQ is reported for both the concentration of the assayed solution, and the total mass in the original sample.

Nuclide	LLQ (ppt)	LLQ (ng)
^{239}Pu	4	0.4
^{240}Pu	4	0.4
^{241}Pu	4	0.4
^{242}Pu	4	0.4
^{233}U	4	0.4
^{235}U	4	0.4
^{153}Eu	10	1
^{154}Eu	4	0.4
^{149}Sm	3	0.3
^{150}Sm	4	0.4
^{152}Sm	5	0.5
^{133}Cs	5	0.5
^{134}Cs	30	3
^{135}Cs	20	2
^{137}Cs	40	4
^{136}Ba	50	5
^{138}Ba	300	30

3.1.6 Ion Exchange and Extraction Chromatographies

Plutonium 1 was used to develop all of the following chromatography procedures. Radiotracers of ^{137}Cs (165 Bq, 51 pg), ^{152}Eu (53 Bq, 8.2 pg), ^{133}Ba (73 Bq, 7.8 pg), and ^{233}U (830 Bq, 2.3 μg) were added to Plutonium 1 from an HNO_3 solution to determine the elution yield of those elements in the following procedures. Low activities were used so the radiotracers would minimally perturb the sample. In addition, these ultra-trace masses better represent the goal of isolating ultra-trace FPs from bulk Pu material. ^{233}U (830 Bq, 2.3 μg) was the only radiotracer added to Plutonium 4. Each chromatographic separation was designed based on systems previously described in the literature, combined to achieve the specific goals discussed in this work (*147, 148, 172-174, 195*).

All columns used in this work were pre-washed by eluting 10 bed volumes (V_B) of each eluent in reverse order. The resin V_B for the first anion exchange column was 5 mL for Plutonium 1 and 12 mL for Plutonium 4. The follow-up anion exchange columns were 1 mL for both samples. The resin V_B of all cation exchange and SR resin columns was 1 mL.

^{235}U was isolated from the Pu samples as a daughter resulting from the radioactive decay of ^{239}Pu. 55 μL of a 1.5 M $NaNO_2$ solution was added to Plutonium 1 (5:1 mol ratio) in 5 mL of 8 M HNO_3. Pu is known to disproportionate into four valence states in solution; $NaNO_2$ is used to fix Pu as primarily Pu^{IV} in HNO_3 over a short redox period.

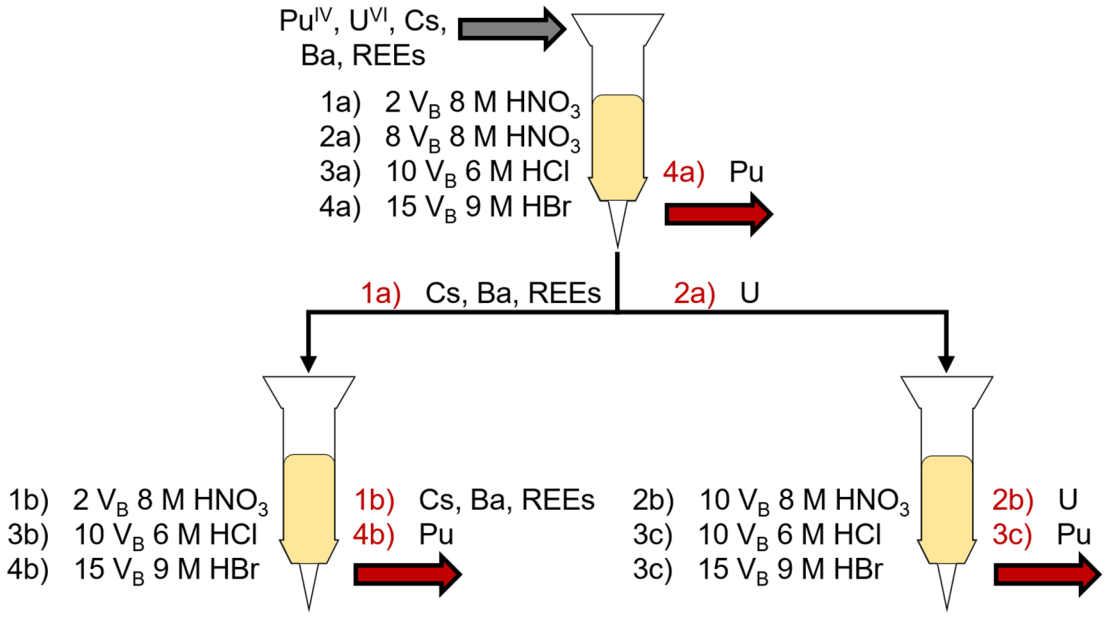

Figure 3.01. Anion Exchange Chromatography of the Separated Pu. The chromatography scheme used to isolate the trace U from Pu on AG MP-1 anion exchange resin (yellow). The streams with black numbers represent eluents; the red numbers represent the corresponding eluates. V_B refers to a volume equal to the bed volume of the resin. The HCl eluent was used solely to rinse HNO_3 off the column prior to eluting HBr.

The solution was heated at 120 °C for several hours to dryness to minimize the amount of Pu^{III} in solution. The dried solution was reconstituted in a small volume of 500 µL of 8 M HNO_3 prior to loading it onto the column.

The elution scheme used to isolate U is described in Figure 3.01, using AG MP-1 anion exchange resin (yellow). Each eluent is indicated using black numbers (left of each column); the corresponding eluates are indicated with red numbers (right of or below each column). The first FP eluate (1a in Figure 3.01) and U eluate (2a in Figure 3.01) were each loaded separately onto a second anion exchange column of the same design. The resulting FP eluate (1b) was used in the

following procedures; the resulting U eluate (2b) was evaporated to dryness and reconstituted in 5 mL of 2% HNO_3. A 10% aliquot was further diluted to 10 mL of 2% HNO_3 for assay by ICP-MS. The same procedure was repeated for Plutonium 4.

Caution should be exercised any time HBr and HNO_3 are used in the same procedure. Mixing these two acids may create a violent redox mixture prone to "spitting" or "bumping" when heated; it is recommended to rinse the column with at least 10 V_B of a less reactive acid (such as HCl) prior to using HBr. The HCl eluents in Figure 3.01 were used solely to rinse HNO_3 off the column prior to using HBr. These HCl fractions were ultimately combined with the Pu fractions at the end of the procedure.

The FP fraction from the prior step (eluate 1b) should contain all the Cs, Ba, and rare-earth elements (REEs). This eluate was evaporated to dryness and reconstituted in a small volume (500 µL) of concentrated HNO_3. This solution was loaded onto a cation exchange column and eluted with 2 V_B of concentrated HNO_3 to collect a fraction containing the Cs and Ba. The REE fraction was subsequently eluted with 15 V_B of 6 M HCl. The REE fraction was evaporated to dryness and reconstituted in 5 mL of 2% HNO_3; a 10% aliquot was further diluted to 10 mL of 2% HNO_3 for assay by ICP-MS. The same procedure was repeated for eluate 1b of Plutonium 4.

All the plastic and glassware used to handle or store Plutonium 4 up to this point was thoroughly soaked with deionized H_2O, 2% HNO_3, and 8 M HNO_3 for one week each to leach residual Ba and minimize natural Ba contamination in the sample.

The Cs/Ba fraction from the prior step was evaporated to dryness and reconstituted in a small volume (500 µL) of 5 M HNO_3. This residue was loaded onto an SR resin column (a Sr selective resin by Eichrom) and eluted with 2 V_B of 5 M HNO_3. This fraction contained the Cs. The Ba was then eluted from the column with 15 V_B of 0.1 M HNO_3; both fractions were evaporated to dryness and reconstituted with 5 mL of 2% HNO_3. 10% aliquots were further diluted to 10 mL of 2% HNO_3 for assay by ICP-MS.

3.2 Chromatography Yield Determination

The radiotracers added to Plutonium 1 were used to determine the relative column yields of each element fraction in the separations performed. Because the radiotracers were added in ultra-trace masses, the detection limit of the HPGe used was studied in detail.

3.2.1 Detection Limits in Gamma Spectrometry

The decision threshold (T_D), also referred to as the lower limit of detection (LLD) or the minimum detectable activity (MDA), was calculated individually for all radionuclides in each sample using Equations 3.01 and 3.02, as per ISO 11929-3(2019) sections B.2 and B.6 (*196*). The MDA represents the minimum activity of a radionuclide that may be distinguished as above background to the stated significance level *α*. Equation 3.01 describes a scenario in which there is no photopeak in the background spectrum, thus the MDA is dependent entirely upon noise and Compton scattering events in the sample spectrum. In Equation 3.01, *k* is the significance interval (set at 3.09, α = 0.001 for a one-tailed distribution), *t* is time,

R_l is the count rate of total events in a region of interest spanning l channels to the left (l_l)of the photopeak's position, R_r is the same l channels to the right (l_r) of the photopeak's position, and b is the total number of channels spanned by the photopeak. In cases where no photopeak was apparent in the sample spectrum, the expected position and span of the photopeak was determined by other spectra (using the same calibration) which did contain a measurable photopeak for the given FP.

$$MDA = k\sqrt{\frac{R_l + R_r}{t}\left(1 + \frac{b}{l_l + l_r}\right)} \tag{3.01}$$

Equation 3.02 describes a scenario in which there is a photopeak in the background spectrum, thus the MDA is dependent upon noise, Compton scattering events, and the background rate. The variables in Equation 3.02 are defined the same as Equation 3.01, where the subscript s refers to data from the sample spectrum, subscript b refers to data from the background spectrum, and R_b is the count rate of the photopeak in the background spectrum (above baseline).

$$MDA = k\left[\frac{R_{l,s} + R_{r,s}}{t}\left(1 + \frac{b}{l_{l,s} + l_{r,s}}\right) + \frac{R_{l,b} + R_{r,b}}{t_b}\left(1 + \frac{b}{l_{l,b} + l_{r,b}}\right) + R_b\left(\frac{1}{t_s} + \frac{1}{t_b}\right)\right]^{\frac{1}{2}} \tag{3.02}$$

The detection limit (L_D) was set at 3.09σ (α = 0.001) above the MDA. The L_D describes the minimum activity of a radionuclide that may be positively identified as above background to the stated significance level α.

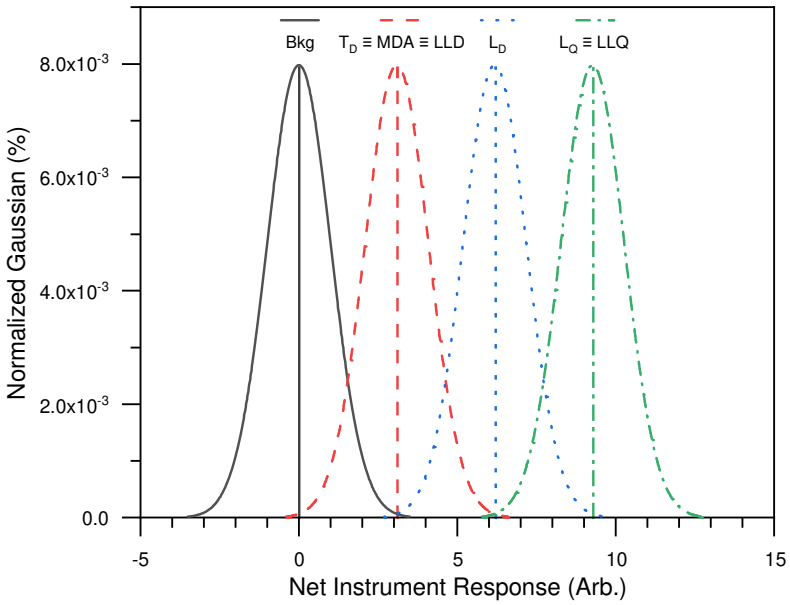

Figure 3.02. Detection Limits in Gamma Spectrometry. The net background (Bkg), MDA, L_D, and LLQ distributions as a function of net instrument response. The net background rate must be zero by definition; the standard deviation is set at one for ease of interpretation. The centroid of each distribution is displayed as a vertical line down to the axis.

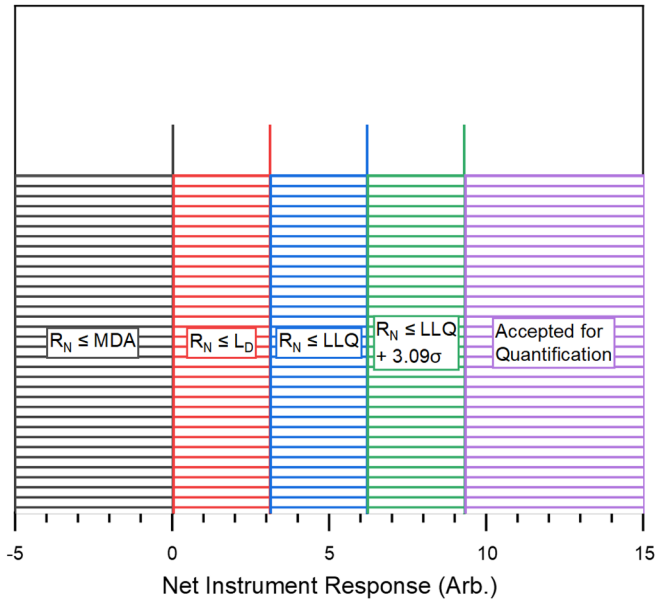

Figure 3.03. Applied Detection Limits in Gamma Spectrometry. The appropriate parameter to report for a net instrument response (R_N) which falls in any region below the LLQ of the system. The vertical lines match exactly with the centroids in Figure 3.02.

The quantification limit (L_Q), more often referred to as the lower limit of quantification (LLQ), was set at 3.09σ (α = 0.001) above the L_D. The LLQ refers to the minimum activity of a radionuclide that may be accepted for quantification.

Figure 3.02 shows the centroids and distributions of the net background rate (Bkg), MDA, L_D, and LLQ as interpreted for this work. The standard deviation is approximated to be equivalent for all four distributions. This approximation is made because in radiation detection the standard deviation is a function of the number of counts (N), which will be similar for all four distributions as the count rate approaches background.

Figure 3.03 describes how these intervals are used for data analysis; if a measured activity falls in the black region, then it is reported as less than the MDA. This conclusion can be made to the α = 0.001 significance level because less than 0.1% of the MDA distribution (red curve from Figure 3.02) resides within the black region in Figure 3.03. Likewise, any activity measured in the red region in Figure 3.03 is reported as less than the L_D, the blue region less than the LLQ, and the green region less than the LLQ + 3.09σ. Any activity measured in the purple region or above is accepted for quantification. The variables described in Equations 3.01 and 3.02 related to the background spectrum are reported in Table 3.03, and the MDA, L_D, and LLQ are reported for all radionuclides of all eluates in Tables 3.04 to 3.07.

Table 3.03. Background Parameters of the Gamma Spectrometer.

Radionuclide	Photopeak (keV)	Background Rate (s^{-1})	$R_{l,b} + R_{r,b}$ (s^{-1})	b
^{235}U	185.7	$(1.22 \pm 0.09)x10^{-2}$	0.100	15
^{152}Eu	121.4	$(2.0 \pm 0.1)x10^{-2}$	0.139	15
^{133}Ba	352.6	$(1.10 \pm 0.08)x10^{-2}$	0.045	15
^{137}Cs	662.2	$(2.23 \pm 0.06)x10^{-2}$	0.022	22

Table 3.04. Activities and Statistics of the U Eluate from Plutonium 1.
Counted for 6687 real seconds with 0.06% dead time.

Radionuclide	Activity (Bq)	$R_{l,s} + R_{r,s}$ (s^{-1})	MDA (Bq)	L_D (Bq)	LLQ (Bq)
^{235}U	0.2 ± 0.1	0.123	0.44	0.89	1.33
^{152}Eu	1.0 ± 0.2	0.166	0.85	1.70	2.54
^{133}Ba	-(0.41 ± 0.03)	0.052	0.46	0.92	1.38
^{137}Cs	1.2 ± 0.2	0.023	0.43	0.86	1.29

Table 3.05. Activities and Statistics of the REE Eluate from Plutonium 1.
Counted for 57600 real seconds with 0.09% dead time.

Radionuclide	Activity (Bq)	$R_{l,s} + R_{r,s}$ (s^{-1})	MDA (Bq)	L_D (Bq)	LLQ (Bq)
^{235}U	-(0.10 ± 0.04)	0.198	0.207	0.414	0.621
^{152}Eu	47 ± 2	0.269	0.40	0.79	1.19
^{133}Ba	-(0.08 ± 0.05)	0.075	0.205	0.410	0.614
^{137}Cs	0.09 ± 0.09	0.045	0.205	0.410	0.615

Table 3.06. Activities and Statistics of the Ba eluate from Plutonium 1.
Counted for 17111 real seconds with 0.07% dead time.

Radionuclide	Activity (Bq)	$R_{l,s} + R_{r,s}$ (s^{-1})	MDA (Bq)	L_D (Bq)	LLQ (Bq)
^{235}U	-(0.30 ± 0.03)	0.257	0.40	0.80	1.20
^{152}Eu	0.8 ± 0.2	0.265	0.67	1.34	2.01
^{133}Ba	73 ± 3	0.042	0.273	0.547	0.820
^{137}Cs	-(0.16 ± 0.07)	0.021	0.271	0.542	0.813

Table 3.07. Activities and Statistics of the Cs eluate from Plutonium 1.
Counted for 57600 real seconds with 0.10% dead time.

Radionuclide	Activity (Bq)	$R_{l,s} + R_{r,s}$ (s^{-1})	MDA (Bq)	L_D (Bq)	LLQ (Bq)
^{235}U	0.01 ± 0.05	0.325	0.254	0.508	0.762
^{152}Eu	6.2 ± 0.3	0.327	0.43	0.85	1.28
^{133}Ba	0.21 ± 0.07	0.183	0.293	0.585	0.878
^{137}Cs	163 ± 6	0.040	0.198	0.397	0.595

A composite γ spectrum of all the eluates from the separation of Plutonium 1 is shown in Figure 3.04. The main axis shows photon energies above 500 keV, while the insert shows photon energies below 500 keV.

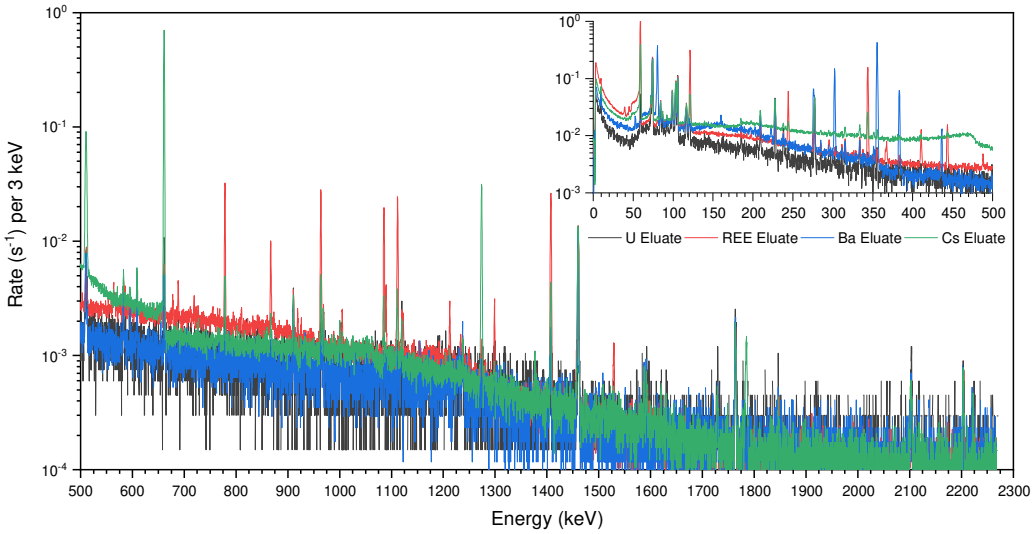

Figure 3.04. Composite Gamma Spectrum of the Plutonium 1 Separations. The γ spectra of all four eluates from the separation of Plutonium 1 are plotted on one figure. The main axis shows photon energies above 500 keV, the insert shows photon energies below 500 keV.

3.2.3 Relative Column Yields

Cs, Ba, and Eu yields were determined in the final fractions by γ spectrometry of the radiotracers added to Plutonium 1 using Equation 3.03, where Y_n is the yield in fraction n, A_n is the activity in fraction n, and A_x is the activity in fraction x.

$$Y_n = \frac{A_n}{A_{x1} + A_{x2} \ldots + A_n} \tag{3.03}$$

U and Pu yields were determined using ICP-MS of the final fractions in Plutonium 1, where activity in Equation 3.03 was replaced with the net response rate. ICP-MS was not used for FP yields because γ spectrometry is a much more sensitive assay for gamma-active radionuclides with short half-lives. For example, an LLQ of 2 Bq ^{137}Cs corresponds to 600 fg ^{137}Cs, well below the LLQ of ICP-MS. The opposite is true for

long-lived radionuclides such as ^{235}U, or radionuclides with low γ-ray transition intensities such as ^{239}Pu or ^{233}U.

3.3 Applied Separations of the Pu Materials

Both Plutonium 1 and Plutonium 4 were separated using the preceding procedures. Plutonium 1 was used to develop the separation scheme, where it was then applied to Plutonium 4 to isolate any trace FPs it may have contained. Therefore, the only radiotracer added to Plutonium 4 was ^{233}U.

3.3.1 Chromatography Yields of Plutonium 1

The overall column scheme used to isolate U and each FP element in Plutonium 1 and Plutonium 4 is detailed in Figure 3.05, along with the reported relative yields of each element. The numbered streams in black text (left of each column) refer to each eluent. The streams in red text (right of or below each column) refer to the corresponding eluates. The first column in Figure 3.05 was performed twice for both Plutonium 1 and Plutonium 4; that is, eluates 1b and 2b underwent two anion exchange (yellow) separations of the same design prior to the cation exchange (orange) and SR resin (gray) columns. The two anion exchange separations were previously discussed in detail in Figure 3.01. Eluates 4a, 4b, and 4c represent all three Pu eluates from Figure 3.01. The anion exchange column was performed twice to maximize the separation factor of Pu from U and the FP elements.

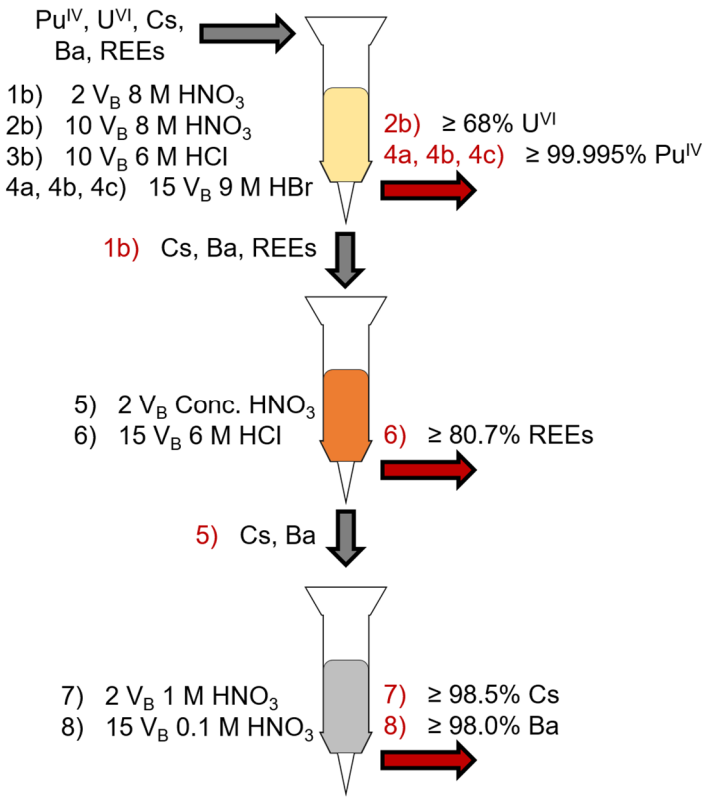

Figure 3.05. Column Chromatography Used to Isolate Trace Fission Products from Separated Pu. The column scheme used to isolate the U and FP fractions from the separated super-grade Pu. Relative column yields are reported next to the relevant eluate stream in red, corresponding to the appropriate eluent stream (of the same number) in black. V_B refers to a volume equal to the bed volume of the resin. The first column used anion exchange resin (yellow), the second cation exchange resin (orange), and the third SR resin (gray). The first column was performed twice for both Plutonium 4 and Plutonium 4. The HCl eluent was used solely to rinse HNO_3 off the column prior to eluting HBr.

The three resulting Pu eluates (4a, 4b, and 4c in Fig. 3) were not assayed directly; the Pu and U content in these eluates was determined to be the mass of Pu and U before chromatography, minus the sum of Pu and U in all other eluates after chromatography. It is well established in literature that Cs, Ba, and the REEs do not adhere to anion exchange resin in eluents 1b and 2b from Figure 3.05 (*147*). Therefore, the activity of ^{137}Cs, ^{133}Ba, and ^{152}Eu in eluates 3a, 3b, and 3c was assumed

to be negligible. This approach assumes that material loss was negligible throughout this procedure. This is a fair assumption as all other eluates were assayed and material was accounted for as appropriate.

The relative column yields of each element are reported for each fraction for Plutonium 1 in Table 3.08. Each fraction in the table is labeled with the corresponding eluate from Figure 3.05. In this table, the MDA, L_D, and LLQ were determined for radiation detection using Equations 3.01 and 3.02 with k as 3.09, 6.18, and 9.27, respectively. The same quantities were determined for mass spectrometry by setting the LLD, L_D, and LLQ as 3.09σ, 6.18σ, and 9.27σ above the background mean, respectively. Values are reported as ≤ MDA, ≤ LD, ≤ LLQ, or ≤ LLQ + 3.09σ as appropriate by Figures 3.02 and 3.03.

The relative yields for Pu in all eluates can be reported with high precision because the LLQ of ^{239}Pu was only 0.4 ng, while the initial mass of Pu was 4.0 mg. The cumulative relative yield of ^{239}Pu in eluates 4a, 4b, and 4c is reported at (99.9954 ± 0.0003)%, indicating a separation factor of approximately 210 for each of the two consecutive anion exchange separations (for either the FP stream or the U stream).

Table 3.08. Relative Column Yields of Each Element by Fraction in Plutonium 1. Fractions are described by element and eluate designation from Figure 3.05.

	Relative Yield (%)				
Fraction (eluate)	Pu	U	REEs	Cs	Ba
Pu (4a, 4b, 4c)	99.9954 ± 0.0003	≥ 25.3	Negligible†	Negligible†	Negligible†
U (2b)	(3.6 ± 0.3) x10-3	≥ 73.8	≤ LLQ	≤ LLQ + 3.09σ	≤ MDA
REE (6)	(2.2 ± 0.2) x10-4	≤ LLQ	≥ 80.7	≤ L_D	≤ MDA
Cs (7)	(5.1 ± 0.5) x10-4	≤ LLQ	≥ 10.2	≥ 98.5	≤ LD
Ba (8)	(2.7 ± 0.2) x10-4	≤ LLQ	≤ LLQ	≤ MDA	≥ 98.0

†These elements are known not to adhere to anion exchange reason to any measurable degree (147)

The relative yields of ^{137}Cs in the Cs fraction (eluate 7) and ^{133}Ba in the Ba fraction (eluate 8) are quite high at ≥ 98.5% and ≥ 98.0%, respectively. These high yields are attributed to the low capacity factors of the two elements in eluents 1 – 5, (*147, 148*) and the low capacity factor of Cs in eluent 6 (*172-174, 195*).The relative yields of ^{233}U in the U fraction (eluate 2) and ^{152}Eu in the REE fraction (eluate 6) were lower at ≥ 73.8% and ≥ 80.7%, respectively. The largest loss of U occurred in eluates 4a and 4c. The relative yield of U in eluate 2b should be improved by using a larger volume in eluents 2a and 2b. The largest loss of ^{152}Eu occurred in eluate 7. The primary cause of this loss is the relatively low capacity factor of the REEs in eluent 5.

Using a smaller volume in eluent 5 would reduce this loss but may not be sufficient to completely elute the Cs and Ba into eluate 5 as designed.

Overall, high yields are reported for each of the elements of interest; the employed separation scheme has proven effective at isolating low masses of both U and these select FP elements out of much larger masses of Pu. The mass of each FP radiotracer was 12.8 ppb, 2.1 ppb, and 2.0 ppb relative to the mass of Pu for ^{137}Cs, ^{152}Eu, and ^{133}Ba, respectively.

3.3.2 Applicability to Larger Samples of Pu

When working with 5 g of Pu, it would be necessary to add an additional large anion exchange separation at the beginning of the process. These larger anion exchange columns have been routinely used to retain and separate large quantities of Pu (up to 4 kg) at Los Alamos for decades (*197*). With an estimated loading of 70 g Pu per liter of resin, the additional 5 g Pu column would need a V_B of at least 75 mL. This additional column would not affect the recovery of the FP elements as they are not retained on anion exchange resin in 8 M HNO_3 to any significant degree (*147*).

Using the separation factor of 210 measured, the mass of Pu that would elute with the U and FPs from this first column would be approximately 25 mg, well within the scope of this work. After this additional column, the procedure reported here may be followed exactly to completion. With three consecutive anion exchange separations, the separation factor measured here can be extrapolated to 9.3×10^6,

which would reduce 5 g of initial Pu to approximately 540 ng of Pu in both the final U and FP eluates.

3.3.3 Trace Fission Product Analysis of Plutonium 4

Eluates 6, 7, and 8 of Plutonium 4 were assayed by ICP-MS to look for trace FP elements in the appropriate streams. The FPs produced by irradiation of U inside a nuclear reactor have exotic isotopic vectors, corresponding to the exact conditions under which the U was irradiated (*44, 51, 53, 54*). As such, any element detected with a natural isotopic vector can be identified as a natural source of the metal, not as a FP. Figure 3.06 reports all potential FP metals found in eluates 6, 7, and 8 in the Plutonium 4 sample, as well as some of their isotope ratios. If a reported isotope ratio agrees with the naturally occurring isotope ratio, then the metal is determined to exist as a natural contaminant, not as a FP (*198*).

All potential FP elements found in Plutonium 4 were identified as natural metal contamination, not as FPs, based on their measured isotope ratios in Figure 3.06. This result is expected since the total mass of Plutonium 4 was only 61.1 mg, where it was expected that a minimum mass of 5 g separated Pu is necessary to contain measurable quantities of the FP elements. However, the chemical methodology applied to Plutonium 4 was able to isolate and concentrate trace levels of natural Cs, Ba, Ce, Nd, and Dy out of a much larger mass of Pu.

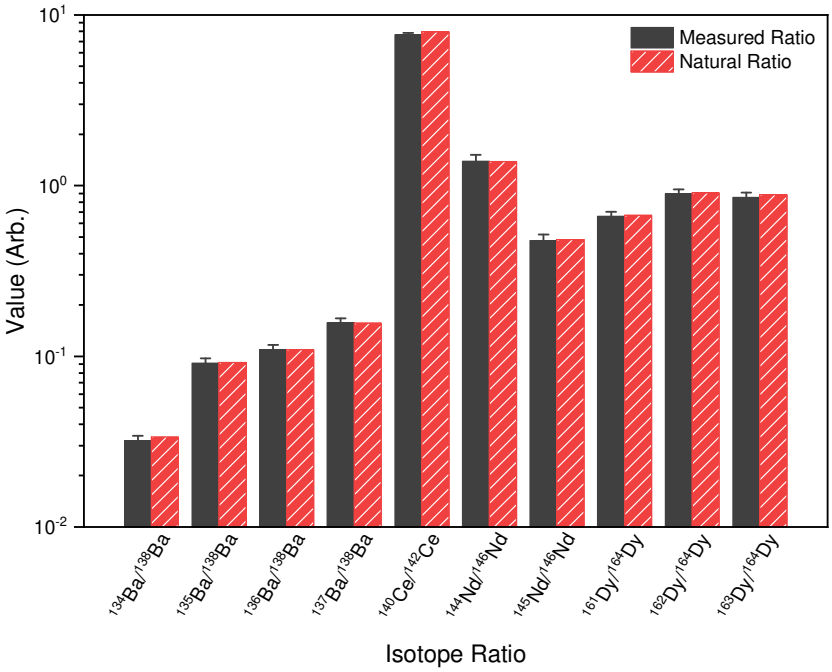

Figure 3.06. Isotope Ratios Measured in Plutonium 4. A comparison of the measured isotope ratios in Plutonium 4 to the natural ratios of each element. Agreement between the measured and natural ratios indicates that the metal is present as contamination, not as a FP.

The masses of these elements and their DFs are reported in Table 3.09. The DF describes how effectively Pu was removed from each element's fraction, as described in Equation 3.04 where *m* is the mass of an analyte, *i* represents the initial ratio, and *f* represents the final ratio.

$$DF = \frac{(m_{Pu}/m_{FP})_i}{(m_{Pu}/m_{FP})_f} \tag{3.04}$$

The Ba, Cs, Ce, Nd, and Dy found in Plutonium 4 were all determined to be natural contaminants (not FPs). These natural metal contaminants may have been introduced in the chemical processing used to initially separate the Pu, or from the

plastic and glassware used to store the sample prior to analysis. The use of sample blanks for ICP-MS indicates that these contaminates were not introduced in the procedure performed here. The large presence of natural Ba in this sample indicates that the $^{136}Ba/^{138}Ba$ isotope ratio of interest may not be suitable for use with the forensic methodology.

Table 3.09 indicates that trace metals present on the order of 10^{-9} g in separated Pu may be sufficiently isolated and assayed via ICP-MS using this chemical methodology. In addition, the radiotracers added to Plutonium 1 (51 pg ^{137}Cs, 8.2 pg ^{152}Eu, 7.8 pg ^{133}Ba, 2.3 μg ^{233}U) were added in trace quantities < 10^{-10} g and were recovered in the appropriate fraction with yields equal to or exceeding 80%. As such, this chemical methodology is capable of isolating trace FPs from bulk Pu material as necessary for the application of the maximum likelihood forensics methodology to 5 g samples of PUREX separated Pu.

Table 3.09. Trace Metal Nuclides Present in Plutonium 4 and Their Decontamination Factors. Elements are grouped together by the assayed fraction from Figure 3.05.

Nuclide	Mass (ng)	DF
^{133}Cs	3.4 ± 0.2	(1.4 ± 0.1)x10^{7}
^{134}Ba	25 ± 2	
^{135}Ba	71 ± 4	
^{136}Ba	85 ± 6	(2.2 ± 0.2)x10^{7}
^{137}Ba	122 ± 7	
^{138}Ba	780 ± 50	
^{140}Ce	410 ± 20	
^{142}Ce	54 ± 2	
^{144}Nd	2.0 ± 0.1	
^{145}Nd	0.67 ± 0.04	
^{146}Nd	1.4 ± 0.1	(2.0 ± 0.2)x10^{6}
^{161}Dy	1.53 ± 0.08	
^{162}Dy	2.1 ± 0.1	
^{163}Dy	2.0 ± 0.1	
^{164}Dy	2.3 ± 0.2	

CHAPTER IV

A FORENSIC INVESTIGATION OF SUPER-GRADE PLUTONIUM ORIGINATING FROM THE MANHATTAN PROJECT

Chapter III used super-grade Pu obtained from LANL to design a chromatographic separation which could be used to apply the maximum likelihood forensic methodology to samples of separated Pu of at least 5 g. Here, the resulting Pu and U fractions from those separations were used as part of a traditional forensics investigation to discriminate the history of those same samples of super-grade Pu at LANL.

Pu was first produced in late 1940 by irradiating ^{238}U with deuterons and neutrons at the 60 in. cyclotron in Berkeley, California by Glenn T. Seaborg and others (*108, 109*). A sample of this cyclotron-produced Pu is on display at the Smithsonian Institution in Washington, DC and represents the oldest samples of Pu created by humankind (*12*). Although the cyclotron production method led to the discovery of Pu, it could only produce microgram quantities of the special nuclear material (SNM). The chemists and physicists in the Manhattan Project quickly learned that they needed gram quantities of the element to fully uncover its nature (*107, 110*), so a Pu production pilot plant was built and designated as X-10 at the Clinton Engineering Works in Oak Ridge, Tennessee; the reactor went critical for the first time in November of 1943 (*107, 199*). Commonly referred to as the "Clinton Pile," this nuclear reactor had two primary missions – to act as a prototype for the Pu

production reactors to be built at Hanford, Washington, and to produce gram quantities of Pu for the first time (*199*). Pu is produced in a nuclear reactor from successive neutron captures and β- decays in the U fuel. The Pu produced at X-10 during this time was primarily referred to as Clinton Pu, but was also called "Pu from X," "X-Pu," or "Pile Pu." (*107, 110, 200-203*) Many reports from the Manhattan Project have been declassified and approved for public release. These publicly available reports do not exactly indicate when the first samples of Clinton Pu were shipped from X-10 to Los Alamos; however, some reports can be used to infer that the first small samples of Clinton Pu were shipped to Los Alamos in January of 1944, and only grams of Pu had been received by March 1944 (*107, 110, 199, 200, 204, 205*).

In this chapter, multiple techniques in the field of forensics were used to discriminate and confirm the origin of four samples labeled as "Clinton Pu" at LANL. The four samples of Pu in question were identified only by their labels; there existed no supporting information or documentation to confirm the origin or identity of the samples at the time of assay. As such, they presented themselves as an ideal opportunity to apply forensic techniques to discriminate the origin of unknown weapons-usable Pu.

4.1 Experimental Methods

4.1.1 Reagents

The ^{233}U radiotracer was obtained as legacy material from LANL with a measured isotopic vector of 76.92% ^{233}U, 0.82% ^{234}U, 0.088% ^{235}U, and 22.17% ^{238}U. Radiotracers are added to a sample at the start of a process to determine the process

yield. All acids used were purchased in the concentrated form as Optima grade from Fisher Scientific. The anion exchange resin was purchased as AG MP-1 from Bio-Rad. $NaNO_2$ was purchased as 99.999% trace metal grade from Sigma Aldrich. The 3 and 20 mL columns were purchased from Evergreen. The U inductively coupled plasma mass spectrometry (ICP-MS) calibration standard was purchased from Inorganic Ventures as 100 ppm U in 2% HNO_3 (v/v). The U500 isotope standard was obtained from New Brunswick Laboratory (NBL) with a certified U isotopic vector of 0.5181% ^{234}U, 49.696% ^{235}U, 0.0755% ^{236}U, and 49.711% ^{238}U in 2% HNO_3 (v/v).

The four samples of Pu were identified in a steel canister labeled "Clinton Pu" as seen in Figure 4.01A. The unknown samples are hereafter designated as Plutonium 1 – 4. The labeling on the steel canister disclosed the supposed masses of the samples contained within: 20 mg (divided between Plutonium 1 and 2, Figure 4.01B), 15.9 mg (Plutonium 3, Figure 4.01C), and 280 mg (Plutonium 4, Figure 4.01D). The steel canister indicated that Plutonium 3 and 4 were stored as PuO_2; the forms of Plutonium 1 and 2 were undisclosed. The samples labeled as "Plutonium 1" and "Plutonium 4" from Chapter III are the same samples discussed with the same name here.

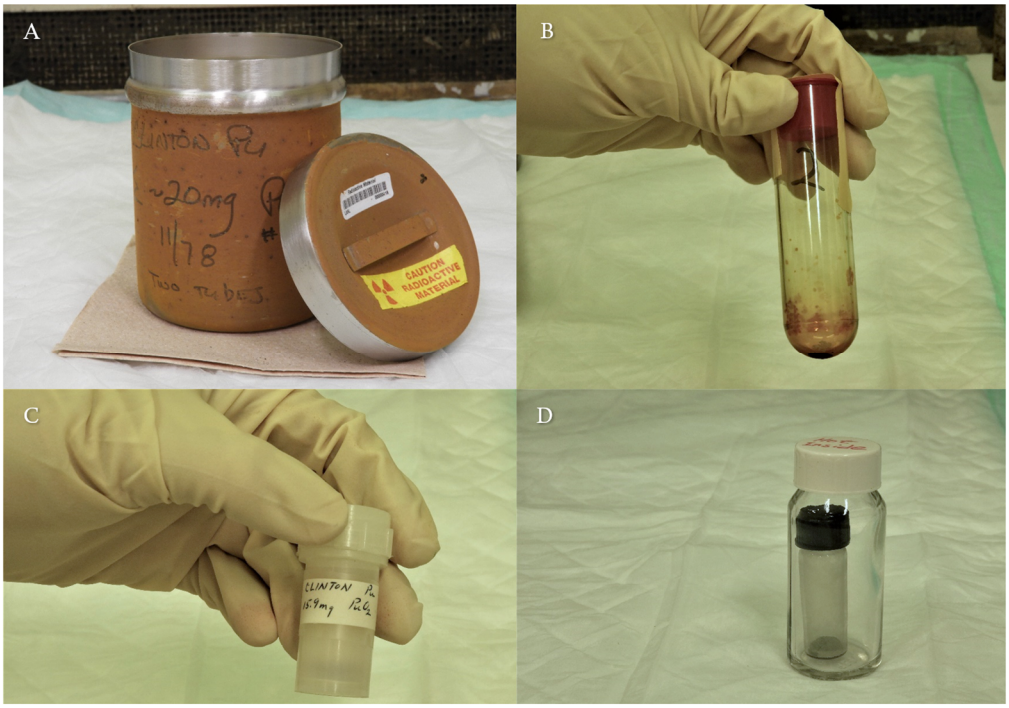

Figure 4.01. Four Samples of "Clinton Pu" Identified at Los Alamos National Laboratory. The steel canister (**A**) which contained four samples of Pu labeled as Clinton Pu: Plutonium 2 (**B**), Plutonium 3 (**C**), and Plutonium 4 (**D**). Plutonium 1 was contained in a tube remarkably similar to Plutonium 2 (**B**).

4.1.2 Dissolution and Separation

Plutonium 1 and 2 were identified as white crystals and dissolved readily in 8 M HNO_3 producing a dark green solution. Plutonium 4 was identified as a green powder and was dissolved over several hours in concentrated HCl producing a dark red solution. Contrarily, Plutonium 3 was identified as a dark powder and could only be dissolved in an aggressive acid solution of concentrated 15:1 HNO_3:HF over four days. This solution was colorless until the complete evaporation of HF, at which point it turned dark green. An aliquot of Plutonium 3 was taken for forensic analysis prior

to its complete dissolution; the entirety of the Plutonium 3 sample after complete dissolution was not investigated here.

Plutonium 1 and Plutonium 4 were separated following the same procedure discussed in Section 3.1.6. In general, multiple ion exchange and extraction chromatographies were performed to isolate Pu, U, Am/REEs, Cs, and Ba into their own fractions. Plutonium 2 and Plutonium 3 initially followed the same procedure to isolate Pu and U, but the cation exchange and SR resin separations were not performed. It was already determined that these materials did not contain measurable quantities of FPs (Section 3.3.3), so it was not necessary to isolate each FP into its own fraction. The ^{233}U radiotracer was added to all four samples to determine the yield of the U fractions. The ^{133}Ba, ^{137}Cs, and ^{152}Eu radiotracers were only added to Plutonium 1.

4.1.3 Radiation Detection

Gamma spectrometry was performed using a Canberra Standard Electrode Coaxial high-purity germanium (HPGe) detector calibrated against a NIST-traceable ^{152}Eu source for energy and efficiency. Spectra were collected with a geometry of 1 mL solution volume at a distance of 9 cm from the detector face. A 0.01% aliquot of the Pu samples were taken for gamma assay prior to chemical separation. This was the largest fraction of the unseparated materials that could be transferred to the counting area per safety protocols. The U and Am fractions obtained after chemical separation met the requirements for material transfer without any further dilution.

Therefore, 100% of the U and Am fractions were assayed at 9 cm from the HPGe detector face for all four samples.

Alpha spectrometry was performed using a Canberra passivated implanted planar silicon (PIPS) detector in a model 7401 single channel alpha spectrometer with a Multiport II MCA calibrated against a NIST-traceable "four-peak" calibration source containing ^{148}Gd, ^{239,240}Pu, ^{241}Am, and ^{244}Cm for energy and efficiency. Aliquots were diluted by a total factor of 10^6 after chemical separation and spectra were collected with a geometry of 50 µL solution evaporated onto a stainless steel planchet with a diameter of 2 mm at a distance of approximately 3 cm below the detector face. Samples were not electrodeposited for alpha spectrometry to avoid adding Pu radiotracers to the samples. The evaporated samples produced a sufficiently small full width at half-maximum (FWHM) at the principal ^{239,240}Pu peak of approximately 30 keV.

4.1.4 Mass Spectrometry

ICP-MS was performed with a Thermo Fisher Scientific iCAP RQ mass spectrometer. All solutions were diluted up to 10 mL with 2% HNO_3 (v/v) prior to assay. All 2% HNO_3 used here was prepared as 2% by volume. Blanks and sample blanks were assayed to determine the background rates and the lower limit of quantification (LLQ) for each mass bin of each sample. The LLQ was set at 10 standard deviations above the blank mean. The U500 isotope standard from NBL was used to correct for mass bias measured in the U isotopes. Hydride and tailing

corrections were performed for ^{239,240}Pu and ^{233,234,235,236}U on an individual basis. The typical hydride formation fraction was approximately 0.0092%.

The presence of ^{233}U in the U fraction was assumed to originate exclusively from the ^{233}U radiotracer added. To support this assumption, no ^{233}U was detected in the unseparated Pu sample prior to adding the radiotracer, and ^{233}U is not a naturally occurring isotope of U. The intensity of ^{233}U and its known isotopic vector was used to determine its contribution to the 234, 235, 236, and 238 mass bins of the U fraction of each sample and corrections were made as appropriate. The ratio of ^{235}U/^{238}U in the U fraction was greater than 300, indicating no significant presence of natural ^{235,234}U in the sample. This follows because the mass ratio of ^{235}U/^{238}U and ^{234}U/^{238}U in ^{nat}U is 7.3×10^{-3} and 5.4×10^{-5}, respectively (*198*); therefore, a small fractional contribution of ^{238}U from natural sources must carry with it a negligible contribution of natural ^{235,234}U. Each replicate measurement was prepared individually for assay by ICP-MS, but the overall chemical separation was only performed once as described.

4.1.5 Reactor Modeling

Reactor models for the 1 MW and 4 MW power levels of the X-10 reactor and the resulting simulations were provided by my colleague Patrick J. Oneal. The results of these models are necessary to describe the entire discrimination process, so details about the reactor models are included here. A depletion calculation for a fuel slug in the X-10 graphite reactor was performed to verify that the isotopic ratios of the unknown Pu samples were consistent with their suspected origin from the X-10

reactor. This calculation was performed using a model made with the Monte Carlo N-Particle (MCNP6) transport code (*184*). The model consisted of a single ^{nat}U fuel slug within a square air channel, surrounded by graphite moderator. The fuel slug was clad in Al of thickness 0.09 cm and the slug's radius and length were 1.51 cm and 10.48 cm, respectively. The fuel slug was modeled with a total weight of 1.175 kg U.

The fuel channel was contained in a graphite lattice square of side length 60.96 cm. The boundaries of the graphite lattice square and the two end faces of the fuel slug were modeled with reflective boundary conditions in order to emulate the fuel slug being located in the interior of a central fuel channel. The first simulation was run to a total fuel burnup of 9.58 MWd/MTU at a power level of 1 MW with a total fuel loading of 29,835 slugs using reflective boundaries. The second simulation was run to a total fuel burnup of 10.72 MWd/MTU at a power level of 4 MW with a total fuel loading of 40,000 slugs using reflective boundaries (*199, 206, 207*).

4.2 Initial Characterizations

4.2.1 Radiopurity and Pu Isotopics

No radionuclides other than $^{239,240}Pu$ were identified in any of the samples via radiation detection prior to chemical separation. After chemical separation, ^{235}U and ^{241}Am were detectable by gamma spectrometry in the largest sample, Plutonium 4; ^{238}Pu remained below the LLQ of the alpha spectrometer for all four samples. Alpha and gamma spectra of Plutonium 4 after separation are shown in Figures 4.02 and 4.03. ^{239}Pu and ^{240}Pu cannot be resolved using typical commercial alpha spectrometers and are identified together.

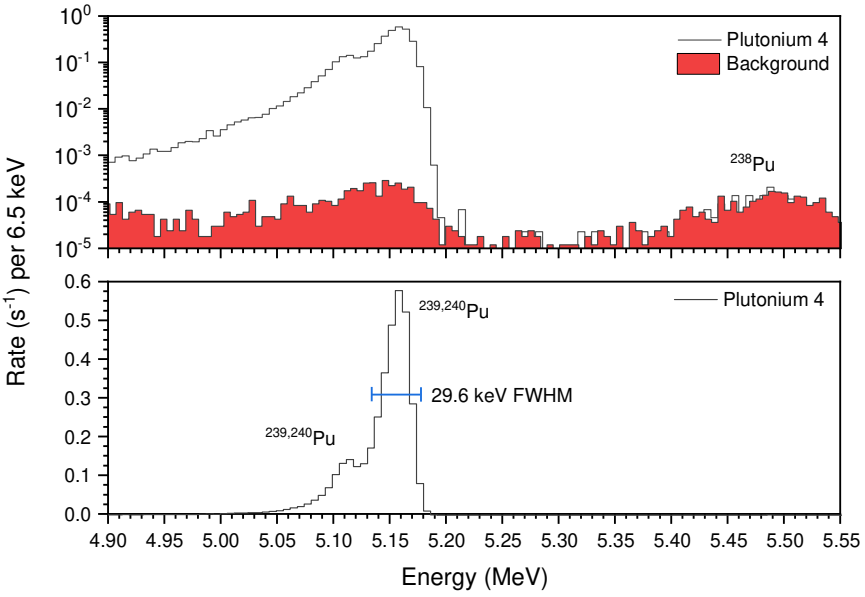

Figure 4.02. Alpha Spectrometry of Plutonium 4. Alpha spectrum of Plutonium 4 between 4.90 – 5.55 MeV after chemical separation on both logarithmic and linear scales. The activity of ^{238}Pu is shown to be below the detection limit of the spectrometer used.

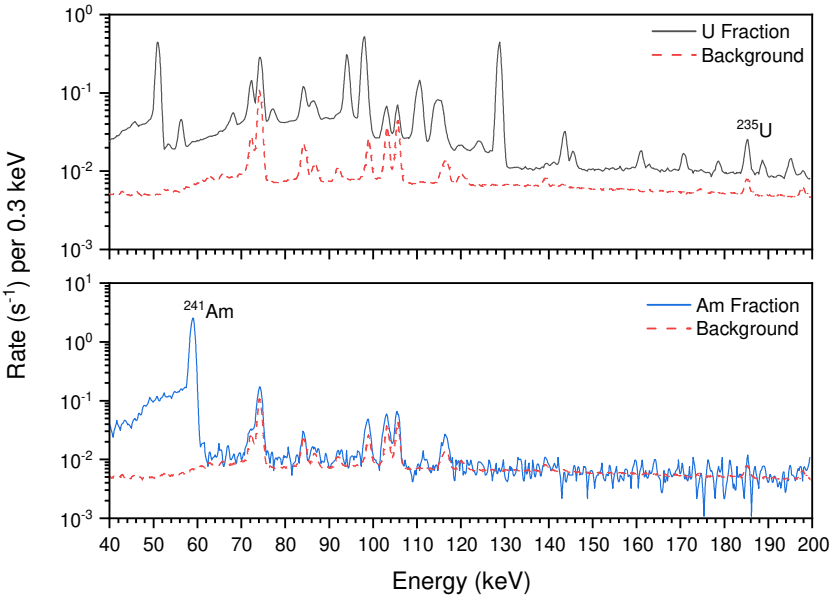

Figure 4.03. Gamma Spectrometry of Plutonium 4. Gamma spectra of the U (top) and Am (bottom) fractions after separation of the Plutonium 4 sample.

The mass of Pu was assayed via alpha spectrometry as 4.02 ± 0.05, 4.04 ± 0.05, and 61.1 ± 0.8 mg for Plutonium 1, 2, and 4 with their 1σ uncertainties, respectively. These masses differ significantly from the labeling on the original steel canister from Figure 4.01A, indicating that material was taken from each sample after their initial containment. The mass of the partial Plutonium 3 aliquot taken was 4.74 ± 0.06 mg. The rest of the Plutonium 3 sample was not assayed here.

The only Pu isotopes which could be assayed directly in any of the four samples were ^{239}Pu and ^{240}Pu. The ^{238,241,242}Pu isotopes were below the LLQ of the ICP-MS and alpha spectrometer used. The isotopics of the four Pu samples are listed in Table 4.01 as measured by ICP-MS with their 1σ uncertainty. These results are consistent for Pu originating from the X-10 reactor, which was known to discharge Clinton Pu at > 99.9% ^{239}Pu (*12, 201-203*).

4.3 Chronometry

Ideally, there exist four chronometers which may be reliably used to determine the chronometric age of Pu: ^{238}Pu – ^{234}U, ^{239}Pu – ^{235}U, ^{240}Pu – ^{236}U, and ^{241}Pu – ^{241}Am. In order to use these chronometers to determine the time since last purification, an analysis must be sensitive to the trace masses of these Pu isotopes and their decay daughters; additionally, there must be relatively high confidence that the purification process completely separated the parent-daughter pairs. In the literature, these Pu chronometers have been routinely used to determine the time since last separation for various unknown and standardized samples of Pu (*9, 10, 26, 32, 33, 182*).

Table 4.01. Isotopics of the Four Pu Samples with their 1σ Uncertainties Compared to Known Samples of Clinton Pu.

Sample	$^{240}Pu/^{239}Pu$ (10^{-4})	^{239}Pu Abundance (%)
Plutonium 1	4.6 ± 0.3	99.954 ± 0.003
Plutonium 2	4.5 ± 0.2	99.955 ± 0.002
Plutonium 3	4.4 ± 0.3	99.956 ± 0.003
Plutonium 4	4.4 ± 0.2	99.953 ± 0.002
Clinton Pu 1†	3.3 ± 0.6	99.967 ± 0.006
Clinton Pu 2‡	3.8 ± 0.1	99.962 ± 0.001

†Bartlett, 1944 – 1946 (*201-203*)
‡Schwantes, 2009 (*12*)

The four samples of Pu investigated here are isotopically too pure to use the ^{238}Pu – ^{234}U or ^{241}Pu – ^{241}Am chronometers directly; there does not exist a high enough activity of $^{238,241}Pu$ to measure by alpha or mass spectrometry. Instead, the ^{239}Pu – ^{235}U and ^{240}Pu – ^{236}U chronometers were measured in multiple ways for each sample and averaged to produce chronometric ages with high confidence. In all four samples, the ^{239}Pu – ^{235}U and ^{240}Pu – ^{236}U chronometers were measured via mass spectrometry of the U fraction after chemical separation. The yield of the U fraction was determined for each sample using the ^{233}U radiotracer initially added. The ^{239}Pu – ^{235}U chronometer was also measured in all four samples via mass spectrometry of the aliquots taken prior to any chemical separation. This procedure ensured at least three measurements for the chronometric age of all four samples.

The ^{239}Pu – ^{235}U chronometer was also measured after separation via gamma spectrometry in Plutonium 4. This was possible because Plutonium 4 was significantly larger in mass than the other three samples, resulting in a measurable activity of ^{235}U via gamma spectrometry.

The measured activities of each radionuclide used for chronometry are listed in Tables 4.02 and 4.03 with their 1σ uncertainties. The activities of the Plutonium 1, 2, and 3 chronometers were measured only once, while the activities of the Plutonium 4 chronometers were measured 18, 15, and 11 times each for ^{235}U, ^{236}U, and ^{234}U, respectively. Chronometric age was determined using the Bateman solution in Equation 1.39 (Section 1.3.2). Chronometric ages are dated as of assay on October 16, 2019.

The average chronometers are reported as measured for Plutonium 1, 2, and 4 in Figure 4.04. Chronometry of Plutonium 3 is discussed at the end of this section. The error bars represent the 1σ uncertainty for Plutonium 1 and 2, and the 95% CI for Plutonium 4. Plutonium 4 was the only sample remeasured multiple times (N = 33), so it is the only case where a 95% CI may be reported. The horizontal red lines represent the earliest time that reactor-produced Pu was shipped from X-10 to Los Alamos, between January – March 1944 (*199*).

Table 4.02. Measured Activities of the U Isotopes in the Pu Samples as of October 2019. All uncertainties represent the 1σ standard deviation.

	Activity (Bq)			
Isotope	Plutonium 1	Plutonium 2	Plutonium 3	Plutonium 4
^{234}U	< LLQ	< LLQ	< LLQ	3.2 ± 0.2
^{235}U	0.63 ± 0.02	0.66 ± 0.02	1.11 ± 0.02	10.5 ± 0.26
^{236}U	0.027 ± 0.001	0.032 ± 0.001	0.050 ± 0.003	0.51 ± 0.03

Table 4.03. Measured Activities of the Pu Isotopes in the Pu Samples as of October 2019. All uncertainties represent the 1σ standard deviation.

	Activity (Bq)			
Isotope	Plutonium 1	Plutonium 2	Plutonium 3	Plutonium 4
^{239}Pu	(9.2 ± 0.1)x10^6	(9.3 ± 0.1)x10^6	(1.09 ± 0.01)x10^7	(1.40 ± 0.02)x10^8
^{240}Pu	(1.57 ± 0.09)x10^4	(1.54 ± 0.05)x10^4	(1.76 ± 0.09)x10^4	(2.29 ± 0.09)x10^5

Plutonium 1 was determined to be last chemically separated in April 1954 ± 24 months (66 ± 2 y) at 1σ uncertainty. This was the youngest chronometer measured of all four samples. The Plutonium 2 chronometer was slightly older with a measured date of December 1947 ± 22 months (72 ± 2 y) at 1σ uncertainty. The average chronometer for the 61.1 mg Plutonium 4 sample aligns exactly with the

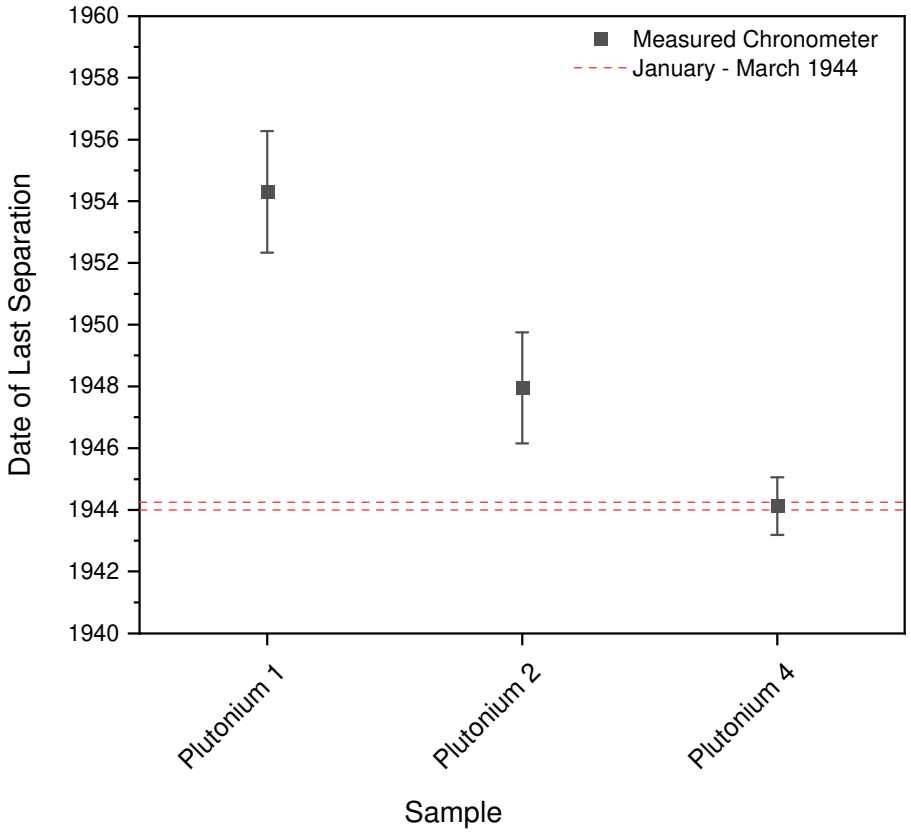

Figure 4.04. Chronometry of the Undocumented Pu. Average chronometric ages of Plutonium 1, 2, and 4. The error bars represent the 1σ uncertainty for Plutonium 1 and 2, and the 95% CI for Plutonium 4. The horizontal red lines indicate the earliest time any reactor-produced Pu was shipped to Los Alamos. Chronometry of Plutonium 3 was not included here because of its impossible date, as discussed in the text.

earliest samples of Clinton Pu that were shipped to Los Alamos, measured as February 1944 ± 11 months (75.7 ± 0.9 y) at the 95% CI.

The Plutonium 3 chronometer is not reported in Figure 4.04 because its measured chronometer was impossible, dated to the year 1918. It is most likely that this happened because the aliquot of Plutonium 3 assayed here was taken prior to complete dissolution of the initial PuO_2 material; it is hypothesized that the U within

the sample dissolved faster than the bulk PuO_2, resulting in significant fractionation between the U/Pu content in the withdrawn aliquot. This hypothesis is supported by the faster rate at which UO_2 is known to dissolve in HNO_3 compared to "high-fired" PuO_2 (*208, 209*). High-fired PuO_2 refers to any PuO_2 calcined at temperatures over 800 °C, which is infamously slow to dissolve (*208, 209*), similar to what was observed for the Plutonium 3 sample.

4.4 Reactor-Type Discrimination

Pu isotope ratios have been routinely used in the literature to discriminate the reactor origin of Pu produced from high fuel burnups (*9-12, 53-56, 58*). In general, different types of nuclear reactors produce different Pu isotope ratios as a function of fuel burnup. These studies typically plot three Pu isotope ratios in 3-dimensional space to produce several curves which are spatially resolved by reactor type. If a measured set of Pu isotope ratios fall on any given curve, it is taken as a strong indication that the Pu originated from the respective reactor type.

The X-10 reactor was modeled at power levels of 1 and 4 MW based on publicly available specifications and burned using the Monte Carlo radiation transport code MCNP6 by Patrick J. Oneal, as discussed in Section 4.1.5. The X-10 reactor was known to operate at 1 MW with approximately 35 metric tons of U in the period between November 1943 – May 1944, and at 4 MW with approximately 47 metric tons of U after July 1944 (*199, 206, 207*). The reactor was "burned" up to 9.58 and 10.72 MWd/MTU for the 1 and 4 MW models respectively. Pu production is reported as a function of fuel burnup for each model in Figure 4.05.

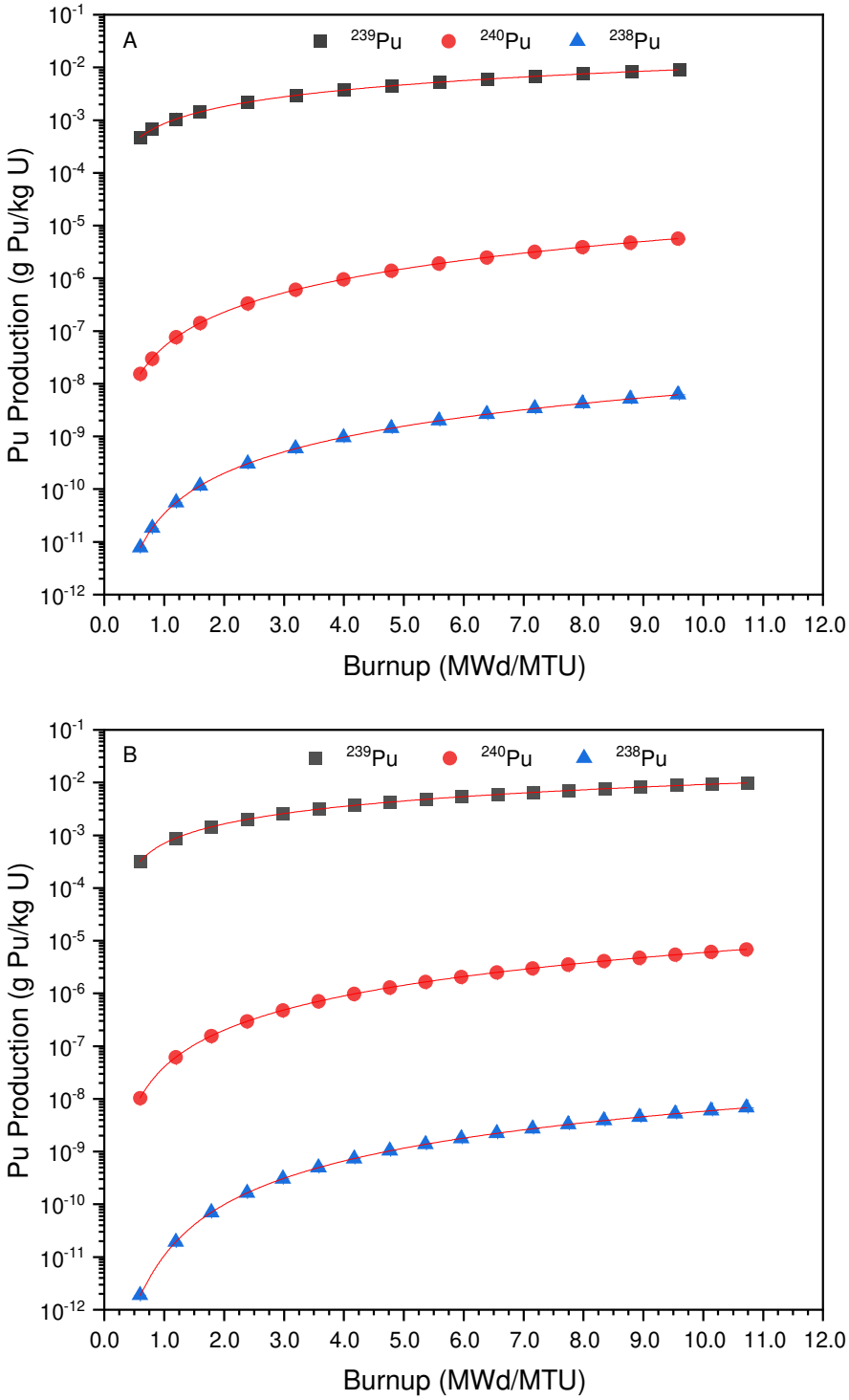

Figure 4.05. Pu Production from the 1 and 4 MW X-10 Reactor Models. Pu production as a function of burnup from both the 1 (**A**) and 4 (**B**) MW X-10 reactor models. The simulated production rates were fit for interpolation using Originlab 2020 (red lines).

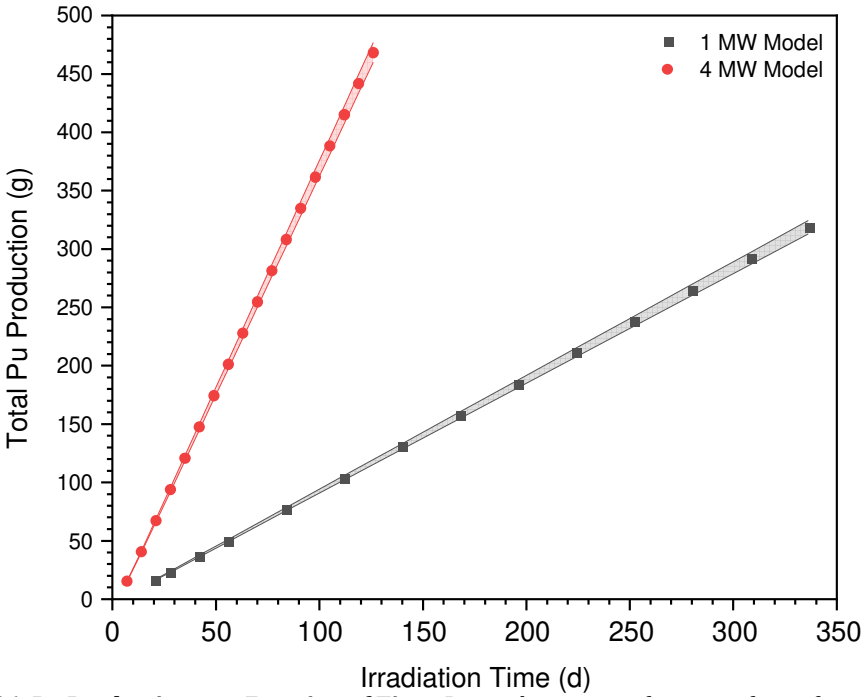

Figure 4.06. Pu Production as a Function of Time. Pu production as a function of time from both the 1 and 4 MW X-10 reactor models. Error bands represent the 1σ uncertainty.

Pu production from the X-10 reactor models is also tabulated in Tables 4.04 and 4.05 and reported as a function of time in Figure 4.06. The linear trends in this figure can be used to estimate that the X-10 reactor discharged approximately 200 g of Clinton Pu during its 1 MW operating period, and approximately 1 kg of Clinton Pu during its 4 MW operating period.

Although ^{238}Pu could not be assayed directly in any of the four Pu samples, its decay daughter ^{234}U was quantified in the U fraction of Plutonium 4 by mass spectrometry as reported in Table 4.02. The masses of the other three Pu samples were too low to identify or quantify ^{234}U in their U fractions. Using its previously

measured chronometric age, Eq. 1.44 (Section 1.3.2) was re-solved to determine the initial mass of ^{238}Pu that must have existed in Plutonium 4 at the moment of purification in 1944.

Table 4.04. Tabulated Pu Production from the 1 MW X-10 Reactor Model with 1σ Uncertainties.

Time (d)	Burnup (MWd/MTU)	^{238}Pu (pg/kg U)	^{239}Pu (μg/kg U)	^{240}Pu (ng/kg U)
21	0.60	7.8 ± 0.4	479 ± 9	15.4 ± 0.3
28	0.80	18.3 ± 0.8	670 ± 10	30.0 ± 0.6
42	1.20	56 ± 3	1050 ± 20	76 ± 2
56	1.60	116 ± 5	1440 ± 30	143 ± 3
84	2.40	310 ± 10	2200 ± 40	335 ± 7
112	3.19	590 ± 30	2970 ± 50	610 ± 10
140	3.99	960 ± 40	3730 ± 70	960 ± 20
168	4.79	1430 ± 60	4500 ± 80	1390 ± 30
196	5.59	1990 ± 90	5300 ± 100	1910 ± 40
224	6.39	2600 ± 100	6000 ± 100	2500 ± 50
252	7.19	3400 ± 200	6800 ± 100	3170 ± 70
280	7.98	4200 ± 200	7600 ± 100	3920 ± 80
308	8.78	5200 ± 200	8300 ± 200	4800 ± 100
336	9.58	6200 ± 300	9100 ± 200	5700 ± 100

Table 4.05. Tabulated Pu Production from the 4 MW X-10 Reactor Model with 1σ Uncertainties.

Time (d)	Burnup (MWd/MTU)	^{238}Pu (pg/kg U)	^{239}Pu (μg/kg U)	^{240}Pu (ng/kg U)
7	0.60	1.88 ± 0.08	325 ± 6	10.4 ± 0.2
14	1.19	19.3 ± 0.9	870 ± 20	62 ± 1
21	1.79	71 ± 3	1430 ± 30	157 ± 3
28	2.38	164 ± 7	2000 ± 40	296 ± 6
35	2.98	310 ± 10	2570 ± 50	480 ± 10
42	3.58	500 ± 20	3140 ± 60	710 ± 20
49	4.17	740 ± 30	3710 ± 70	980 ± 20
56	4.77	1030 ± 50	4280 ± 80	1300 ± 30
63	5.36	1380 ± 60	4850 ± 90	1660 ± 30
70	5.96	1770 ± 80	5400 ± 100	2070 ± 40
77	6.55	2200 ± 100	6000 ± 100	2520 ± 50
84	7.15	2700 ± 100	6600 ± 100	3010 ± 60
91	7.75	3300 ± 200	7100 ± 100	3550 ± 70
98	8.34	3900 ± 200	7700 ± 100	4130 ± 90
105	8.94	4500 ± 200	8300 ± 200	4800 ± 100
112	9.53	5200 ± 200	8800 ± 200	5400 ± 100
119	10.13	6000 ± 300	9400 ± 200	6100 ± 100
126	10.72	6800 ± 300	10000 ± 200	6900 ± 100

Table 4.06. Measured Isotope Ratios in Plutonium 4 and their 1σ Uncertainties.

Isotope Ratio	Value
$^{240}Pu/^{239}Pu$	$(4.4 \pm 0.2)x10^{-4}$
$^{238}Pu/^{239}Pu$	$(5.2 \pm 0.3)x10^{-7}$
$^{238}Pu/^{240}Pu$	$(1.17 \pm 0.09)x10^{-3}$

The Pu isotope ratios measured in Plutonium 4 are reported in Table 4.06 with their 1σ uncertainties. The ratios were measured a total of 12, 11, and 11 times each for $^{240}Pu/^{239}Pu$, $^{238}Pu/^{239}Pu$, and $^{238}Pu/^{240}Pu$, respectively. The $^{238}Pu/^{239}Pu$, $^{240}Pu/^{239}Pu$, and $^{238}Pu/^{240}Pu$ isotope ratios are plotted as a function of fuel burnup in Figure 4.07 as estimated by the 1 and 4 MW X-10 reactor models burned in MCNP6. Errors in the MCNP simulations are reported by error bands expanded to the range of 2σ and were estimated using the errors of the relevant thermal neutron capture cross sections and the stochastic errors from the reaction rates as reported by MCNP. The experimentally measured isotope ratios of Plutonium 4 are plotted as a black sphere with error bars representing the range of the 95% CI.

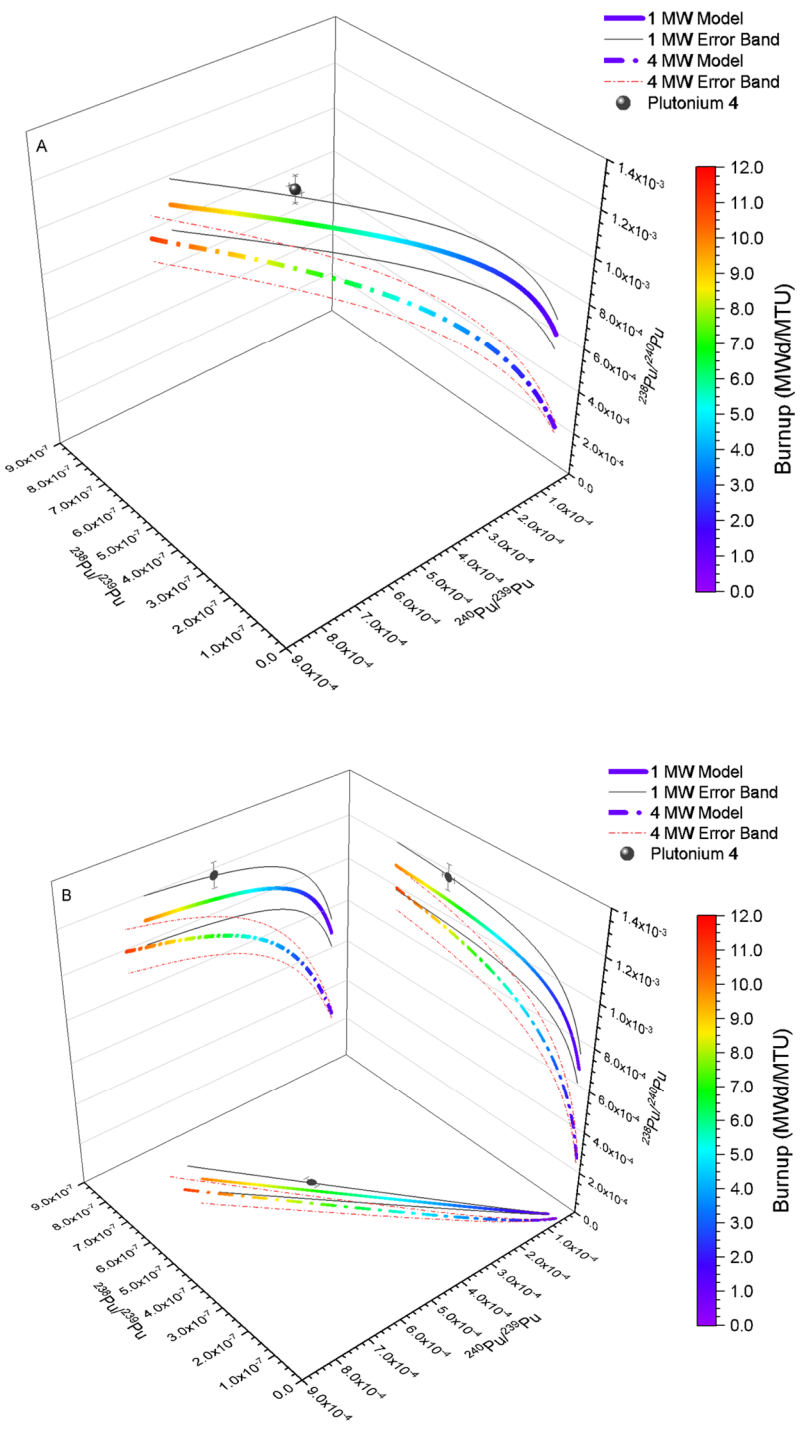

Figure 4.07. Reactor Discrimination of Plutonium 4. (**A**): Pu isotope ratios as a function of burnup from the 1 and 4 MW X-10 reactor models compared to Plutonium 4. (**B**): The same information is projected onto the three spatial planes to provide a different representation of the position of Plutonium 4 in relation to the reactor models. The Plutonium 4 error bars represent the range of the 95% confidence interval, while the model error bands are expanded to cover the range of 2σ.

Initial inspection of Figure 4.07A indicates that the measured isotopics of Plutonium 4 are consistent with discharge from the X-10 reactor. Closer inspection of the projections in Figure 4.07B shows that the measured isotopics of Plutonium 4 overlap significantly with the 1 MW model on all three projections but do not overlap with the 4 MW model on any projection. This indicates that the measured isotopics of Plutonium 4 are more consistent with discharge from the 1 MW reactor model, which was known to operate from November 1943 – May 1944. This result is consistent with the chronometer measured in Figure 4.04 indicating separation in early 1944.

Fuel burnup at discharge was estimated by determining the point of closest approach between the centroid of the measured Pu isotopics and the centroid of the 1 MW model curve from Figure 4.07A. The point of closest approach was determined as the minimum distance between the measured ratios and the model curve, calculated using the standard distance formula. This distance is reported in Figure 4.08 as a function of burnup. The point of closest approach occurred at a model burnup of 7 ± 2 MWd/MTU. The error in burnup was estimated by setting the range of its 1σ uncertainty equal to the highest and lowest burnups within 1σ uncertainty of closest approach. This may be visualized using Figure 4.08 by drawing a line tangential to the upper error band at closest approach. The two points where this tangent line intersects the distance line sets the bounds of the 1σ uncertainty in the burnup measurement.

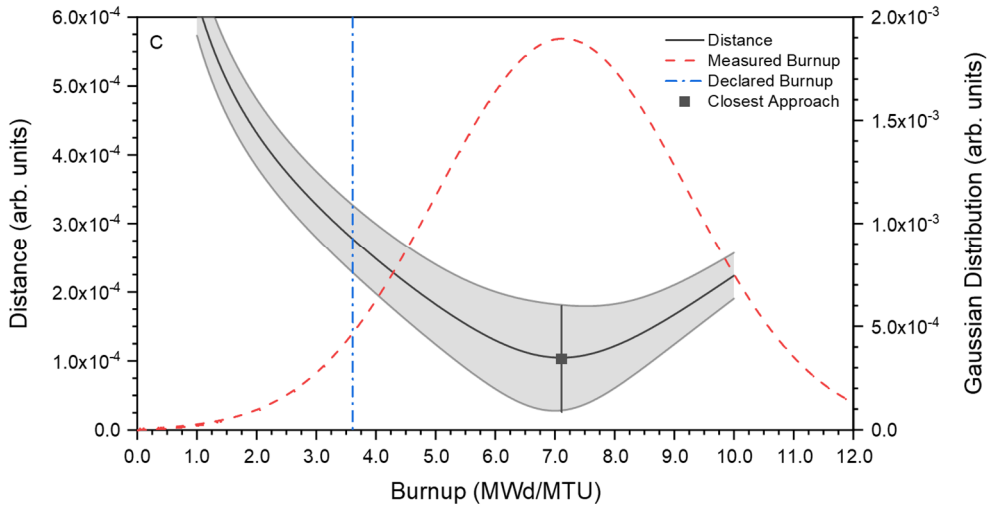

Figure 4.08. Closest Approach Approximation of the 1 MW Reactor Model. The distance between the measured Pu isotope ratios and the 1 MW model curve as a function of burnup (left axis). The point of closest approach and its 1σ error are represented by the square point. The Gaussian distribution of the measured burnup (red line, right axis) is compared to the declared burnup (blue line).

The declared fuel burnup of 3.6 MWd/MTU for the X-10 reactor is shown as a vertical line without error in Figure 4.08; however, it is noted that the technique used to measure burnup in the X-10 reactor may have been prone to error (*12*). At the time, reactor operators monitored burnup by measuring the temperature of the cooling gas as it left the reactor core (*12*). Such a measurement may not accurately reflect the burnup of each individual fuel channel within the core. Thus, the measured burnup reported here is considered to be in general agreement with the declared burnup from the X-10 reactor. Table 4.03 indicates it would take between 175 – 323 d to produce fuel at a burnup between 5.0 – 9.2 MWd/MTU (the 1σ range of estimated burnup) during the 1 MW operation period. This is consistent with the known operation period of approximately 211 d for the 1 MW power level.

4.5 Trace Metal Analysis

The Clinton Pu produced at X-10 was purified through the bismuth phosphate process in large batches prior to shipment to Los Alamos (*110, 199*). Some of the metals commonly associated with this process include Bi, La, and Ce, along with some of the lighter d-block elements such as Fe and Zr (*12*). After arrival at Los Alamos, it was realized that the Clinton Pu required further decontamination before it was suitable for use in weapons research and development (*110, 111*). The adopted solution to this problem was reported in May 1944 and was first performed on milligrams of Clinton Pu as early as March 1944 (*111*). Although the final Pu product met the required purity specifications, multiple lots of Clinton Pu were indicated to possess trace Li, Be, Na, Mg, Al, Ca, and Th in addition to all of the previously discussed metal impurities.

The four Plutonium samples investigated here were assayed for trace metals using ICP-MS before and after chemical separation, as reported in Figure 4.09. For most elements assayed, a positive identification was only made if a metal's isotope ratios matched the natural values. In all cases where an isotope ratio did not agree with the natural value, an interfering isobar was always identified, and corrections were made. No FPs were identified in any of the four Pu samples. Positive identification of monoisotopic elements was only made if no possible isobaric interference existed for the given mass bin.

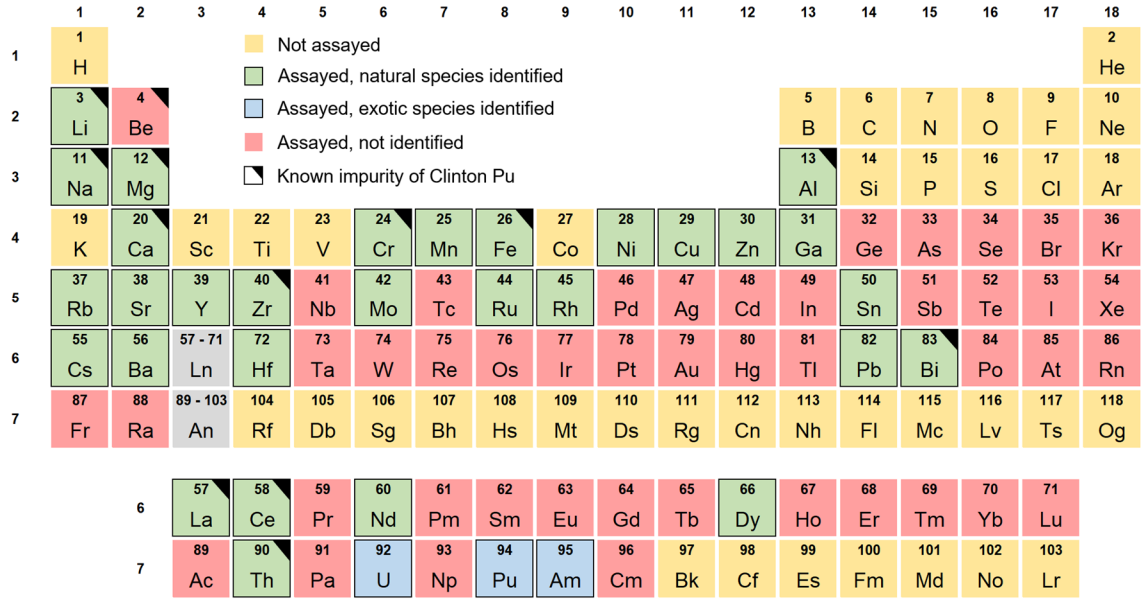

Figure 4.09. Trace Metal Analysis of Plutonium 4. This periodic table has been color-mapped to the identification of various trace metals in the four Pu samples. Positively identified elements (natural or exotic) are also indicated with a border for grayscale viewing. Metals which are known impurities in Clinton Pu have been earmarked in the upper-right corner. An exotic species is any species which was not observed with a natural isotopic distribution.

The 13 known trace metal impurities of Clinton Pu are indicated by an earmark in the upper right corner in Figure 4.09; 12 of these impurities were positively identified in the Pu samples. The trace metal content of Clinton Pu was observed to vary slightly by each lot sent to Los Alamos, so the absence of Be in these samples is still consistent with the documented trace metal content reported during the Manhattan Project (*111*). The identification of La, Ce, and Bi is an indication that this material was previously separated using the bismuth phosphate process. The trace metals which are positively identified here, but not in the previous Manhattan Project report, were present on the order of 100 ppb or less. These concentrations were below the detection limit of any element in their report (*111*).

4.6 Forensic Conclusions

The masses of Plutonium 1, 2, and 4 were assayed via alpha spectrometry and found to be significantly lower than suggested by their labeling. This suggests the three samples were used as solid stocks of Pu and material was removed after their initial containment. Isotopic analysis indicates all four samples are of super-grade quality, consistent with known samples of Clinton Pu.

The chronometric ages of Plutonium 1, 2, and 4 are reported as April 1954 ± 24 months, December 1947 ± 22 months, and February 1944 ± 11 months, respectively. This indicates that Plutonium 4 was last chemically separated in the earliest days of weapons science, dating back to the first shipments of Clinton Pu from the X-10 reactor to Los Alamos. The isotopics of Plutonium 4 match exceptionally well with the X-10 reactor model at 1 MW operating power, and the fuel burnup predicted by the 1 MW reactor model is consistent with the documented fuel burnup discharged from the X-10 reactor. These results support the production age of Plutonium 4 in the early half of 1944 by the X-10 reactor, which produced less than one kilogram of Pu before switching to the 4 MW operating level. The trace metals identified in the four Pu samples are consistent with the known metal impurities of Clinton Pu as reported during the Manhattan Project.

For all of these aforementioned reasons, it is concluded that Plutonium 4 was produced as Clinton Pu from the X-10 reactor during the second World War, and is among the first kilogram of Pu ever produced by humankind in the early half of 1944; this sample represents the oldest identified reactor-produced Pu in the open

literature as of October 2019. The similar Pu isotopics of the other three samples are consistent with production as Clinton Pu, however there isn't enough ^{238}Pu or ^{234}U in those smaller samples to confirm their identity as Clinton Pu.

CHAPTER V

SUMMARY OF RESEARCH AND FUTURE WORK

All work performed within this dissertation aimed to move the field of nuclear forensics forward with new analytical tools to discriminate the history of special nuclear material. Several radioanalytical characterizations were performed on samples of irradiated UO_2 containing weapons-usable Pu to support the development of a novel reactor-source discrimination methodology (*44*). The characterizations performed herein were used to correctly discriminate the irradiation history of those irradiated UO_2 materials with the forensics methodology and provide a precedent for future applications of the methodology in studies of newly irradiated materials (*53*). Future studies of newly irradiated low-enriched U (LEU) would benefit from following Chapter II of this dissertation and applying some of the separation techniques discussed in Chapter III for a more thorough evaluation of the Cs and Ba fission products. Such LEU samples are expected to arrive for analysis with the Texas A&M forensics collaboration within the next year.

In continued support of the methodology, larger samples of Pu up to 60 mg were separated at Los Alamos National Laboratory to provide a characterized procedure for applying the methodology to samples of separated weapons-grade Pu. Such work may be used as the basis for a future forensics study of large quantities (grams or more) of interdicted Pu. These potential new studies would need to

dissolve at least a 5 g sample of Pu and process it through the procedures as discussed in Chapter III of this dissertation.

The work reported here also used traditional tools in nuclear forensics to discriminate and confirm the history of what is currently known to be the world's oldest reactor-produced Pu. The forensic investigation used to discriminate the origin of this historic material brought the scope of reactor discrimination forward in a significant way, providing a measurable distinction between the discharge of fuel between different operating power levels of a single nuclear reactor.

Appendix A and Appendix B describe some aspects of nuclear forensics as it applies to the PUREX process, which is the most common liquid-liquid extraction procedure used to separate weapons-grade Pu from irradiated U reactor fuel (*185*). Preliminary work presented in Appendix B indicates that some FP and actinide elements are affected differently by altering the extraction conditions used in the PUREX process; therefore, by carefully studying the extraction chemistry of each FP and actinide element, it may be possible to identify forensic signatures which describe the extraction conditions used to purify a sample of weapons-grade Pu, or from which stream of the PUREX process a sample of Pu was discharged. Future work in this area should focus on applying process-engineering models to observe trends in FP and actinide extraction chemistry based on a solution's temperature, acidity, uranyl nitrate concentration, and extractant saturation (*186*). A careful observer may find some FP or actinide nuclide ratios which are indicative of the extraction chemistry used to purify the Pu

REFERENCES

1. S. Niemeyer, L. Koch, The Historical Evolution of Nuclear Forensics: A Technical Viewpoint. Paper presented at the International Conference on Advances in Nuclear Forensics, Vienna, Austria, 2014. IAEA-CN-218-117

2. T. Fanghänel, K. Mayer, Z. Varga, M. Wallenius, 20 Years of Nuclear Forensics at ITU: Between R&D and Case Work. Paper presented at the International Conference on Advances in Nuclear Forensics, Vienna, Austria, 2014. IAEA-CN-218-44

3. V. P. Kuchinov, Development of Nuclear Forensics in Russia. Paper presented at the International Conference on Advances in Nuclear Forensics, Vienna, Austria, 2014. IAEA-CN-218-118

4. International Report, Nuclear Security Communiqué. Paper presented at the International Nuclear Security Summit, Washington D.C, United States of America, 2016. http://www.nss2016.org/

5. International Report, Nuclear Security Communiqué. Paper presented at the International Nuclear Security Summit, The Hague, Netherlands, 2014. http://www.nss2016.org/

6. International Report, Nuclear Security Communiqué. Paper presented at the International Nuclear Security Summit, Seoul, Republic of Korea, 2012. http://www.nss2016.org/

7. International Report, Nuclear Security Communiqué. Paper presented at the International Nuclear Security Summit, Washington D.C, United States of America, 2010. http://www.nss2016.org/

8. M. J. Kristo, S. J. Tumey, The state of nuclear forensics. *Nucl. Instrum. Methods Phys. Res. B* **294**, 656-661 (2013). doi:10.1016/j.nimb.2012.07.047

9. B. L. Byerly, F. Stanley, K. Spencer, L. Colletti, K. Garduno, K. Kuhn, E. Lujan, A. Martinez, D. Porterfield, J. Rim, M. Schappert, M. Thomas, L. Townsend, N. Xu, L. Tandon, Forensic investigation of plutonium metal: A case study of CRM 126. *J. Radioanal. Nucl. Chem.* **310**, 623-632 (2016). doi:10.1007/s10967-016-4919-x

10. J. H. Rim, K. J. Kuhn, L. Tandon, N. Xu, D. R. Porterfield, C. G. Worley, M. R. Thomas, K. J. Spencer, F. E. Stanley, E. J. Lujan, K. Garduno, H. R. Trellue, Determination of origin and intended use of plutonium metal using nuclear forensic techniques. *Forensic Sci. Int.* **273**, e1-e9 (2017). doi:10.1016/j.forsciint.2017.01.014

11. J. A. Savina, J. L. Steeb, M. R. Savina, C. J. Mertz, J. A. Fortner, V. S. Sullivan, M. E. Bennett, D. B. Chamberlain, A non-destructive internal nuclear forensic investigation at Argonne: discovery of a Pu planchet from 1948. *J. Radioanal. Nucl. Chem.* **311**, 243-252 (2017). doi:10.1007/s10967-016-4893-3

12. J. M. Schwantes, M. Douglas, S. E. Bonde, J. D. Briggs, O. T. Farmer, L. R. Greenwood, E. A. Lepel, C. R. Orton, J. F. Wacker, A. T. Luksic, Nuclear archeology in a bottle: Evidence of pre-Trinity U.S. weapons activities from a waste burial site. *Anal. Chem.* **81**, 1297-1306 (2009). doi:10.1021/ac802286a

13. E. Keegan, M. J. Kristo, K. Toole, R. Kips, E. Young, Nuclear Forensics: Scientific Analysis Supporting Law Enforcement and Nuclear Security Investigations. *Anal. Chem.* **88**, 1496-1505 (2016). doi:10.1021/acs.analchem.5b02915

14. M. J. Kristo, A. M. Gaffney, N. Marks, K. Knight, W. S. Cassata, I. D. Hutcheon, Nuclear Forensic Science: Analysis of Nuclear Material Out of Regulatory Control. *Annu. Rev. Earth Planet. Sci.* **44**, 555-579 (2016). doi:10.1146/annurev-earth-060115-012309

15. M. May, R. Abedin-Zadeh, D. Barr, A. Carnesale, P. Coyle, J. Davis, W. Dorland, W. Dunlop, S. Fetter, A. Glaser, I. Hutcheon, F. Slakey, B. Tannenbaum, "Nuclear Forensics: Role, State of the Art, Program Needs," (Joint report from the American Physical Society and the American Association for the Advancement of Science, 2008). https://www.aps.org/policy/reports/popa-reports/forensics.cfm

16. J. M. Osborn, K. J. Glennon, E. D. Kitcher, J. D. Burns, C. M. Folden III, S. S. Chirayath, Computational and experimental forensics characterization of weapons-grade plutonium produced in a thermal neutron environment. *Nucl. Eng. Technol.* **50**, 820-828 (2018). doi:10.1016/j.net.2018.04.017

17. M. W. Swinney, C. M. Folden III, R. J. Ellis, S. S. Chirayath, Experimental and computational forensics characterization of weapons-grade plutonium produced in a fast reactor neutron environment. *Nucl. Technol.* **197**, 1-11 (2017). doi:10.13182/NT16-76

18. K. J. Moody, I. D. Hutcheon, P. M. Grant, *Nuclear Forensic Analysis*. (CRC Press, Boca Raton, 2015).

19. W. D. Loveland, D. J. Morrissey, G. T. Seaborg, in *Modern Nuclear Chemistry*. (John Wiley & Sons, Inc., Hoboken, 2017), pp. 663-682.

20. B. Byerly, K. Kuhn, L. Colletti, L. Foster, R. Keller, E. Lujan, A. Martinez, D. Porterfield, D. Schwartz, K. Spencer, F. Stanley, M. Thomas, L. Townsend, N. Xu, L. Tandon, Chemical investigation of three plutonium-beryllium neutron sources. *J. Radioanal. Nucl. Chem.* **312**, 95-104 (2017). doi:10.1007/s10967-017-5192-3

21. J. L. Doyle, K. Kuhn, B. Byerly, L. Colletti, J. Fulwyler, K. Garduno, R. Keller, E. Lujan, A. Martinez, S. Myers, D. Porterfield, K. Spencer, F. Stanley, L. Townsend, M. Thomas, L. Walker, N. Xu, L. Tandon, Nuclear forensic analysis of a non-traditional actinide sample. *Talanta* **159**, 200-207 (2016). doi:10.1016/j.talanta.2016.06.028

22. F. E. Stanley, A. M. Stalcup, H. B. Spitz, A brief introduction to analytical methods in nuclear forensics. *J. Radioanal. Nucl. Chem.* **295**, 1385-1393 (2013). doi:10.1007/s10967-012-1927-3

23. K. Lutzenkirchen, M. Wallenius, Z. Varga, T. Wiss, A. Knott, A. Nicholl, K. Mayer, Nuclear forensics on uranium fuel pellets. *Radiochim. Acta* **107**, 635-643 (2019). doi:10.1515/ract-2018-3068

24. K. L. Nash, M. Nilsson, in *Reprocessing and Recycling of Spent Nuclear Fuel*. (Woodhead Publishing, Oxford, 2015), pp. 3-25.

25. M. Christl, N. Guérin, M. Totland, A. Gagn, Z. Kazi, S. Burrell, H. A. Synal, A novel chronometry technique for dating irradiated uranium fuels using Cm isotopic ratios. *J. Radioanal. Nucl. Chem.* **322**, 1611-1620 (2019). doi:10.1007/s10967-019-06767-4

26. K. Mathew, T. Kayzar-Boggs, Z. Varga, A. Gaffney, J. Denton, J. Fulwyler, K. Garduno, A. Gaunt, J. Inglis, R. Keller, W. Kinman, D. Labotka, E. Lujan, J. Maassen, T. Mastren, I. May, K. Mayer, A. Nicholl, C. Ottenfeld, T. Parsons-Davis, D. Porterfield, J. Rim, J. Rolison, F. Stanley, R. Steiner, L. Tandon, M. Thomas, R. Torres, K. Treinen, M. Wallenius, A. Wende, R. Williams, J. Wimpenny, Intercomparison of the radio-chronometric ages of plutonium-certified reference materials with distinct isotopic compositions. *Anal. Chem.* **91**, 11643-11652 (2019). doi:10.1021/acs.analchem.9b02156

27. M. Higginson, C. Gilligan, F. Taylor, D. Knight, P. Kaye, T. Shaw, P. Thompson, Development of rapid methodologies for uranium age dating. *J. Radioanal. Nucl. Chem.* **318**, 157-164 (2018). doi:10.1007/s10967-018-6021-z

28. F. E. Stanley, K. J. Mathew, B. L. Byerly, R. Keller, K. J. Spencer, M. R. Thomas, Pursuing standards strategies in nuclear forensics: investigating extraction of progeny uranium in CRM-126a as a quality control material in Pu-U chronometry. *J. Radioanal. Nucl. Chem.* **311**, 1819-1824 (2017). doi:10.1007/s10967-016-5133-6

29. M. Sturm, S. Richter, Y. Aregbe, R. Wellum, T. Prohaska, Optimized Chemical Separation and Measurement by TE TIMS Using Carburized Filaments for Uranium Isotope Ratio Measurements Applied to Plutonium Chronometry. *Anal. Chem.* **88**, 6223-6230 (2016). doi:10.1021/acs.analchem.5b03852

30. L. A. Meyers, S. E. Glover, S. P. LaMont, A. M. Stalcup, H. B. Spitz, Radiological chronometry of uranium metal samples. *J. Radioanal. Nucl. Chem.* **299**, 1833-1837 (2014). doi:10.1007/s10967-013-2880-5

31. T. M. Kayzar-Boggs, K. C. Treinen, A. Okubo, J. S. Denton, A. M. Gaffney, M. M. Miller, R. E. Steiner, A. M. Wende, R. W. Williams, An interlaboratory

collaboration to determine consensus Pa-231/U-235 model ages of a uranium certified reference material for nuclear forensics. *J. Radioanal. Nucl. Chem.* **323**, 1189-1195 (2020). doi:10.1007/s10967-020-07030-x

32. Z. Varga, A. Nicholl, M. Wallenius, K. Mayer, Plutonium age dating (production date measurement) by inductively coupled plasma mass spectrometry. *J. Radioanal. Nucl. Chem.* **307**, 1919-1926 (2016). doi:10.1007/s10967-015-4418-5

33. Z. Varga, A. Nicholl, J. Zsigrai, M. Wallenius, K. Mayer, Methodology for the preparation and validation of plutonium age dating materials. *Anal. Chem.* **90**, 4019-4024 (2018). doi:10.1021/acs.analchem.7b05204

34. Z. Varga, M. Wallenius, A. Nicholl, K. Mayer, I. Balan, V. Benea, Measurement of production date (age) of nanogram amount of uranium. *J. Radioanal. Nucl. Chem.* **322**, 1585-1591 (2019). doi:10.1007/s10967-019-06705-4

35. K. C. Treinen, K. M. Samperton, R. E. Lindvall, J. B. Wimpenny, A. M. Gaffney, M. Bavio, E. J. Baransky, R. W. Williams, Evaluating uranium radiochronometry by single-collector mass spectrometry for nuclear forensics: a multi-instrument investigation. *J. Radioanal. Nucl. Chem.* **322**, 1627-1640 (2019). doi:10.1007/s10967-019-06832-y

36. Z. Varga, A. Nicholl, E. Hrnecek, M. Wallenius, K. Mayer, Measurement of the Pa-231/U-235 ratio for the age determination of uranium materials. *J. Radioanal. Nucl. Chem.* **318**, 1565-1571 (2018). doi:10.1007/s10967-018-6247-9

37. K. B. Lavelle, R. M. Essex, K. P. Carney, J. T. Cessna, C. R. Hexel, A reference material for evaluation of Cs-137 radiochronometric measurements. *J. Radioanal. Nucl. Chem.* **318**, 195-208 (2018). doi:10.1007/s10967-018-6061-4

38. K. C. Treinen, A. M. Gaffney, J. M. Rolison, K. M. Samperton, K. C. McHugh, M. L. Miller, R. W. Williams, Improved protactinium spike calibration method applied to Pa-231-U-235 age-dating of certified reference materials for nuclear forensics. *J. Radioanal. Nucl. Chem.* **318**, 209-219 (2018). doi:10.1007/s10967-018-6149-x

39. D. R. McLain, Y. Tsai, D. G. Graczyk, J. L. Canaday, J. L. Steeb, An alternative separation procedure for Sr-90 age dating using DGA Resin. *J. Radioanal. Nucl. Chem.* **317**, 1439-1445 (2018). doi:10.1007/s10967-018-6057-0

40. J. M. Rolison, R. W. Williams, Application of the Ra-226-Th-230-U-234 and Ac-227-Pa-231-U-235 radiochronometers to UF_6 cylinders. *J. Radioanal. Nucl. Chem.* **317**, 897-905 (2018). doi:10.1007/s10967-018-5955-5

41. A. I. Apostol, J. Zsigrai, J. Bagi, M. Brandis, J. Nikolov, K. Mayer, Characterization of californium sources by gamma spectrometry: relevance for nuclear forensics. *J. Radioanal. Nucl. Chem.* **321**, 405-412 (2019). doi:10.1007/s10967-019-06628-0

42. C. M. Fallon, W. R. Bower, I. C. Lyon, F. R. Livens, P. Thompson, M. Higginson, J. Collins, S. L. Heath, G. T. W. Law, Isotopic and compositional variations in single nuclear fuel pellet particles analyzed by nanoscale secondary ion mass spectrometry. *ACS Omega* **5**, 296-303 (2020). doi:10.1021/acsomega.9b02703

43. P. M. Mendoza, S. S. Chirayath, C. M. Folden III, Fission product decontamination factors for plutonium separated by PUREX from low-burnup, fast-neutron irradiated depleted UO_2. *Appl. Radiat. Isot.* **118**, 38-42 (2016). doi:10.1016/j.apradiso.2016.08.021

44. K. J. Glennon, J. M. Osborn, J. D. Burns, E. D. Kitcher, S. S. Chirayath, C. M. Folden, Measuring key Sm isotope ratios in irradiated UO_2 for use in plutonium discrimination nuclear forensics. *J. Radioanal. Nucl. Chem.* **320**, 405-414 (2019). doi:10.1007/s10967-019-06486-w

45. J. Wacker, New advances in inductively coupled plasma – mass spectrometry (ICP-MS) for routine measurements in the nuclear industry. *J. Radioanal. Nucl. Chem.* **249**, 103-108 (2001). doi:10.1023/a:1013202206031

46. J. S. Becker, Inductively coupled plasma mass spectrometry (ICP-MS) and laser ablation ICP-MS for isotope analysis of long-lived radionuclides. *Int. J. Mass Spectrom.* **242**, 183-195 (2005). doi:10.1016/j.ijms.2004.11.009

47. S. F. Boulyga, C. Testa, D. Desideri, J. S. Becker, Optimisation and application of ICP-MS and alpha-spectrometry for determination of isotopic ratios of depleted uranium and plutonium in samples collected in Kosovo. *J. Anal. At. Spectrom.* **16**, 1283-1289 (2001). doi:10.1039/B103178N

48. C. J. Palmer, K. R. Gerez, J. M. Schwantes, R. A. Clark, Scoping evaluation of trace isotopic ratios within the noble metal-phase as indicators of reactor class. *Prog. Nucl. Energy* **117**, 8 (2019). doi:10.1016/j.pnucene.2019.103059

49. J. A. Dunne, D. A. Richards, H. W. Chen, Procedures for precise measurements of Cs-135/Cs-137 atom ratios in environmental samples at extreme dynamic ranges and ultra-trace levels by thermal ionization mass spectrometry. *Talanta* **174**, 347-356 (2017). doi:10.1016/j.talanta.2017.06.033

50. E. E. Groopman, K. S. Grabowski, A. J. Fahey, L. Koop, Rapid, molecule-free, in situ rare earth element abundances by SIMS-SSAMS. *J. Anal. At. Spectrom.* **32**, 2153-2163 (2017). doi:10.1039/c7ja00294g

51. S. S. Chirayath, J. M. Osborn, T. M. Coles, Trace fission product ratios for nuclear forensics attribution of weapons-grade plutonium from fast and thermal reactors. *Sci. Global Secur.* **23**, 48-67 (2015). doi:10.1080/08929882.2015.996079

52. E. D. Kitcher, J. M. Osborn, S. S. Chirayath, Sensitivity studies on a novel nuclear forensics methodology for source reactor-type discrimination of separated weapons grade plutonium. *Nucl. Eng. Technol.* **51**, 1355-1364 (2019). doi:10.1016/j.net.2019.02.019

53. J. M. Osborn, K. J. Glennon, E. D. Kitcher, J. D. Burns, C. M. Folden III, S. S. Chirayath, Experimental validation of a nuclear forensics methodology for source reactor-type discrimination of chemically separated plutonium. *Nucl. Eng. Technol.* **51**, 384-393 (2018). doi:10.1016/j.net.2018.11.003

54. J. M. Osborn, E. D. Kitcher, J. D. Burns, C. M. Folden III, S. S. Chirayath, Nuclear forensics methodology for reactor-type attribution of chemically separated plutonium. *Nucl. Technol.* **201**, 1-10 (2017). doi:10.1080/00295450.2017.1401442

55. M. Wallenius, K. Lützenkirchen, K. Mayer, I. Ray, L. A. de las Heras, M. Betti, O. Cromboom, M. Hild, B. Lynch, A. Nicholl, H. Ottmar, G. Rasmussen, A. Schubert, G. Tamborini, H. Thiele, W. Wagner, C. Walker, E. Zuleger, Nuclear forensic investigations with a focus on plutonium. *J. Alloys Compd.* **444-445**, 57-62 (2007). doi:10.1016/j.jallcom.2006.10.161

56. M. Wallenius, P. Peerani, L. Koch, Origin determination of plutonium material in nuclear forensics. *J. Radioanal. Nucl. Chem.* **246**, 317-321 (2000). doi:10.1023/A:1006774524272

57. A. Favalli, D. Vo, B. Grogan, P. Jansson, H. Liljenfeldt, V. Mozin, P. Schwalbach, A. Sjöland, S. J. Tobin, H. Trellue, S. Vaccaro, Determining initial enrichment, burnup, and cooling time of pressurized-water-reactor spent fuel assemblies by analyzing passive gamma spectra measured at the Clab interim-fuel storage facility in Sweden. *Nucl. Instrum. Methods Phys. Res. A* **820**, 102-111 (2016). doi:10.1016/j.nima.2016.02.072

58. I. Lantzos, C. Kouvalaki, G. Nicolaou, Plutonium fingerprinting in nuclear forensics of spent nuclear fuel. *Prog. Nucl. Energy* **85**, 333-336 (2015). doi:10.1016/j.pnucene.2015.07.002

59. E. M. Redd, G. Sjoden, A. Erickson, Computationally-generated nuclear forensic characteristics of early production reactors with an emphasis on sensitivity and uncertainty. *Ann. Nucl. Energy* **110**, 941-947 (2017). doi:10.1016/j.anucene.2017.07.032

60. G. Nicolaou, Discrimination of spent nuclear fuels in nuclear forensics through isotopic fingerprinting. *Ann. Nucl. Energy* **72**, 130-133 (2014). doi:10.1016/j.anucene.2014.05.016

61. G. Nicolaou, S. R. Biegalski, Discrimination of plutonium from thermal reactors in the frame of nuclear forensics. *J. Radioanal. Nucl. Chem.* **317**, 559-564 (2018). doi:10.1007/s10967-018-5902-5

62. G. Nikolaou, S. R. Biegalski, Discrimination of weapons-grade plutonium from thermal reactors in nuclear forensics. *J. Radioanal. Nucl. Chem.* **322**, 513-518 (2019). doi:10.1007/s10967-019-06810-4

63. J. H. Su, J. Wu, S. D. Hu, Identification of spent nuclear fuel with multivariate analysis based on database. *Acta Phys. Sin.* **68**, 8 (2019). doi:10.7498/aps.68.20190107

64. M. S. Snow, D. C. Snyder, J. E. Delmore, Fukushima Daiichi reactor source term attribution using cesium isotope ratios from contaminated environmental samples. *Rapid Commun. Mass Spectrom.* **30**, 523-532 (2016). doi:10.1002/rcm.7468

65. E. Rollin, O. Musset, D. Cardona, J. B. Sirven, Laser-induced breakdown spectroscopy of uranium in the vacuum ultraviolet range. *Spectroc. Acta Pt. B-Atom. Spectr.* **166**, 6 (2020). doi:10.1016/j.sab.2020.105796

66. T. L. Spano, A. Simonetti, L. Corcoran, P. A. Smith, S. R. Lewis, P. C. Burns, Comparative chemical and structural analyses of two uranium dioxide fuel pellets. *J. Nucl. Mater.* **518**, 149-161 (2019). doi:10.1016/j.jnucmat.2019.02.038

67. D. D. Reilly, M. T. Athon, J. E. Corbey, Leavy, II, K. M. McCoy, J. M. Schwantes, Trace element migration during UF_4 bomb reduction: Implications to metal fuel production, worker health and safety, and nuclear forensics. *J. Nucl. Mater.* **510**, 156-162 (2018). doi:10.1016/j.jnucmat.2018.07.052

68. C. A. Barrett, W. Chouyyok, R. J. Speakman, K. B. Olsen, R. S. Addleman, Rapid extraction and assay of uranium from environmental surface samples. *Talanta* **173**, 69-78 (2017). doi:10.1016/j.talanta.2017.05.052

69. J. Gao, B. T. Manard, A. Castro, D. P. Montoya, N. Xu, R. M. Chamberlin, Solid-phase extraction microfluidic devices for matrix removal in trace element assay of actinide materials. *Talanta* **167**, 8-13 (2017). doi:10.1016/j.talanta.2017.01.080

70. E. Balboni, N. Jones, T. Spano, A. Simonetti, P. C. Burns, Chemical and Sr isotopic characterization of North America uranium ores: Nuclear forensic applications. *Appl. Geochem.* **74**, 24-32 (2016). doi:10.1016/j.apgeochem.2016.08.016

71. K. B. Lavelle, S. Glover, W. B. Connick, H. Spitz, Preconcentration of trace environmental plutonium from iron oxide matrix using DIPEXA (R) extractant. *J. Radioanal. Nucl. Chem.* **301**, 677-683 (2014). doi:10.1007/s10967-014-3236-5

72. E. J. Judge, J. E. Barefield, J. M. Berg, S. M. Clegg, G. J. Havrilla, V. M. Montoya, L. A. Le, L. N. Lopez, Laser-induced breakdown spectroscopy measurements of uranium and thorium powders and uranium ore. *Spectroc. Acta Pt. B-Atom. Spectr.* **83-84**, 28-36 (2013). doi:10.1016/j.sab.2013.03.002

73. S. T. Heffernan, N. C. Ly, B. J. Mower, C. Vachet, I. J. Schwerdt, T. Tasdizen, L. W. McDonald, Identifying surface morphological characteristics to differentiate between mixtures of U3O8 synthesized from ammonium diuranate and uranyl peroxide. *Radiochim. Acta* **108**, 29-36 (2020). doi:10.1515/ract-2019-3140

74. E. C. Abbott, A. Brenkmann, C. Galbraith, J. Ong, I. J. Schwerdt, B. D. Albrecht, T. Tasdizen, L. W. McDonald, Dependence of UO2 surface morphology on processing history within a single synthetic route. *Radiochim. Acta* **107**, 1121-1131 (2019). doi:10.1515/ract-2018-3065

75. C. Ly, A. M. Olsen, I. J. Schwerdt, R. Porter, K. Sentz, L. W. McDonald, T. Tasdizen, A new approach for quantifying morphological features of U3O8 for nuclear forensics using a deep learning model. *J. Nucl. Mater.* **517**, 128-137 (2019). doi:10.1016/j.jnucmat.2019.01.042

76. I. J. Schwerdt, A. Brenkmann, S. Martinson, B. D. Albrecht, S. Heffernan, M. R. Klosterman, T. Kirkham, T. Tasdizen, L. W. McDonald, Nuclear proliferomics: A new field of study to identify signatures of nuclear materials as demonstrated on alpha-UO_3. *Talanta* **186**, 433-444 (2018). doi:10.1016/j.talanta.2018.04.092

77. I. J. Schwerdt, A. Olsen, R. Lusk, S. Heffernan, M. Klosterman, B. Collins, S. Martinson, T. Kirkham, L. W. McDonald, Nuclear forensics investigation of morphological signatures in the thermal decomposition of uranyl peroxide. *Talanta* **176**, 284-292 (2018). doi:10.1016/j.talanta.2017.08.020

78. K. Campbell, E. J. Judge, M. R. Dirmyer, D. Kelly, K. Czerwinski, Synthesis and characterization of surrogate nuclear explosion debris: urban glass matrix. *J. Radioanal. Nucl. Chem.* **314**, 197-206 (2017). doi:10.1007/s10967-017-5367-y

79. A. L. Tamasi, L. J. Cash, W. T. Mullen, A. L. Pugmire, A. R. Ross, C. E. Ruggiero, B. L. Scott, G. L. Wagner, J. R. Walensky, M. P. Wilkerson, Morphology of U3O8 materials following storage under controlled conditions of temperature and relative humidity. *J. Radioanal. Nucl. Chem.* **311**, 35-42 (2017). doi:10.1007/s10967-016-4923-1

80. T. G. Ditcham, A. Wotherspoon, K. P. Kirkbride, C. E. Lenehan, R. S. Popelka-Filcoff, Thermal decomposition of Australian uranium ore concentrates: characterisation of speciation and morphological changes following thermogravimetric analysis. *J. Radioanal. Nucl. Chem.* **310**, 725-732 (2016). doi:10.1007/s10967-016-4871-9

81. A. L. Tamasi, L. J. Cash, W. T. Mullen, A. R. Ross, C. E. Ruggiero, B. L. Scott, G. L. Wagner, J. R. Walensky, S. A. Zerkle, M. P. Wilkerson, Comparison of morphologies of a uranyl peroxide precursor and calcination products. *J. Radioanal. Nucl. Chem.* **309**, 827-832 (2016). doi:10.1007/s10967-016-4692-x

82. E. P. Hastings, C. Lewis, J. FitzPatrick, D. Rademacher, L. Tandon, Characterization of depleted uranium oxides fabricated using different processing methods. *J. Radioanal. Nucl. Chem.* **276**, 475-481 (2008). doi:10.1007/s10967-008-0529-6

83. N. Erdmann, M. Betti, O. Stetzer, G. Tamborini, J. V. Kratz, N. Trautmann, J. van Geel, Production of monodisperse uranium oxide particles and their characterization by scanning electron microscopy and secondary ion mass spectrometry. *Spectroc. Acta Pt. B-Atom. Spectr.* **55**, 1565-1575 (2000). doi:10.1016/s0584-8547(00)00262-7

84. E. Villa-Aleman, A. L. Houk, N. J. Bridges, T. C. Shehee, Raman spectroscopy: A tool to investigate alpha decay damage in a PuO_2 crystal lattice and determining sample age since calcination. *J. Raman Spectrosc.* **50**, 899-901 (2019). doi:10.1002/jrs.5591

85. P. Martz, J. Mercadier, J. Perret, J. Villeneuve, E. Deloule, M. Cathelineau, D. Quirt, A. Doney, P. Ledru, Post-crystallization alteration of natural uraninites: Implications for dating, tracing, and nuclear forensics. *Geochim. Cosmochim. Acta* **249**, 138-159 (2019). doi:10.1016/j.gca.2019.01.025

86. N. T. Hubley, D. L. Wegge, T. M. Weilert, C. P. Leibman, M. S. Rearick, J. D. Robertson, J. D. Brockman, Rapid dissolution of surrogate nuclear debris using ammonium bifluoride fusion and indirect sonication dissolution methods. *J. Radioanal. Nucl. Chem.* **318**, 49-54 (2018). doi:10.1007/s10967-018-6127-3

87. C. A. Mason, N. T. Hubley, J. D. Robertson, D. L. Wegge, J. D. Brockman, Sonication assisted dissolution of post-detonation nuclear debris using ammonium bifluoride. *Radiochim. Acta* **105**, 1059-1070 (2017). doi:10.1515/ract-2017-2802

88. N. T. Hubley, J. D. Brockman, J. D. Robertson, Evaluation of ammonium bifluoride fusion for rapid dissolution in post-detonation nuclear forensic analysis. *Radiochim. Acta* **105**, 629-635 (2017). doi:10.1515/ract-2016-2735

89. S. Biegalski, N. Kane, J. Mann, T. Tipping, K. Dayman, Neutron activation of NIST surrogate post-detonation urban debris (SPUD) candidate SRMs. *J. Radioanal. Nucl. Chem.* **318**, 187-193 (2018). doi:10.1007/s10967-018-6023-x

90. E. C. Koeman, B. K. McNamara, F. N. Smith, A. Simonetti, P. C. Burns, Developing methodologies for source attribution: glass phase separation in Trinitite using NF_3. *Radiochim. Acta* **105**, 417-430 (2017). doi:10.1515/ract-2016-2641

91. P. H. Donohue, A. Simonetti, Vesicle Size Distribution as a Novel Nuclear Forensics Tool. *PLoS One* **11**, 9 (2016). doi:10.1371/journal.pone.0163516

92. M. T. Cook, J. D. Auxier, A. V. Giminaro, J. J. Molgaard, J. R. Knowles, H. L. Hall, A comparison of gamma spectra from trinitite versus irradiated synthetic nuclear melt glass. *J. Radioanal. Nucl. Chem.* **307**, 259-267 (2016). doi:10.1007/s10967-015-4266-3

93. J. J. Molgaard, J. D. Auxier, A. V. Giminaro, C. J. Oldham, J. Gill, H. L. Hall, Production of Synthetic Nuclear Melt Glass. *J. Vis. Exp.*, 7 (2016). doi:10.3791/53473

94. J. J. Molgaard, J. D. Auxier, A. V. Giminaro, C. J. Oldham, M. T. Cook, S. A. Young, H. L. Hall, Development of synthetic nuclear melt glass for forensic analysis. *J. Radioanal. Nucl. Chem.* **304**, 1293-1301 (2015). doi:10.1007/s10967-015-3941-8

95. J. J. Bellucci, A. Simonetti, Nuclear forensics: searching for nuclear device debris in trinitite-hosted inclusions. *J. Radioanal. Nucl. Chem.* **293**, 313-319 (2012). doi:10.1007/s10967-012-1654-9

96. E. Simpson, "The Colorful Nuclide Chart." Last updated April 2020, accessed May 2020. https://people.physics.anu.edu.au/~ecs103/chart/

97. W. D. Loveland, D. J. Morrissey, G. T. Seaborg, in *Modern Nuclear Chemistry*. (John Wiley & Sons, Inc., Hoboken, New Jersey, 2017), pp. 25-55.

98. W. Loveland, D. J. Morrissey, G. T. Seaborg, in *Modern Nuclear Chemistry*. (John Wiley & Sons, Inc., Hoboken, New Jersey, 2017), pp. 57-92.

99. W. Loveland, D. J. Morrissey, G. T. Seaborg, in *Modern Nuclear Chemistry*. (John Wiley & Sons, Inc., Hoboken, 2017), pp. 247-303.

100. N. Otuka, E. Dupont, V. Semkova, B. Pritychenko, A. I. Blokhin, M. Aikawa, S. Babykina, M. Bossant, G. Chen, S. Dunaeva, R. A. Forrest, T. Fukahori, N. Furutachi, S. Ganesan, Z. Ge, O. O. Gritzay, M. Herman, S. Hlavač, K. Katō, B. Lalremruata, Y. O. Lee, A. Makinaga, K. Matsumoto, M. Mikhaylyukova, G. Pikulina, V. G. Pronyaev, A. Saxena, O. Schwerer, S. P. Simakov, N. Soppera, R. Suzuki, S. Takács, X. Tao, S. Taova, F. Tárkányi, V. V. Varlamov, J. Wang, S. C. Yang, V. Zerkin, Y. Zhuang, Towards a More Complete and Accurate Experimental Nuclear Reaction Data Library (EXFOR): International Collaboration Between Nuclear Reaction Data Centres (NRDC). *Nucl. Data Sheets* **120**, 272-276 (2014). doi:10.1016/j.nds.2014.07.065

101. W. Loveland, D. J. Morrissey, G. T. Seaborg, in *Modern Nuclear Chemistry*. (John Wiley & Sons, Inc., Hoboken, 2017), pp. 113-124.

102. G. Choppin, J.-O. Liljenzin, J. Rydberg, C. Ekberg, in *Radiochemistry and Nuclear Chemistry*. (Academic Press, Oxford, 2013), pp. 313-338.

103. D. A. Brown, M. B. Chadwick, R. Capote, A. C. Kahler, A. Trkov, M. W. Herman, A. A. Sonzogni, Y. Danon, A. D. Carlson, M. Dunn, D. L. Smith, G. M. Hale, G. Arbanas, R. Arcilla, C. R. Bates, B. Beck, B. Becker, F. Brown, R. J. Casperson, J. Conlin, D. E. Cullen, M. A. Descalle, R. Firestone, T. Gaines, K. H. Guber, A. I. Hawari, J. Holmes, T. D. Johnson, T. Kawano, B. C. Kiedrowski, A. J. Koning, S. Kopecky, L. Leal, J. P. Lestone, C. Lubitz, J. I. Márquez Damián, C. M. Mattoon, E. A. McCutchan, S. Mughabghab, P. Navratil, D. Neudecker, G. P. A. Nobre, G. Noguere, M. Paris, M. T. Pigni, A. J. Plompen, B. Pritychenko, V. G. Pronyaev, D. Roubtsov, D. Rochman, P. Romano, P. Schillebeeckx, S. Simakov, M. Sin, I. Sirakov, B. Sleaford, V. Sobes, E. S. Soukhovitskii, I. Stetcu, P. Talou, I. Thompson, S. van der Marck, L. Welser-Sherrill, D. Wiarda, M. White, J. L. Wormald, R. Q. Wright, M. Zerkle, G. Žerovnik, Y. Zhu, ENDF/B-VIII.0: The 8th Major Release of the Nuclear Reaction Data Library with CIELO-project Cross Sections, New Standards and Thermal Scattering Data. *Nucl. Data Sheets* **148**, 1-142 (2018). doi:10.1016/j.nds.2018.02.001

104. K. Shibata, O. Iwamoto, T. Nakagawa, N. Iwamoto, A. Ichihara, S. Kunieda, S. Chiba, K. Furutaka, N. Otuka, T. Ohsawa, T. Murata, H. Matsunobu, A. Zukeran, S. Kamada, J.-i. Katakura, JENDL-4.0: A New Library for Nuclear Science and Engineering. *J. Nucl. Sci. Technol.* **48**, 1-30 (2011). doi:10.1080/18811248.2011.9711675

105. W. Loveland, D. J. Morrissey, G. T. Seaborg, in *Modern Nuclear Chemistry*. (Hoboken, 2017), pp. 509-551.

106. W. Loveland, D. J. Morrissey, G. T. Seaborg, in *Modern Nuclear Chemistry*. (Hoboken, 2017), pp. 553-601.

107. D. Hawkins, "Manhattan District History, Project Y, The Los Alamos Project," *LA-MS-2532* (Los Alamos National Laboratory, 1946).

108. J. W. Kennedy, G. T. Seaborg, E. Segrè, A. C. Wahl, Properties of 94(239). *Phys. Rev.* **70**, 555-556 (1946). doi:10.1103/PhysRev.70.555

109. G. T. Seaborg, Transuranium elements: Past, present, and future. *Acc. Chem. Res.* **28**, 257-264 (1995). doi:10.1021/ar00054a003

110. R. Duffield, C. Garner, A. Wahl, "Los Alamos project handbook, chemistry of plutonium," *LA-30* (Los Alamos National Laboratory, 1944).

111. A. C. Wahl, D. F. Mastick, F. K. Pittman, "Purification of Pu," *LA-75* (Los Alamos National Laboratory, 1944).

112. D. A. Skoog, F. J. Holler, S. R. Crouch, in *Principals of Instrumental Analysis*. (Brooks Cole, Belmont, 2007), pp. 816 - 855.

113. C. Song, P. Wang, H. A. Makse, A phase diagram for jammed matter. *Nature* **453**, 629-632 (2008). doi:10.1038/nature06981

114. D. A. Skoog, F. J. Holler, S. R. Crouch, in *Principals of Instrumental Analysis*. (Brooks Cole, Belmont, 2007), pp. 762 - 787.

115. K. L. Nash, M. P. Jensen, Analytical-scale separations of the lanthanides: A review of techniques and Fundamentals. *Sep. Sci. Technol.* **36**, 1257-1282 (2001). doi:10.1081/SS-100103649

116. M. Kumar, Recent trends in chromatographic procedures for separation and determination of rare earth elements. *Analyst (Cambridge, U. K.)* **119**, 2013-2024 (1994). doi:10.1039/an9941902013

117. J. M. Schwantes, R. S. Rundberg, W. A. Taylor, D. J. Vieira, Rapid, high-purity, lanthanide separations using HPLC. *J. Alloys Compd.* **418**, 189-194 (2006). doi:101016/jjallcom200508110

118. B. J. Bene, W. A. Taylor, E. R. Birnbaum, R. Sudowe, Chromatographic separation of thulium from erbium for neutron capture cross section

measurements-Part II: Preparative scale separation. *J. Radioanal. Nucl. Chem.* **311**, 155-163 (2017). doi:10.1007/s10967-016-4889-z

119. R. Trikha, B. K. Sharma, K. N. Sabharwal, K. Prabhu, Elution profiles of lanthanides with α-hydroxyisobutyric acid by ion exchange chromatography using fine resin. *J. Sep. Sci.* **38**, 3810-3814 (2015). doi:10.1002/jssc.201500628

120. V. Mocko, W. A. Taylor, F. M. Nortier, J. W. Engle, T. E. Barnhart, R. J. Nickles, A. D. Pollington, G. J. Kunde, M. W. Rabin, E. R. Birnbaum, Isolation of Ho-163 from dysprosium target material by HPLC for neutrino mass measurements. *Radiochim. Acta* **103**, 577-585 (2015). doi:10.1515/ract-2014-2362

121. X. Y. Chen, G. S. Goff, W. C. Ewing, B. L. Scott, W. Runde, Solid-State and Solution-State Coordination Chemistry of Lanthanide(III) Complexes with alpha-Hydroxyisobutyric Acid. *Inorg. Chem.* **51**, 13254-13263 (2012). doi:10.1021/ic301775d

122. N. M. Raut, P. G. Jaison, S. K. Aggarwal, Comparative evaluation of three alpha-hydroxycarboxylic acids for the separation of lanthanides by dynamically modified reversed-phase high-performance liquid chromatography. *J. Chromatogr. A* **959**, 163-172 (2002). doi:10.1016/s0021-9673(02)00447-8

123. R. Garcia-Valls, A. Hrdlicka, J. Perutka, J. Havel, N. V. Deorkar, L. L. Tavlarides, M. Munoz, M. Valiente, Separation of rare earth elements by high performance liquid chromatography using a covalent modified silica gel column. *Anal. Chim. Acta* **439**, 247-253 (2001). doi:10.1016/s0003-2670(01)01044-3

124. N. Gharibyan, B. J. Bene, R. Sudowe, Chromatographic separation of thulium from erbium for neutron capture cross section measurements—Part I: Trace scale optimization of ion chromatography method with various complexing agents. *J. Radioanal. Nucl. Chem.* **311**, 179-187 (2017). doi:10.1007/s10967-016-4926-y

125. J. M. Schwantes, W. A. Taylor, R. S. Rundberg, D. J. Vieira, Preparation of a one-curie Tm-171 target for the Detector for Advanced Neutron Capture Experiments (DANCE). *J. Radioanal. Nucl. Chem.* **276**, 533-542 (2008). doi:10.1007/s10967-008-0538-5

126. C. Bromba, P. Carrie, J. K. W. Chui, T. M. Fyles, Phenyl boronic acid complexes of diols and hydroxyacids. *Supramol. Chem.* **21**, 81-88 (2009). doi:10.1080/10610270802527044

127. I. Günther-Leopold, N. Kivel, J. Kobler Waldis, B. Wernli, Characterization of nuclear fuels by ICP mass-spectrometric techniques. *Anal. Bioanal. Chem.* **390**, 503-510 (2008). doi:10.1007/s00216-007-1644-x

128. G. R. Choppin, R. J. Silva, Separation of the lanthanides by ion exchange with alpha-hydroxy isobutyric acid. *J. Inorg. Nucl. Chem.* **3**, 153-154 (1956). doi:10.1016/0022-1902(56)80076-6

129. M. Seitz, A. G. Oliver, K. N. Raymond, The Lanthanide Contraction Revisited. *J. Am. Chem. Soc.* **129**, 11153-11160 (2007). doi:10.1021/ja072750f

130. K. N. Raymond, D. L. Wellman, C. Sgarlata, A. P. Hill, Curvature of the lanthanide contraction: An explanation. *Cr. Chim.* **13**, 849-852 (2010). doi:10.1016/j.crci.2010.03.034

131. J. A. Peters, K. Djanashvili, C. Geraldes, C. Platas-Iglesias, The chemical consequences of the gradual decrease of the ionic radius along the Ln-series. *Coord. Chem. Rev.* **406**, 27 (2020). doi:10.1016/j.ccr.2019.213146

132. B. P. Sobolev, Lanthanum and Lanthanide Trifluorides: Lanthanide Contraction and Volume of Fluorine Ion. *Crystallogr. Rep.* **65**, 175-181 (2020). doi:10.1134/s1063774520020212

133. J. E. Powell, The nature of the complex exchange process in rare-earth elutions with lactate and α-hydroxyisobutyrate. *J. Inorg. Nucl. Chem.* **30**, 1331-1334 (1968). doi:10.1016/0022-1902(68)80565-2

134. R. Portanova, L. H. J. Lajunen, M. Tolazzi, J. Piispanen, Critical evaluation of stability constants for alpha-hydroxycarboxylic acid complexes with protons and metal ions and the accompanying enthalpy changes. Part II. Aliphatic 2-hydroxycarboxylic acids (IUPAC Technical Report). **75**, 495 (2003). doi:10.1351/pac200375040495

135. J. S. Thayer, Relativistic Effects and the Chemistry of the Heaviest Main-Group Elements. *J. Chem. Educ.* **82**, 1721 (2005). doi:10.1021/ed082p1721

136. J. S. Thayer, *Relativistic Methods for Chemists*. J. Leszczynski, Ed., (Springer Netherlands, ed. 1, 2010).

137. V. A. Dzuba, Ionization potentials and polarizabilities of superheavy elements from Db to Cn (Z = 105-112). *Phys. Rev. A* **93**, 032517/032511-032519/032515 (2016). doi:10.1103/PhysRevA.93.032519

138. V. A. Dzuba, V. V. Flambaum, Electron structure of superheavy elements Uut, Fl and Uup (Z=113 to 115). *Hyperfine Interact.* **237**, 1-17 (2016). doi:10.1007/s10751-016-1365-7

139. L. Seijo, Z. Barandiaran, E. Harguindey, The ab initio model potential method: Lanthanide and actinide elements. *J. Chem. Phys.* **114**, 118-129 (2001). doi:10.1063/1.1330209

140. W. H. E. Schwarz, *Relativistic Methods for Chemists*. J. Leszczynski, Ed., Challenges and Advances in Computational Chemistry and Physics (Springer Netherlands, ed. 1, 2010), pp. XIV, 613.

141. W. H. E. Schwarz, E. M. v. Wezenbeek, E. J. Baerends, J. G. Snijders, The origin of relativistic effects of atomic orbitals. *J. Phys. B. At. Mol. Opt.* **22**, 1515 (1989).

142. J. D. Burns, S. M. Van Cleve, E. H. Smith, R. A. Boll, Californium purification and electrodeposition. *J. Radioanal. Nucl. Chem.* **305**, 109-116 (2015). doi:10.1007/s10967-014-3815-5

143. J. Runke, C. E. Düllmann, K. Eberhardt, P. A. Ellison, K. E. Gregorich, S. Hofmann, E. Jäger, B. Kindler, J. V. Kratz, J. Krier, B. Lommel, C. Mokry, H. Nitsche, J. B. Roberto, K. P. Rykaczewski, M. Schädel, P. Thörle-Pospiech, N. Trautmann, A. Yakushev, Preparation of actinide targets for the synthesis of the heaviest elements. *J. Radioanal. Nucl. Chem.* **299**, 1081-1084 (2014). doi:10.1007/s10967-013-2616-6

144. G. R. Choppin, B. G. Harvey, S. G. Thompson, A new eluant for the separation of the actinide elements. *J. Inorg. Nucl. Chem.* **2**, 66-68 (1956). doi:10.1016/0022-1902(56)80105-X

145. E. R. Bertelsen, J. A. Jackson, J. C. Shafer, A Survey of Extraction Chromatographic f-Element Separations Developed by E. P. Horwitz. *Solvent Extr. Ion Exch.* **38**, 251-289 (2020). doi:10.1080/07366299.2020.1720958

146. M. Snow, J. Ward, Fundamental distribution coefficient data and separations using eichrom extraction chromatographic resins. *J. Chromatogr. A* **1620**, 7 (2020). doi:10.1016/j.chroma.2019.460833

147. J. P. Faris, R. F. Buchanan, Anion Exchange Characteristics of the Elements in Nitric Acid Medium. *Anal. Chem.* **36**, 1157-1158 (1964). doi:10.1021/ac60212a067

148. S. F. Marsh, J. E. Alarid, C. F. Hamond, M. J. McLeod, F. R. Roensch, J. E. Rein, "Cation exchange of 53 elements in nitric acid," *LA-7083* (Los Alamos National Laboratory, United States, 1978).

149. S. F. Marsh, J. E. Alarid, C. F. Hammond, M. J. McLeod, F. R. Roensch, J. E. Rein, "Anion Exchange of 58 Elements in Hydrobromic Acid and in Hydroiodic Acid," *LA-7084* (Los Alamos National Laboratory, 1978).

150. M. Sáez-Muñoz, J. Ortiz, S. Martorell, J. Gómez-Arozamena, A. Cearreta, Sequential determination of uranium and plutonium in soil and sediment samples by borate salts fusion. *J. Radioanal. Nucl. Chem.* **323**, 1167-1177 (2020). doi:10.1007/s10967-020-07028-5

151. B. J. B. Nelson, J. Wilson, S. Richter, M. J. M. Duke, M. Wuest, F. Wuest, Taking cyclotron Ga-68 production to the next level: Expeditious solid target production of Ga-68 for preparation of radiotracers. *Nucl. Med. Biol.* **80-81**, 24-31 (2020). doi:10.1016/j.nucmedbio.2020.01.005

152. L. Rovan, M. Strok, Optimization of the sample preparation and measurement protocol for the analysis of uranium isotopes by MC-ICP-MS without spike

addition. *J. Anal. At. Spectrom.* **34**, 1882-1891 (2019). doi:10.1039/c9ja00144a

153. W. Wojdowska, D. Pawlak, I. Cieszykowska, M. Zoltowska, T. Janiak, T. Barcikowski, A. Stolarz, J. Choinski, J. Parus, P. Garnuszek, R. Mikolajczak, Improved procedures of $Sc(OH)_3$ precipitation and UTEVA extraction for Sc-44 separation. *Nucl. Med. Rev.* **22**, 56-59 (2019). doi:10.5603/NMR.a2019.0013

154. E. P. Horwitz, M. L. Dietz, R. Chiarizia, H. Diamond, A. M. Essling, D. Graczyk, Separation and preconcentration of uranium from acidic media by extraction chromatography. *Anal. Chim. Acta* **266**, 25-37 (1992). doi:10.1016/0003-2670(92)85276-C

155. E. P. Horwitz, C. A. A. Bloomquist, The preparation, performance and factors affecting band spreading of high efficiency extraction chromatographic columns for actinide separations. *J. Inorg. Nucl. Chem.* **34**, 3851-3871 (1972). doi:10.1016/0022-1902(72)80033-2

156. S. C. Metzger, B. W. Ticknor, K. N. Tevepaugh, D. A. Bostick, E. H. McBay, M. P. Field, H. Kim, C. R. Hexel, Reproducible automated renewable column generation. *Sep. Sci. Technol.* **55**, 860-866 (2020). doi:10.1080/01496395.2019.1577439

157. M. Lopez-Lora, I. Levy, E. Chamizo, Simple and fast method for the analysis of U-236, Np-237, (PU)-P-239 and Pu-240 from seawater samples by Accelerator Mass Spectrometry. *Talanta* **200**, 22-30 (2019). doi:10.1016/j.talanta.2019.03.036

158. S. C. Metzger, K. T. Rogers, D. A. Bostick, E. H. McBay, B. W. Ticknor, B. T. Manard, C. R. Hexel, Optimization of uranium and plutonium separations using TEVA and UTEVA cartridges for MC-ICP-MS analysis of environmental swipe samples. *Talanta* **198**, 257-262 (2019). doi:10.1016/j.talanta.2019.02.034

159. E. P. Horwitz, M. L. Dietz, R. Chiarizia, H. Diamond, S. L. Maxwell, M. R. Nelson, Separation and preconcentration of actinides by extraction chromatography using a supported liquid anion exchanger: application to the characterization

of high-level nuclear waste solutions. *Anal. Chim. Acta* **310**, 63-78 (1995). doi:10.1016/0003-2670(95)00144-O

160. S. Nour, W. C. Burnett, E. P. Horwitz, 234Th analysis of marine sediments via extraction chromatography and liquid scintillation counting. *Appl. Radiat. Isot.* **57**, 235-241 (2002). doi:10.1016/S0969-8043(02)00088-X

161. T. Y. Su, T. L. Tsai, Determination of plutonium-241 in low-level radwastes using radiochemical separation combined with LSC, alpha spectrometer and ICP-MS. *J. Radioanal. Nucl. Chem.* **319**, 447-452 (2019). doi:10.1007/s10967-018-6362-7

162. H. Freymuth, C. D. R. Reekie, H. M. Williams, A Triple-Stack Column Procedure for Rapid Separation of Cu and Zn from Geological Samples. *Geostand. Geoanal. Res.*, 14. doi:10.1111/ggr.12323

163. M. Friebel, E. R. Toth, M. A. Fehr, M. Schonbachler, Efficient separation and high-precision analyses of tin and cadmium isotopes in geological materials. *J. Anal. At. Spectrom.* **35**, 273-292 (2020). doi:10.1039/c9ja00289h

164. C. Dalencourt, M. N. Chabane, J. C. Tremblay-Cantin, D. Lariviere, A rapid sequential chromatographic separation of U- and Th-decay series radionuclides in water samples. *Talanta* **207**, 9 (2020). doi:10.1016/j.talanta.2019.120282

165. J. Engel, R. Maas, J. Woodhead, J. Tympel, A. Greig, A single-column extraction chemistry for isotope dilution U-Pb dating of carbonate. *Chem. Geol.* **531**, 6 (2020). doi:10.1016/j.chemgeo.2019.119311

166. R. Chiariza, E. P. Horwitz, S. D. Alexandrators, M. J. Gula, Diphonix® Resin: A Review of Its Properties and Applications. *Sep. Sci. Technol.* **32**, 1-35 (1997). doi:10.1080/01496399708003184

167. E. P. Horwitz, "Diphonix: A new ion exchange resin for the treatment of industrial waste streams, contaminated groundwaters, and mixed-wastes," *ANL/CHM/PP-75639* (Argonne National Laboratory, 1994). https://www.osti.gov/servlets/purl/10132905

168. E. P. Horwitz, R. Chiarizia, M. L. Dietz, DIPEX: A new extraction chromatographic material for the separation and preconcentration of actinides from aqueous solution. *React. Funct. Polym.* **33**, 25-36 (1997). doi:10.1016/S1381-5148(97)00013-8

169. W. C. Burnett, D. R. Corbett, M. Schultz, E. P. Horwitz, R. Chiarizia, M. Dietz, A. Thakkar, M. Fern, Pre-concentration of actinide elements from soils and large volume water samples using extraction chromatography. *J. Radioanal. Nucl. Chem.* **226**, 121-127 (1997). doi:10.1007/BF02063635

170. D. R. McAlister, E. P. Horwitz, Characterization of Extraction of Chromatographic Materials Containing Bis(2-ethyl-1-hexyl)Phosphoric Acid, 2-Ethyl-1-Hexyl (2-Ethyl-1-Hexyl) Phosphonic Acid, and Bis(2,4,4-Trimethyl-1-Pentyl)Phosphinic Acid. *Solvent Extr. Ion Exch.* **25**, 757-769 (2007). doi:10.1080/07366290701634594

171. E. Philip Horwitz, D. R. McAlister, M. L. Dietz, Extraction Chromatography Versus Solvent Extraction: How Similar are They? *Sep. Sci. Technol.* **41**, 2163-2182 (2006). doi:10.1080/01496390600742849

172. W. Bu, J. Zheng, X. Liu, K. Long, S. Hu, S. Uchida, Mass spectrometry for the determination of fission products 135Cs, 137Cs and 90Sr: A review of methodology and applications. *Spectrochim. Acta B Atom. Spec.* **119**, 65-75 (2016). doi:10.1016/j.sab.2016.03.008

173. B. C. Russell, I. W. Croudace, P. E. Warwick, Determination of 135Cs and 137Cs in environmental samples: A review. *Anal. Chim. Acta* **890**, 7-20 (2015). doi:10.1016/j.aca.2015.06.037

174. B. C. Russell, I. W. Croudace, P. E. Warwick, J. A. Milton, Determination of Precise 135Cs/137Cs Ratio in Environmental Samples Using Sector Field Inductively Coupled Plasma Mass Spectrometry. *Anal. Chem.* **86**, 8719-8726 (2014). doi:10.1021/ac501894a

175. B. C. Russell, P. E. Warwick, I. W. Croudace, Calixarene-based Extraction Chromatographic Separation of 135Cs and 137Cs in Environmental and Waste Samples Prior to Sector Field ICP-MS Analysis. *Anal. Chem.* **86**, 11890-11896 (2014). doi:10.1021/ac5036988

176. D. A. Skoog, F. J. Holler, S. R. Crouch, in *Principals of Instrumental Analysis*. (Brooks Cole, Belmont, 2007), pp. 281 - 301.

177. D. A. Skoog, F. J. Holler, S. R. Crouch, in *Principals of Instrumental Analysis*. (Brooks Cole, Belmont, 2007), pp. 550 - 585.

178. R. Murugan, T. Aono, S. K. Sahoo, Precise Measurement of Tellurium Isotope Ratios in Terrestrial Standards Using a Multiple Collector Inductively Coupled Plasma Mass Spectrometry. *Molecules* **25**, 14 (2020). doi:10.3390/molecules25081956

179. M. L. Pons, M. A. Millet, G. N. N. Nowell, S. Misra, H. M. M. Williams, Precise measurement of selenium isotopes by HG-MC-ICPMS using a 76-78 double-spike. *J. Anal. At. Spectrom.* **35**, 320-330 (2020). doi:10.1039/c9ja00331b

180. S. Y. Tong, J. Meija, L. Zhou, Z. Mester, L. Yang, Determination of the isotopic composition of hafnium using MC-ICPMS. *Metrologia* **56**, 8 (2019). doi:10.1088/1681-7575/ab2995

181. J. S. Denton, K. C. Treinen, Y. Chen, E. Baransky, A. M. Gaffney, S.-H. Huang, T. M. Kayzar-Boggs, K. Samperton, R. E. Steiner, A. M. Wende, R. W. Williams, Y.-G. Zhao, International cooperation in age-dating uranium standards for nuclear forensics using the 231Pa/235U radiochronometer. *J. Radioanal. Nucl. Chem.* **324**, 705-714 (2020). doi:10.1007/s10967-020-07084-x

182. A. M. Gaffney, J. B. N. Wimpenny, T. Parsons-Davis, R. W. Williams, R. A. Torres, B. W. Chung, A case study in plutonium radiochronometry using multiple isotope systems. *J. Radioanal. Nucl. Chem.* **318**, 287-295 (2018). doi:10.1007/s10967-018-6131-7

183. E. Mullins, *Statistics for the Quality Control Chemistry Laboratory*. (Royal Society of Chemistry, Cambridge, 2003).

184. C. J. Werner, "MCNP users manual - code version 6.2," *LA-UR-17-29981* (Los Alamos National Laboratory, 2017).

185. L. W. Gray, K. S. Holliday, A. Murray, M. Thompson, D. T. Thorp, S. Yarbro, T. J. Venetz, "Separation of Plutonium from Irradiated Fuels and Targets," (Lawrence Livermore National Laboratory, United States, 2015). https://e-reports-ext.llnl.gov/pdf/799624.pdf

186. M. Benedict, T. H. Pigford, L. Hans Wolfgang, *Fuel Reprocessing*. Nuclear Chemical Engineering, Second Edn. (McGraw-Hill Education, 1981).

187. World Nuclear Association, "Fast Neutron Reactors." Last updated Februrary 2020, accessed June 19th, 2020. https://www.world-nuclear.org/information-library/current-and-future-generation/fast-neutron-reactors.aspx

188. F. Pointurier, N. Baglan, P. Hémet, Ultra low-level measurements of actinides by sector field ICP-MS. *Appl. Radiat. Isot.* **60**, 561-566 (2004). doi:10.1016/j.apradiso.2003.11.083

189. G. Marinov, A. Marinova, M. Milanova, S. Happel, N. A. Lebedev, A. Drokhlyansky, N. Mirzayev, D. V. Karaivanov, D. V. Filosofov, Sorption of Rare-Earth Elements and Ac on UTEVA Resin in Different Acid Solutions. *Solvent Extr. Ion Exch.* **35**, 280-291 (2017). doi:10.1080/07366299.2017.1336404

190. K. Kołacińska, T. A. DeVol, A. F. Seliman, J. Dudek, M. Trojanowicz, Sequential injection analysis system with DGA resin for sample pretreatment in ICP-MS determination of 239Pu in nuclear industry samples. *Microchem. J* **152**, 104426 (2020). doi:10.1016/j.microc.2019.104426

191. N. l. Banik, K. Lützenkirchen, R. Malmbeck, A. Nichol, A method for the mg scale separation of curium(III) from americium(III) by HPLC using a SCX column. *J. Radioanal. Nucl. Chem.* **321**, 841-849 (2019). doi:10.1007/s10967-019-06653-z

192. B. D. Roach, E. K. Fenske, D. C. Glasgow, J. D. Partridge, T. J. Keever, J. M. Giaquinto, Rapid concentration and isotopic measurements of ultra-trace 235U fission products with comparison to an ORIGEN isotope depletion model. *Talanta* **205**, 120079 (2019). doi:10.1016/j.talanta.2019.06.079

193. F. Guéguen, H. Isnard, A. Nonell, L. Vio, T. Vercouter, F. Chartier, Neodymium isotope ratio measurements by LC-MC-ICPMS for nuclear applications: investigation of isotopic fractionation and mass bias correction. *J. Anal. At. Spectrom.* **30**, 443-452 (2015). doi:10.1039/C4JA00361F

194. O. J. Wick, *Plutonium Handbook : A Guide to the Technology*. (The American Nuclear Soc., La Grange Park, Ill., 1980), vol. 1 & 2.

195. E. Philip Horwitz, R. Chiarizia, M. L. Dietz, A novel strontium-selective extraction chromatographic resin. *Solvent Extr. Ion Exch.* **10**, 313-336 (1992). doi:10.1080/07366299208918107

196. International Organization for Standardization, Determination of the Characteristic Limits (Decision Threshold, Detection Limit and Limits of the Coverage Interval) for Measurements of Ionizing Radiation — Fundamentals and Application. Part 3: Applications to Unfolding Methods. ISO 11929-3:2019, 2019.

197. J. L. Ryan, E. J. Wheelwright, "The Recovery, Purification, and Concentration of Plutonium by Anion Exchange in Nitric Acid," *HW-55893* (Hanford Atomic Products Operation, 1959). https://www.osti.gov/servlets/purl/4232455

198. B. Michael, E. W. Michael, Isotopic compositions of the elements 2009 (IUPAC Technical Report). *Pure and Applied Chemistry* **83**, 397-410 (2011). doi:10.1351/PAC-REP-10-06-02

199. Multiple Authors, in *Manhattan Distric History - Pile Project X-10,* G. Hadden, Ed. (Washington, D.C.: Manhattan District, 1946), vol. II - Research - Clinton Laboratories.

200. L. Hoddeson, The discovery of spontaneous fission in plutonium during World War II. *Historical Studies in the Physical and Biological Sciences* **23**, 279-300 (1993). doi:10.2307/27757700

201. A. A. Bartlett, D. F. Swinehart, "Isotopic composition of plutonium II," *LA-327* (Los Alamos National Laboratory, 1945).

202. A. A. Bartlett, D. F. Swinehart, "Isotopic composition of plutonium III," *LA-561* (Los Alamos National Laboratory, 1946).

203. A. A. Bartlett, D. F. Swinehart, R. W. Thompson, "Isotopic composition of plutonium I," *LA-168* (Los Alamos National Laboratory, 1944).

204. L. Hempelmann, "Health report," *LA-MS-67* (Los Alamos National Laboratory, 1944).

205. A. U. Seybolt, L. Lovinson, J. Zaring, "Metallurgy of plutonium," *LA-70* (Los Alamos National Laboratory, 1944).

206. A. H. Compton, M. D. Whitaker, R. L. Doan, H. W. Newson, "Physics of the clinton pile," *CP-1300 (A-1859)* (Oak Ridge National Laboratory, 1944).

207. A. F. Rupp, J. A. Cox, "Operation of the ORNL graphite reactor and the low-intensity test reactor," *ORNL-1866* (Oak Ridge National Lab, 1955). https://www.osti.gov/servlets/purl/4340941

208. D. L. Clark, S. S. Hecker, G. D. Jarvinen, M. P. Neu, in *The Chemistry of the Actinide and Transactinide Elements,* L. R. Morss, N. M. Edelstein, J. Fuger, Eds. (Springer Netherlands, Dordrecht, 2006), pp. 813-1264.

209. G. Matlack, "A Plutonium Primer: An Introduction to Plutonium Chemistry and Its Radioactivity," *LA-UR-02-6594* (Los Alamos National Laboratory, 2003).

210. W. Bebbington, The Reprocessing of Nuclear Fuels. *Scientific American* **235**, 30 - 41 (1976). doi:10.1038/scientificamerican1276-30

211. E. E. Tereshatov, M. Y. Boltoeva, V. Mazan, M. F. Volia, C. M. Folden III, Thallium Transfer from Hydrochloric Acid Media into Pure Ionic Liquids. *J. Phys. Chem. B* **120**, 2311-2322 (2016). doi:10.1021/acs.jpcb.5b08924

212. E. E. Tereshatov, M. Boltoeva, V. Mazan, C. Baley, C. M. Folden III, Hydrophobic polymerized ionic liquids for trace metal solid phase extraction: thallium

transfer from hydrochloric acid media. *New J. Chem.* **43**, 8958-8969 (2019). doi:10.1039/c9nj00689c

213. M. F. Volia, E. E. Tereshatov, V. Mazan, C. M. Folden III, M. Boltoeva, Effect of aqueous hydrochloric acid and zwitterionic betaine on the mutual solubility between a protic betainium-based ionic liquid and water. *J. Mol. Liq.* **276**, 296-306 (2019). doi:10.1016/j.molliq.2018.11.136

214. M. F. Volia, E. E. Tereshatov, M. Boltoeva, C. M. Folden III, Indium and thallium extraction into betainium bis(trifluoromethylsulfonyl)imide ionic liquid from aqueous hydrochloric acid media. *New J. Chem.* **44**, 2527-2537 (2020). doi:10.1039/c9nj04879k

215. A. V. Boyarintsev, G. V. Kostikova, S. I. Stepanov, A. M. Chekmarev, A. Y. Tsivadze, Liquid–liquid extraction of trivalent americium from carbonate and carbonate–peroxide aqueous solutions by methyltrioctylammonium carbonate in toluene. *J. Radioanal. Nucl. Chem.* **324**, 1031-1038 (2020). doi:10.1007/s10967-020-07162-0

216. R. Gupta, B. Vats, A. K. Pandey, M. K. Sharma, P. Sahu, A. K. Yadav, S. M. Ali, S. Kannan, Insight into speciation and electrochemistry of uranyl ions in deep eutectic solvents. *J. Phys. Chem. B* **124**, 181-189 (2020). doi:10.1021/acs.jpcb.9b08197

217. C. Lefebvre, T. Dumas, C. Tamain, T. Ducres, P. L. Solari, M.-C. Charbonnel, Addressing ruthenium speciation in tri-n-butyl-phosphate solvent extraction process by fourier transform infrared, extended x-ray absorption fine structure, and single crystal x-ray diffraction. *Ind. Eng. Chem. Res.* **56**, 11292-11301 (2017). doi:10.1021/acs.iecr.7b02973

218. I. J. Schwerdt, C. Hawkins, B. Taylor, A. Brenkmann, S. Martinson, L. W. McDonald, Uranium oxide synthetic pathway discernment through thermal decomposition and morphological analysis. *Radiochim. Acta* **107**, 193-205 (2019). doi:10.1515/ract-2018-3033

219. R. Rosner, L. Eden, Rebuilding an aging nuclear weapons complex: What should the United States do, and not do? An overview. *Bull. Atom. Scient.* **75**, 3-8 (2019). doi:10.1080/00963402.2019.1555977

220. S. D. Conradson, N. Bock, J. M. Castro, D. R. Conradson, L. E. Cox, W. Dmowski, D. E. Dooley, T. Egami, F. J. Espinosa-Faller, F. J. Freibert, A. J. Garcia-Adeva, N. J. Hess, E. Holmstrom, R. C. Howell, B. A. Katz, J. C. Lashley, R. J. Martinez, D. P. Moore, L. A. Morales, J. D. Olivas, R. A. Pereyra, M. Ramos, J. H. Terry, P. M. Villella, Intrinsic Nanoscience of delta Pu-Ga Alloys: Local Structure and Speciation, Collective Behavior, Nanoscale Heterogeneity, and Aging Mechanisms. *J. Phys. Chem. C* **118**, 8541-8563 (2014). doi:10.1021/jp5004038

221. O. A. Akindele, B. S. Alan, J. T. Burke, R. J. Casperson, R. O. Hughes, J. D. Koglin, K. Kolos, E. B. Norman, S. Ota, A. Saastamoinen, Expansion of the surrogate method to measure the prompt fission neutron multiplicity for Pu-241. *Phys. Rev. C* **99**, 7 (2019). doi:10.1103/PhysRevC.99.054601

222. A. Ratkiewicz, J. A. Cizewski, J. E. Escher, G. Potel, J. T. Burke, R. J. Casperson, M. McCleskey, R. A. E. Austin, S. Burcher, R. O. Hughes, B. Manning, S. D. Pain, W. A. Peters, S. Rice, T. J. Ross, N. D. Scielzo, C. Shand, K. Smith, Towards neutron capture on exotic nuclei: Demonstrating (d,p gamma) as a surrogate reaction for (n,gamma). *Phys. Rev. Lett.* **122**, 7 (2019). doi:10.1103/PhysRevLett.122.052502

223. M. J. Sarsfield, R. J. Taylor, C. Puxley, H. M. Steele, Raman spectroscopy of plutonium dioxide and related materials. *J. Nucl. Mater.* **427**, 333-342 (2012). doi:10.1016/j.jnucmat.2012.04.034

224. E. Villa-Aleman, N. J. Bridges, T. C. Shehee, A. L. Houk, Raman microspectroscopy of PuO_2 particulate aggregates. *J. Nucl. Mater.* **515**, 140-149 (2019). doi:10.1016/j.jnucmat.2018.12.022

225. B. L. Scott, A. L. Pugmire, J. T. Stritzinger, D. K. Veirs, L. E. Wolfsberg, M. P. Wilkerson, Relationships between experimental signatures and processing history for a variety of PuO_2 materials. *J. Nucl. Mater.* **521**, 155-160 (2019). doi:10.1016/j.jnucmat.2019.04.036

226. D. L. Clark, The chemical complexities of plutonium. *Los Alamos Sci.* **26**, 364-381 (2000).

227. J. L. Drummond, G. A. Welch, The preparation and properties of some plutonium compounds. Part VI. Plutonium dioxide. *J. Chem. Soc. (Resumed)*, 4781-4785 (1957). doi:10.1039/JR9570004781

APPENDIX A

LIQUID-LIQUID EXTRACTIONS

Liquid-liquid extractions have been investigated for weapons research since the beginning of the US program in 1943 (*110*). These extractions are performed by mixing a liquid phase containing an extractant with another immiscible liquid phase containing one or more species desired for extraction. The most common applications extract desired species from a mineral acid aqueous phase into a hydrocarbon organic phase containing an extractant. Discussion in this section will assume material is being extracted from an aqueous phase (*aq*) into an organic phase (*org*).

The extraction yield of a species is determined using Equation A.01 where *m* is mass, subscript *i* refers to the initial state, and subscript *f* refers to the final state.

$$E = \frac{m_{org}}{m_{org} + m_{aq}} = \frac{m_{aq,f} - m_{aq,i}}{m_{aq,i}} \qquad (A.01)$$

The first solution of Equation A.01 is the most thorough solution that generally provides the most accurate measurement. The second solution is only used when the mass of the constituent in the *org* phase cannot be measured due to an experimental constraint. The challenge with the second solution is that it cannot be used if the initial and final masses in the *aq* phase are within experimental error. Figure A.01 shows that the smallest extraction yield which can be measured using the second solution at 2 sigma with a 2% measurement error is 7.7%.

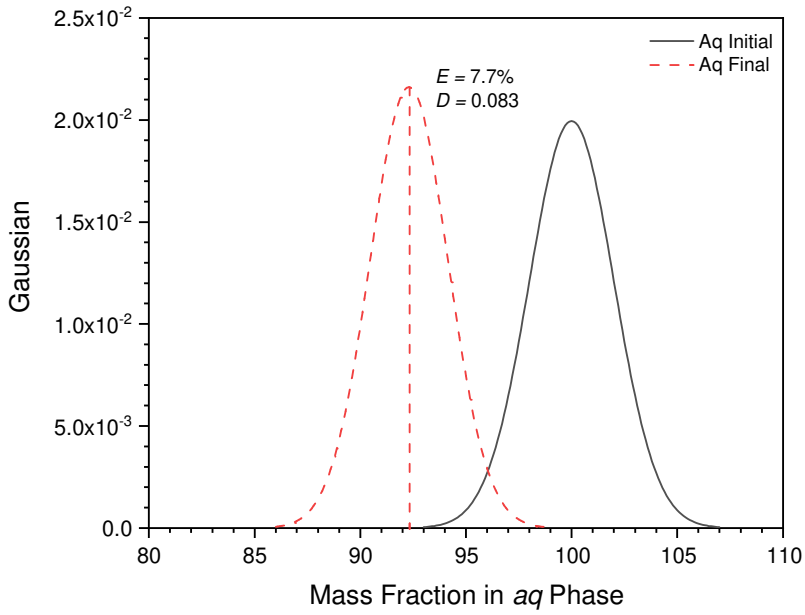

Figure A.01. Limitations in Measuring Extraction Yield. This figure demonstrates the lowest extraction yield and D-value that may be measured when using the second solutions of Equations A.01 and A.02 at 2 sigma with 2% measurement error. This limitation arises from the measurement error of the initial and final aqueous phases overlapping. An extraction yield or D-value measured below this limit using the second solutions is generally below the detection limit.

Distribution coefficients (D, D-values) are the preferred extraction metric when extraction yields are exceptionally high or exceptionally low. D-values may be calculated per Equation A.02 where V is the volume of a phase.

$$D = \frac{m_{org}/V_{org}}{m_{aq}/V_{aq}} = \frac{\left(m_{aq,f} - m_{aq,i}\right)/V_{org}}{m_{aq,f}/V_{aq}} = \frac{E}{1-E}\frac{V_{aq}}{V_{org}} \qquad (A.02)$$

The first solution should be used whenever possible. The second solution should only be used when the *org* phase cannot be assayed directly, as it suffers from the same problem as extraction yield. Per Figure A.01, the smallest D-value that may be measured using the second solution at 2 sigma with a 2% measurement error is

0.083. The third solution is useful to convert between extraction yields and D-values. It should be noted that increasing the org/aq phase ratio will always increase the extraction yield but will never change the D-value. Asymmetric phase ratios are routinely used to maximize extraction yields.

Another metric commonly used in liquid-liquid extractions is the decontamination factor (DF). The DF describes how effectively one species has been separated from another and may be calculated using Equation A.03 where species 1 is being separated from species 2 from an *aq* phase into an *org* phase. The second solution to this equation is only applicable over a single extraction step.

$$DF = \frac{m_{2,aq}/m_{1,aq}}{m_{2,org}/m_{1,org}} = \frac{D_1}{D_2} \qquad (A.03)$$

In the case where a single "contact" does not extract enough of the desired material, a series of extractions may be performed until the extraction requirements are satisfied. These series of extractions may be performed cross-currently or counter-currently. Cross-current extractions are described in Figure A.02 with five example extractions. The "feed" represents the initial *aq* medium prior to any separation; each extraction occurs from left to right. Each *org* phase is set aside after extraction and all *org* phases are combined at the end of the process. The feed is extracted multiple times until all of the desired material has been extracted. Cross-current extractions are effective at extracting all of the desired material, but they also extract a large amount of undesired material and result in relatively low DFs.

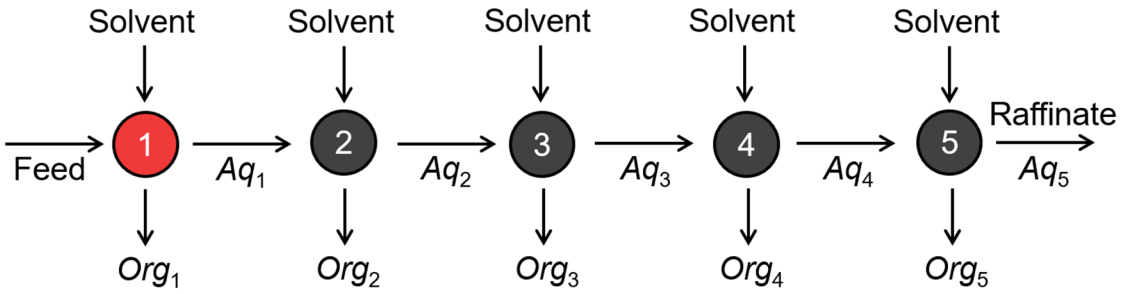

Figure A.02. Cross-Current Extractions. Cross-current extraction schematic in a five-stage extraction. The red circle indicates a stage where the *aq* phase resembles the feed; black circles indicate stages where the solvated content in the *aq* phase is significantly different than the feed. The *org* phases are set aside after extraction and are finally combined after all extractions are completed. This results in high extraction yields with relatively low decontamination factors.

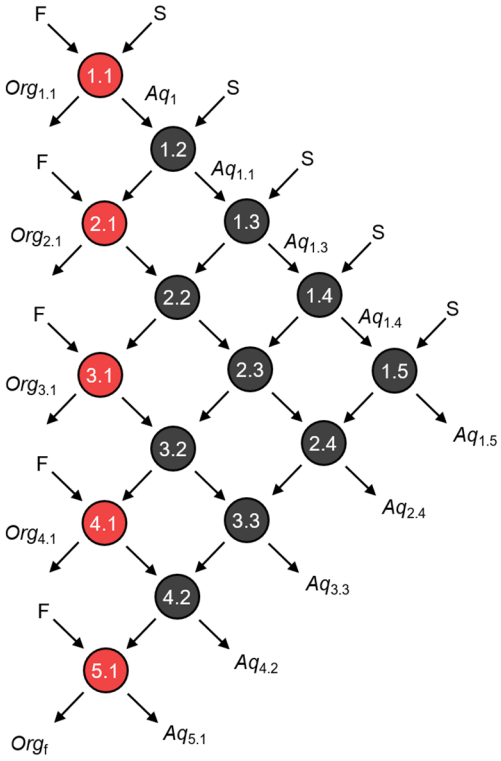

Figure A.03. Counter-Current Extractions. Counter-current extraction schematic for batch extractions in a five-stage process. The red circles indicate stages where the *aq* phase resembles the feed; black circles indicate stages where the solvated content in the *aq* phase is significantly different than the feed. F indicates the addition of fresh feed, and S the addition of fresh solvent. The *aq* and *org* phases from previous extractions are used as the initial *aq* and *org* phases for future extractions. Arrows pointing towards the right always indicate the flow of *aq* phases, while arrows pointing to the left always indicate the flow of *org* phases. The final product is represented by org_f and features high extraction yields with high decontamination factors. The other *org* phases do not represent the final product and do not feature high extraction yields.

Counter-current extractions are generally more complicated as shown using a batch model in Figure A.03. These extractions use the *aq* and *org* phases discharged from a previous extraction as the initial *aq* and *org* phases for a follow up extraction. Counter-current extractions are a powerful tool used to extract the entirety of one species while maximizing its decontamination. While the scheme in Figure A.03 must be followed for batch extractions in a laboratory, it is only a representation of counter-current extractions as they are performed in industrial facilities. Some processing facilities use centrifugal contactors to perform a multi-stage counter-current extraction within one device (*210*).

The speciation of an extracted species may be solved using a combination of slope analysis and instrumental characterizations. In slope analysis, the D-value of extraction is plotted as a function of extraction parameters such as acid concentration or extractant concentration. The equilibrium equation of the extraction may be solved where the total charge on the extracted species is left as an unknown variable equal to the slope of the plotted function. These slopes have been used to determine the speciation of an extracted species extensively in the literature (*211-215*). Multiple modes of instrumental characterizations are also available to determine the speciation of an extracted species. Some recent works report using techniques such as Fourier-transform infrared spectroscopy (FTIR), x-ray absorption spectroscopy (XAS), and molecular dynamics simulations (MDs) to determine speciation (*216, 217*).

APPENDIX B

THE PUREX PROCESS FOR PLUTONIUM SEPARATIONS

The Plutonium Uranium Redox Extraction (PUREX) process has been the dominant Pu purification scheme used world-wide since the first PUREX reprocessing pilot facility was built in 1952 (*185*). The process utilizes tri-*n*-butyl phosphate (TBP) as an extractant present on the order of 30% by volume in an *n*-dodecane *org* phase to extract U and Pu out of irradiated U fuel solvated in HNO_3. The D-values for U and Pu extraction are not large, generally ranging up to 10 under most conditions; however, its strength comes from the low D-values for most FP elements. By utilizing counter-current extraction processes, the process features extremely high FP DFs on the order of 10^6 – 10^8 with high U and Pu extraction yields ≥ 99% (*185, 186*). TBP is known to extract even valence An elements with neutral speciation per Equations B.01 and B.02.

$$AnO_2^{2+} + 2NO_3^- + 2TBP \rightarrow AnO_2(NO_3)_2TBP_2 \qquad (B.01)$$

$$An^{4+} + 4NO_3^- + 2TBP \rightarrow An(NO_3)_4TBP_2 \qquad (B.02)$$

The PUREX process as discussed herein was outlined in the proposed Barnwell Nuclear Fuel Plant (BNFP) from the 1970s. This plant was built in Barnwell, SC, to reprocess irradiated commercial reactor fuel but was ultimately shut down prior to initial operations due to policy changes in the federal government. The flowsheet for this facility is described in some detail in the literature (*186, 210*); a representation is shown in Figure B.01.

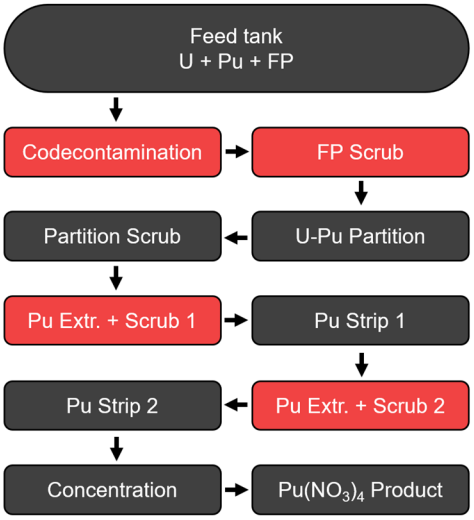

Figure B.01. Pu Purification Process Flowsheet. The eight major steps of the PUREX process as designed at the Barnwell Nuclear Fuel Plant. Black cells indicate stages where Pu exists in the *aq* phase at equilibrium, red stages the *org* phase. Temperature, acidity, U concentration, and the *org*/*aq* phase ratio change between each step. Only the codecontamination raffinate is sent to waste; the other raffinate streams are recycled back to the codecontamination step.

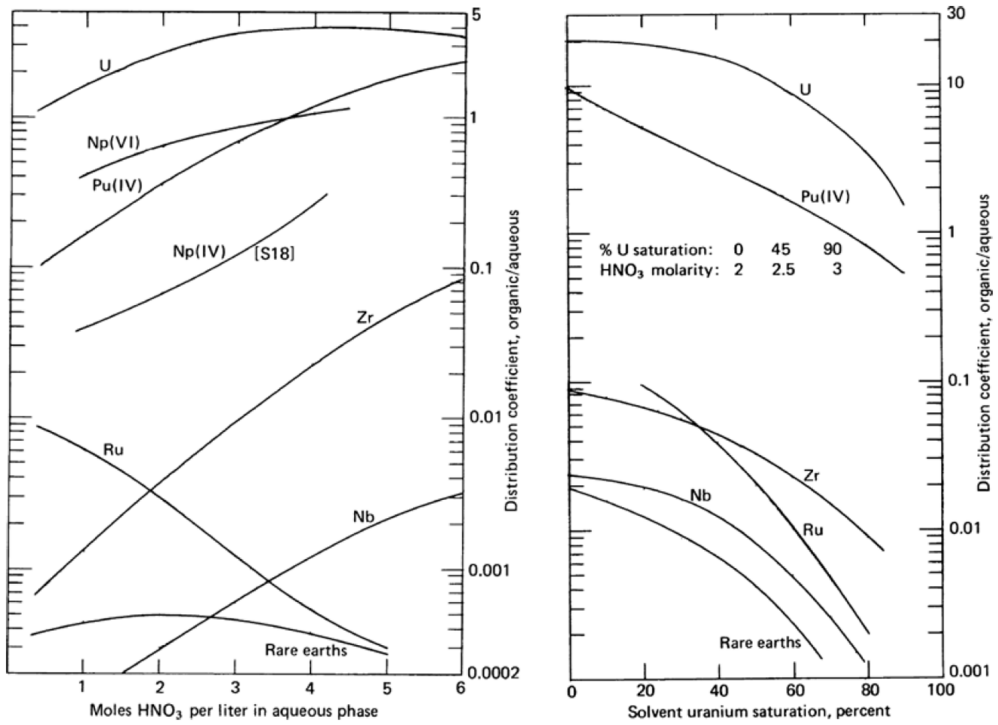

Figure B.02. Pu Separation D-Values. The distribution coefficient of extraction for some elements under varying HNO_3 and U concentrations. Extraction yields tend to increase with increasing HNO_3 and decrease with increasing U concentration. Presented with permission from (186).

The first step is referred to as "codecontamination" and involves separating U(VI) and Pu(IV) jointly from the irradiated fuel solution. This step is practically the most critical in the entire process, as it features the highest DFs and extraction yields. As instituted at the BNFP, this step uses a 10-stage centrifugal contactor to perform 10 extractions in tandem via a counter-current extraction scheme.

Following codecontamination, U and Pu are partitioned from each other using redox chemistry. As TBP only extracts even valence An elements into the *org* phase, Pu is readily "stripped" back into the *aq* phase via reduction to Pu(III). This is accomplished with redox agents such as Fe(II), hydroxylamine, or catalytic current (*186*). After partition, the Pu is further purified with two more extraction steps to maximize the decontamination of the FP elements.

The D-values of Pu, U, and the FP elements throughout the PUREX process is a function of *aq* phase acidity, U concentration, and temperature. Some of these trends are reported in Figure B.02 (*186*). In general, the D-values of extractable species tend to increase with HNO_3 concentration through Le Chatelier's principle as NO_3^- is a reactant of extraction. The D-value is shown to decrease for all species as U concentration increases. This is understood through competitive extraction – U is the species with the highest D-value in solution, therefore increasing the concentration of U present decreases the amount of free TBP available to extract other species.

Due to the nature of counter-current extractions, extraction conditions do *not* need to maximize the D-value of Pu and U; if the extraction yield for a species is high enough, a 10-stage centrifugal contactor will extract nearly 100% of the material. As

the extraction yield of an unextractable species approaches 0%, a 10-stage centrifugal contactor will extract the nominal extraction yield representative from a single extraction. The BNFP takes advantage of this by choosing extraction conditions which minimize the extraction of the FP elements to maximize DFs.

Examples of extracted and unextracted species in counter-current PUREX extractions are presented in Figure B.03. These extractions were performed by the author with a 3 M HNO_3, 0.85 M UO_2^{2+} *aq* phase and a 30% TBP in *n*-dodecane *org* phase at 40 °C with an *org*/*aq* phase ratio of 2.3/1. The nominal extraction yields of Pu and Ru under these conditions were measured as 70% by α spectrometry and 1.1% by γ spectrometry, respectively. The red circles indicate *aq* phases which resemble the feed with a high concentration of U; the black circles indicate *aq* phases which have a significantly lower concentration of U, and therefore higher D-values for all species. The extraction yields of Pu and Ru in these black circles were approximately 80% and 9%, respectively. The nature of these counter-current extractions allows for the extraction yield of Pu to converge towards 100% in the final product (org_f) as the number of stages increases past 5, while the extraction yield of a FP such as Ru remains at its nominal value of approximately 1% (red circle in the legend of Figure B.03).

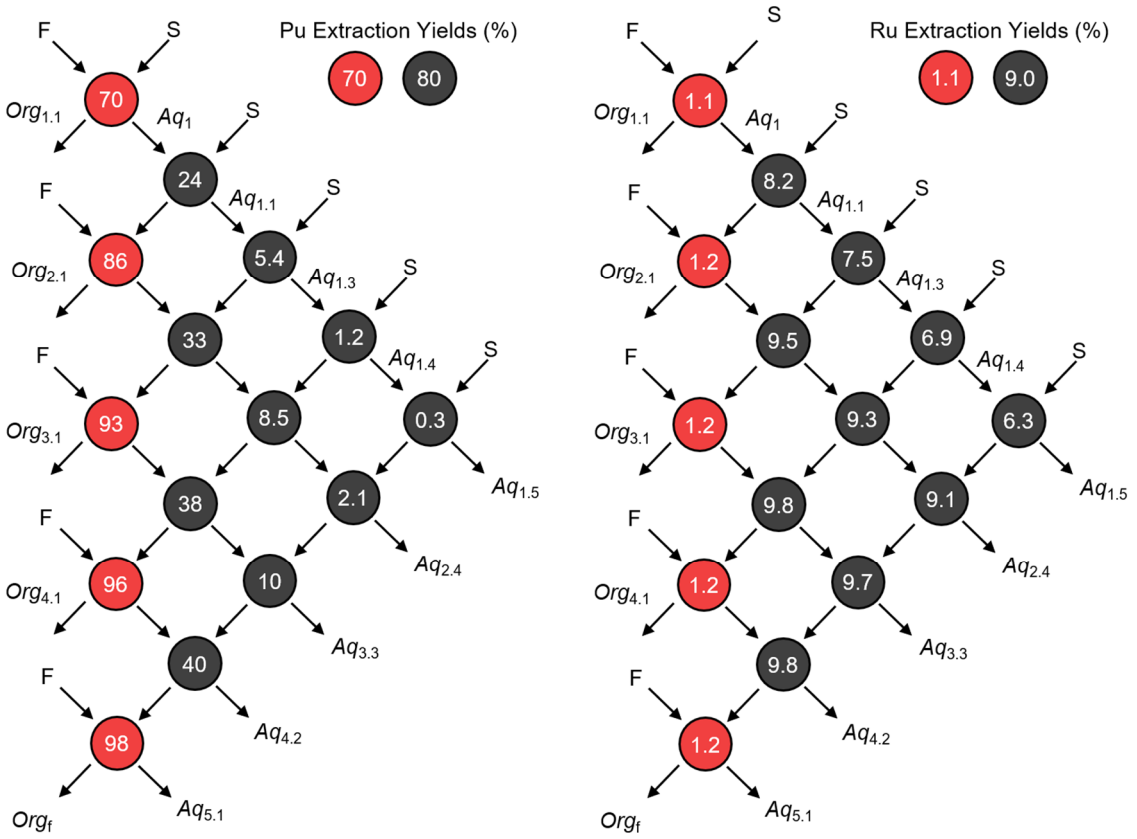

Figure B.03. Counter-Current Extraction Yields. The extraction yields of Pu and Ru in a representative 5-stage counter-current extraction process. Red circles indicate extractions where the *aq* phase resembles the feed, black circles indicate extractions where the *aq* phase contains solved content significantly different than the feed. Numbers represent extraction yield into the *org* phase at the given extraction. This diagram includes five feed injections; therefore, the maximum extraction yield possible across a diagram is 500%. Extractions were performed with the UO_2 irradiated at the High Flux Isotope Reactor.

The codecontamination and partition extractions are the only steps in the PUREX process where a significant amount of U is present. As such, it is expected for the D-values of the FP elements in these early steps to be significantly different than the D-values of the FP elements in the later steps, per Figures B.03 and B.04. Therefore, the inter-elemental FP ratios within PUREX-separated Pu may indicate from which stream the Pu was discharged – either prior to or after the partition step.

This is currently an unexplored area in nuclear forensics, but it does present challenges. Primarily, the PUREX process extraction conditions change between each PUREX facility, so a wide range of extraction conditions would need to be tested to make strong forensic conclusions. However, the changing PUREX conditions between facilities may provide the capability to determine if a sample of PUREX separated Pu is consistent with separation at a specific facility. In such a case, a forensic database would need to be built containing the D-values of each FP at each step in all declared PUREX facilities. This is certainly better done with an extraction code than by batch extractions in the radiochemistry laboratory.

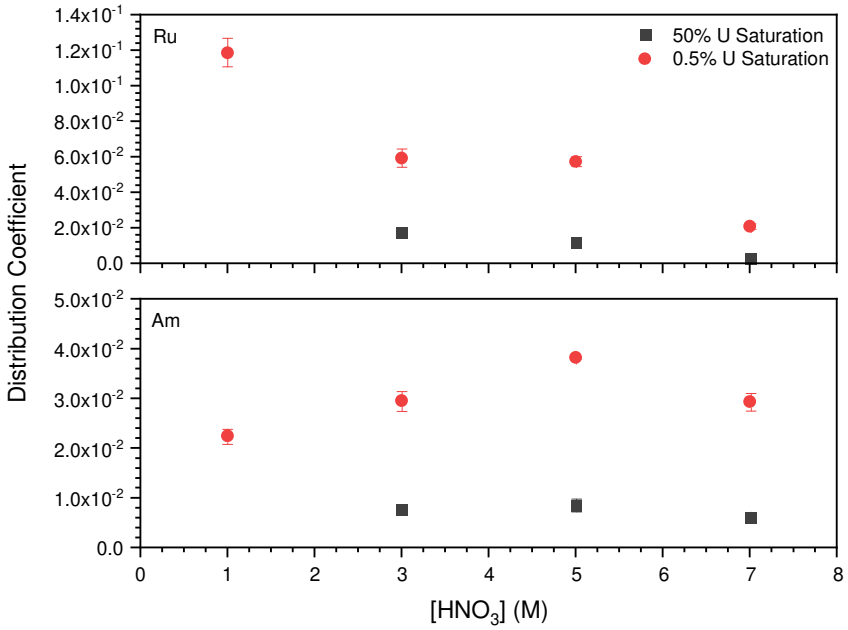

Figure B.04. D-values of Am and Ru. Changes in the D-values of Ru (top) and Am (bottom) under varying conditions in the PUREX process. The black squares represent extractions where 50% of the TBP molecules are saturated with U, the red circles 0.5%. Extractions were performed at 25 °C with the UO_2 irradiated at the High Flux Isotope Reactor as described in Section 2.1.1.

APPENDIX C

SAMPLE MORPHOLOGY IN NUCLEAR FORENSICS

Sample morphology is investigated during some forensic procedures and checked for consistency against the documented morphology from production facilities. Currently, sample morphology tends to hold less forensic information than the other observables available, however it still produces valuable information. In one investigation, the grain size of an HEU powder was used to determine that a sample of smuggled U_3O_8 was not produced from a US weapons enrichment facility (*18*). The TEM used revealed two dominate microstructures of U_3O_8 with an average grain size of 0.1 μm, shown in Figure C.01 (*18*).

One forensic group from the University of Utah has determined that the morphology of UO_2 (and other U species) may reveal information about the chemical pathway used to produce the material (*73-77, 218*). U ore concentrates (UOCs) are precipitated from uranyl nitrate hexahydrate (UNH) solutions using NH_4OH, $(NH_4)_2CO_3$, MgO, or H_2O_2. The U species precipitated using these reagents are usually called ammonium diuranate (ADU), ammonium uranyl carbonate (AUC), magnesium diuranate (MDU), or uranyl hydroxide (UH), respectively.

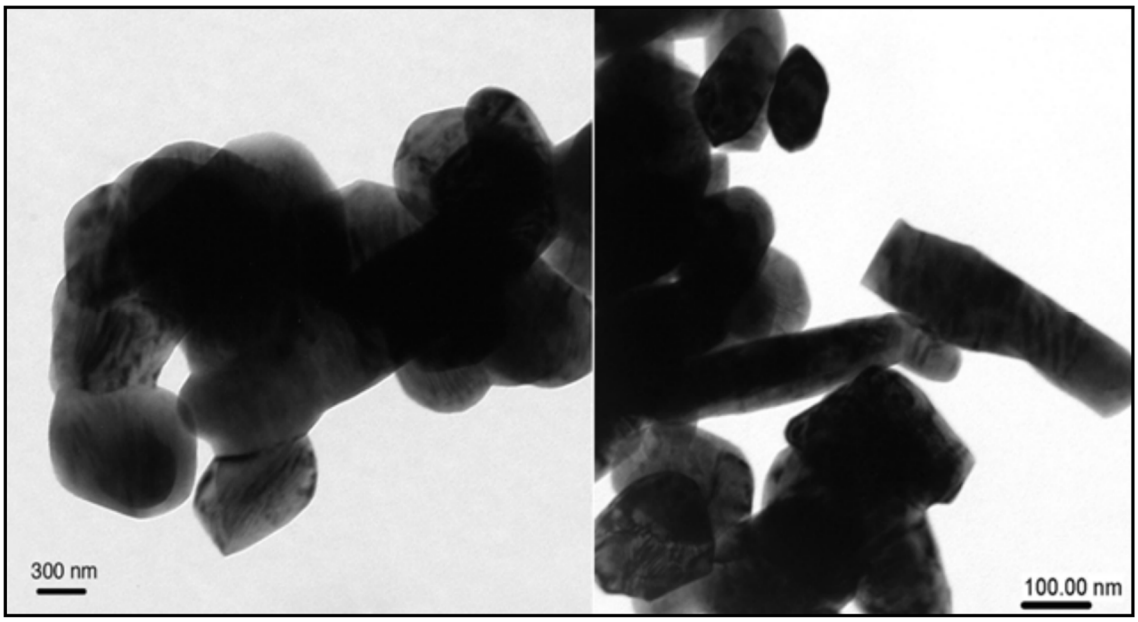

Figure C.01. Microscopy of Smuggled U_3O_8 From Bulgaria. Morphology of interdicted highly enriched U_3O_8 as seen by TEM. The TEM revealed two grain shapes, "oval to equant" grains (left), and "rod or plate-shaped" grains (right). The average grain size of the material was significantly smaller than for highly enriched U_3O_8 produced from US weapons enrichment facilities. Presented with permission from (18).

Recent work has shown the morphology of these UOCs are significantly different immediately after precipitation, depicted in Figure C.02 (*218*) as viewed using an SEM. In addition, the morphology of the ultimate UO_2 product expresses differences between each of the starting UOCs, shown in Figure C.03 (*218*). The precipitation pathway applied in industry is dependent upon the properties of the ore as it is mined; therefore, it may be possible to discriminate the range of facilities that produced a sample of unknown UO_2 based on its morphology.

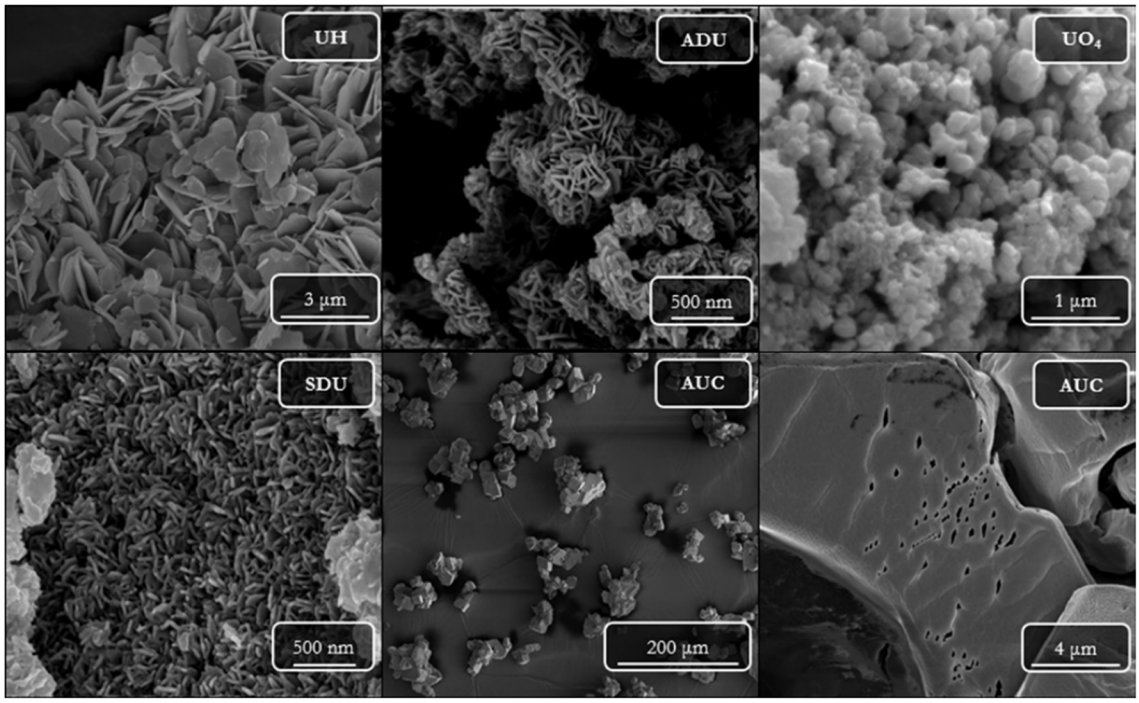

Figure C.02. Microscopy of U Ore Concentrates. Multiple UOCs were precipitated from a UNH solution and viewed under an SEM to identify differences in UOC morphology. Most of the different UOCs express significantly different sample morphology immediately after precipitation. Presented from an open access publication (218).

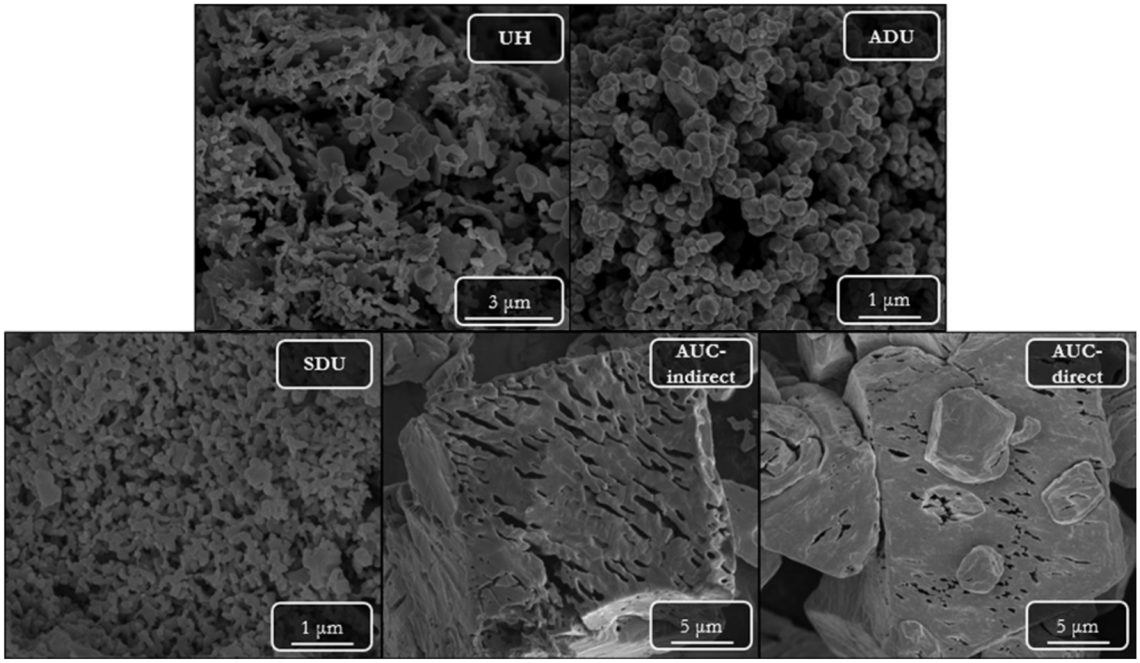

Figure C.03. U Oxides Produced from Different U Ore Concentrates. The same UOCs from Figure C.02 were calcined at 800 °C then reduced with H_2 to produce U oxides, presumably UO_2. The oxides which were produced still express significantly different morphology based on the starting UOC. Presented from an open access publication (218).

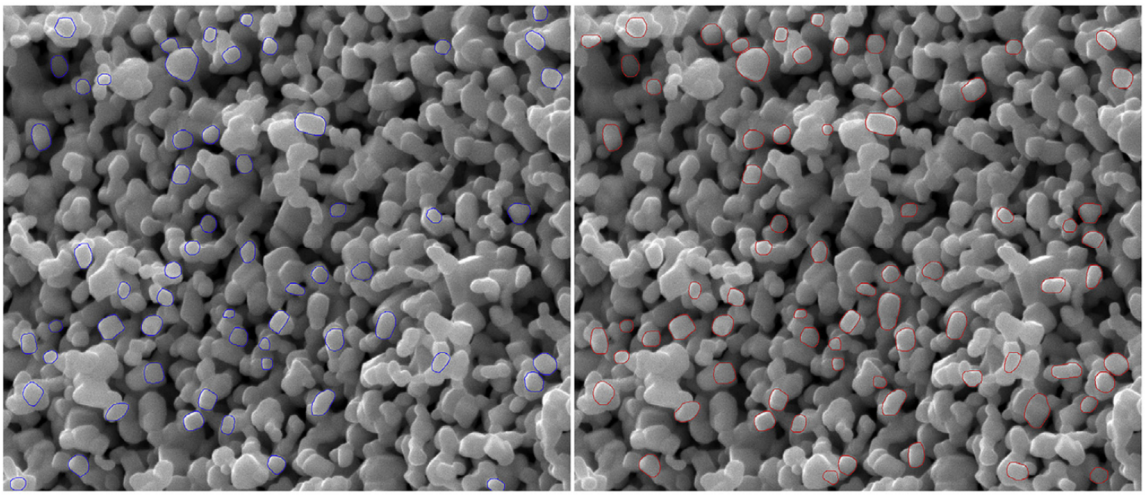

Figure C.04. U Oxide Morphology as Interpreted by an Artificial Intelligence. Comparison of the AI's ability to identify complete particulates (left, blue outlines) versus an expert scientist (right, red outlines) The AI generally identified the same particulates as the expert scientist. Presented with permission from (75).

These studies have begun using machine learning code to automatically identify the features in the SEM of U oxides that may be used to discriminate the precipitation method of the starting UOC (*75*). The artificial intelligence (AI) was trained to identify "complete" particulates in the grain structure of the U oxide, then document how those particulates change based on the precipitation method.

The comparison between AI and expert identification of complete particulates in a U oxide material is shown in Figure C.04 (*75*). The AI was able to distinguish some differences between U oxides produced from different UOCs, but there is currently little understanding of what the AI is actually looking for. Regardless, the eventual application of such techniques to samples such as those shown in Figure C.03 may standardize the process of discriminating the production facility which produced an unknown U oxide.

As a radionuclide with a relatively high specific activity, the crystal structure of $^{239}PuO_2$ and metal structure of ^{239}Pu degrade over time as they are irradiated by their own 5.5 MeV α particles. Understanding this degradation in ^{239}Pu metal is crucial to the US nuclear weapons program; the US no longer tests any of the weapons in its nuclear stockpile, so we must use other methods to verify the integrity of the ^{239}Pu metal "pit" in older weapons (*219-222*). The scope of nuclear forensics has not yet extended into physical investigations of complete Pu pits, so these effects are currently of minor interest to the field. A forensic scientist is much more likely to investigate PuO_2, which also experiences significant degradation over time.

These degradation effects have been identified in the Raman spectra of PuO_2 materials (*84, 223-225*). One study annealed a sample of PuO_2 to repair any prior age defects then allowed it to age over a period of 2.4 y. The authors collected Raman spectra of the PuO_2 over time, shown in Figure C.05 (*84*); the spectra are focused on the T_{2g} band of the PuO_2 material and the area immediately surrounding it. The T_{2g} band was observed to broaden and two "symmetry-breaking" peaks were observed to grow in as the material aged. The height of these new peaks was associated with the density of "damaged sites." Figure C.06 (*84*) describes how the T_{2g} peak broadens and how the two new peaks grow in over time. The figure reports that the aging effects as measured by Raman are consistent with the change in the crystal structure as measured by x-ray crystallography (XRD). These effects may be used to further support chronometry in the age dating of PuO_2.

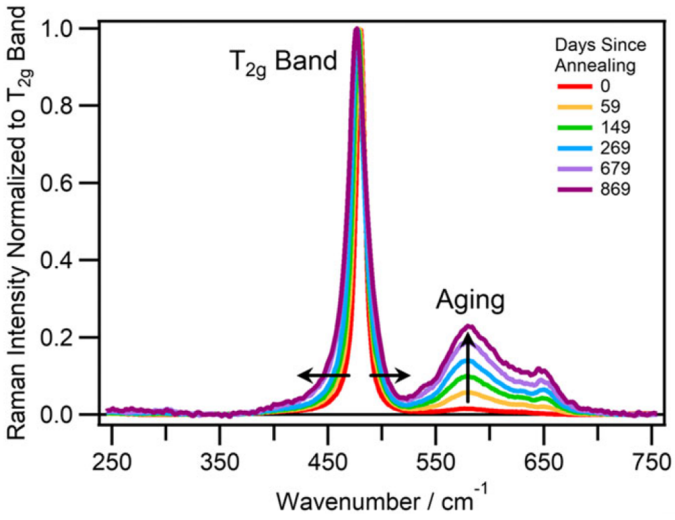

Figure C.05. Raman Spectra of Aging PuO_2. Raman spectra were taken over 2.4 y to assay the change in the T_{2g} and surrounding stretches of PuO_2 due to self-radiolysis. The T_{2g} stretch is shown to broaden over time, while the new stretches grow in over time. The new stretches are associated with damaged sites in the PuO_2 crystal structure. Presented with permission from (84).

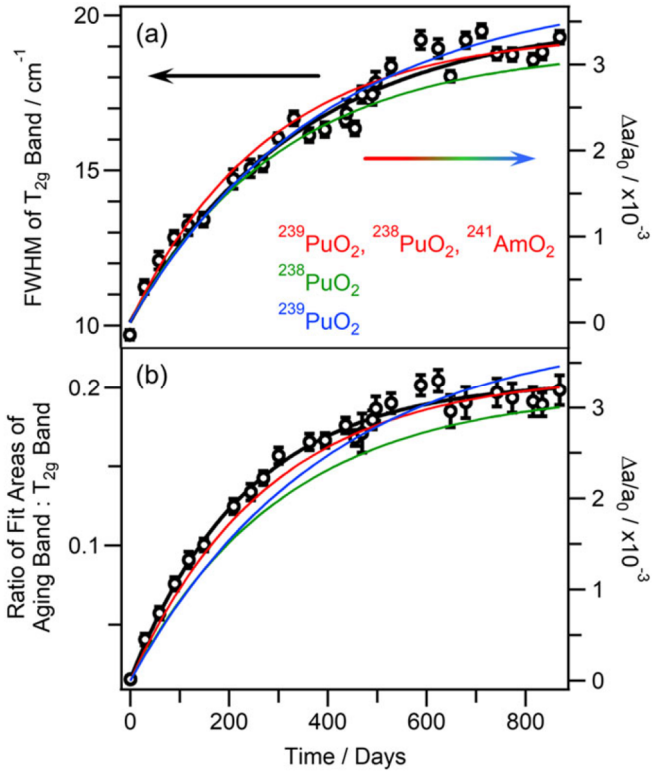

Figure C.06. Quantified Degradation of Aged PuO_2. (**A**) The change in the FWHM of the T_{2g} stretch of PuO_2 (black circles, left axis) over 2.4 years compared to the change in the lattice parameter (solid lines, right axis) by XRD. (**B**) The peak height ratio of the new stretches to the T_{2g} band compared to the changing lattice parameter in aged PuO_2. Presented with permission from (84).

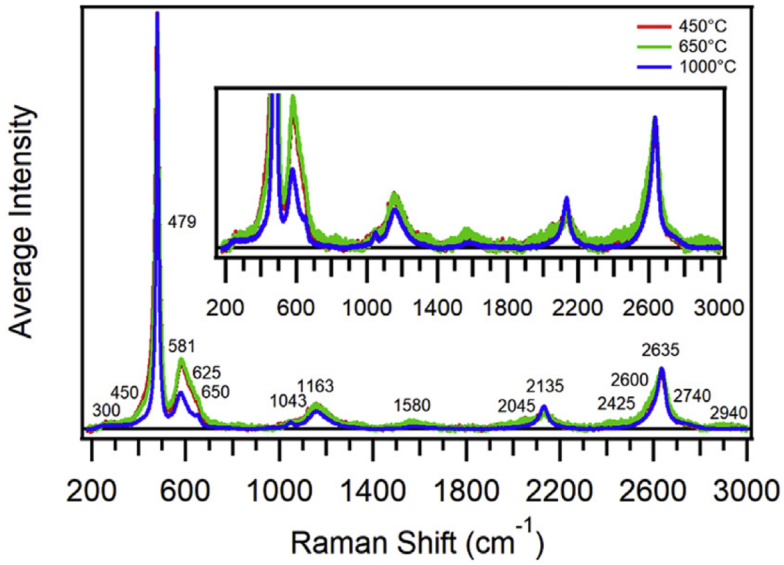

Figure C.07. Raman Spectrum of PuO_2 Calcined at Multiple Temperatures. Samples of PuO_2 recently calcined at three different temperatures were probed by Raman spectroscopy. The different calcination temperatures are expressed by changes in the FWHM of the T_{2g} shift (479 cm^{-1}) and the growth of its neighboring peaks. Presented from an open access publication (224).

Pu is typically calcined to the oxide from the metal, carbonate, nitrate, oxalate, or hydroxide form from temperatures between 300 and 1500 °C (*208, 209, 226, 227*). The starting material used for calcination tends to impact the color of the final oxide material, while the temperature of calcination has a strong effect on the dissolution of the oxide material in various acids.

"High-fired" PuO_2 calcined above 800 °C is infamous for being difficult to dissolve in most acid systems (*208, 209, 226, 227*). The temperature at which PuO_2 was calcined may also be observed from a Raman spectrum of the material, using the same T_{2g} and neighboring stretches as before. In general, higher temperature calcinations produce PuO_2 with fewer defects, resulting in a lower FWHM of the T_{2g} peak and reduced prominence of the neighboring defect stretches, shown in

Figure C.07 (*224*). Initially, these two different material properties (age and calcination temperature) affecting the same Raman stretches confounds the ability to use Raman for PuO_2 forensics; however, if the sample age is determined through other means, it may be possible to deconvolute the contributions to the Raman spectrum by the two material properties. This is currently an unexplored area in PuO_2 forensics.

APPENDIX D

POST DETONATION NUCLEAR FORENSICS

The other side of nuclear forensics investigates materials which have been exposed to a nuclear detonation to attribute properties of the detonating device. In these cases, the material properties of most interest are typically related to the design of the detonating device (*86-95*). Whether it was a ^{239}Pu or $^{233,235}U$ device should be immediately apparent based on the isotope ratios of the actinide material present in the debris and the ratio of Pu/U.

During detonation, multiple different materials are dispersed throughout the debris. These materials include remnants of the fissile pit, structural components of the weapon, activation products, and fission products. Close evaluation of these materials within the surrounding debris may reveal information about the detonating device (*95*). A large focus in post-detonation nuclear forensics is therefore focused on dissolving this debris to isolate and measure these materials (*86-88*). In support of that goal, some forensic labs have developed their own procedures to produce surrogate material which is similar to debris in composition (*78, 92-94*). In addition, the formation of vesicles in debris has been linked to the hydrodynamics of detonation, which may correspond to some device properties (*91*).

APPENDIX E

THE PERIODIC TABLE OF THE ELEMENTS

The periodic table of the elements as it is known as of July 2020 (Figure E.01).

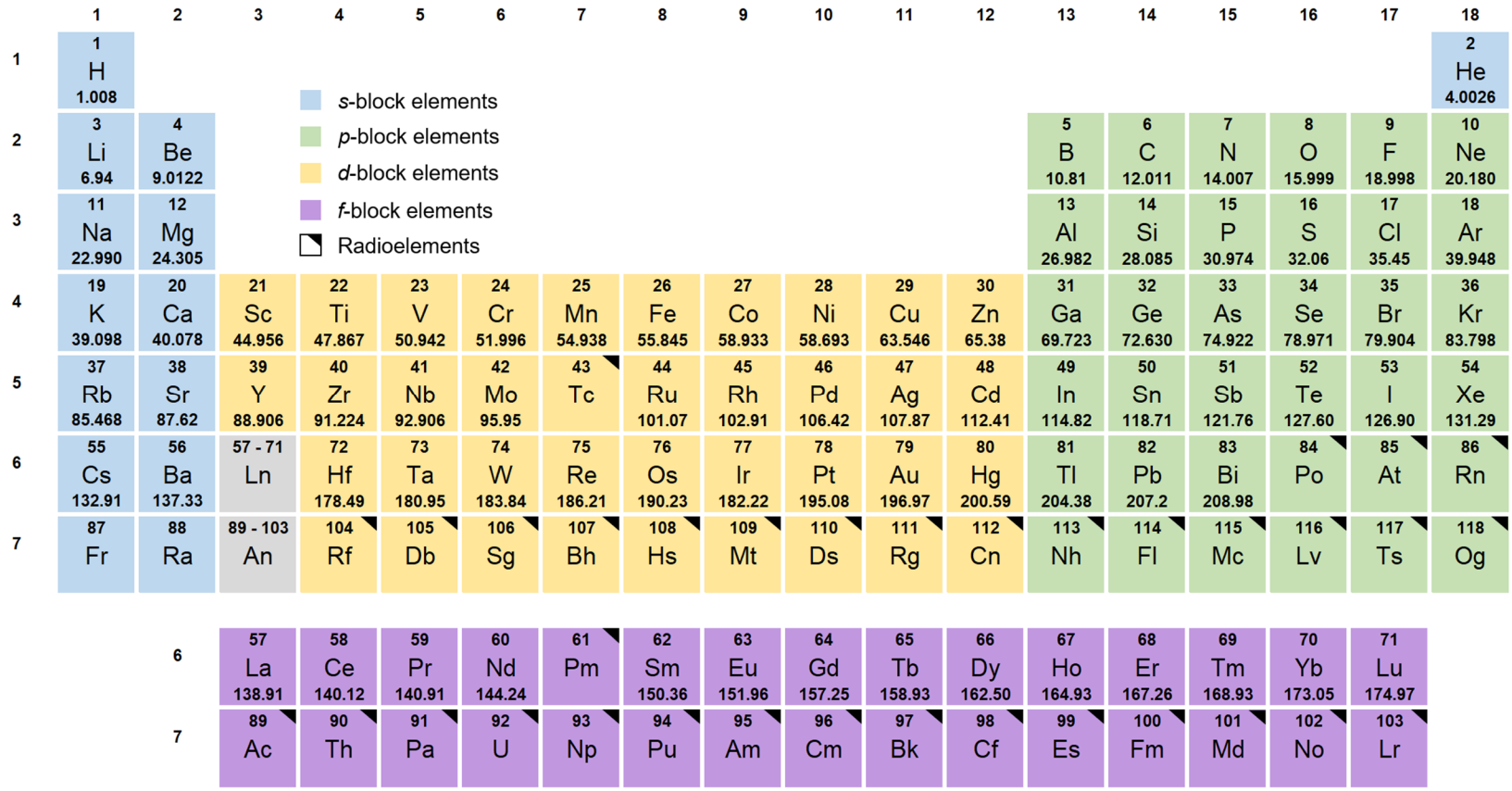

Figure E.01. The Periodic Table of the Elements. The periodic table of the elements as of July 2020. The radioelements are indicated with an earmark in the upper right corner of their symbol. Atomic numbers are listed above the atomic symbol. Molar masses are listed in units of g/mol below the atomic symbol.